

Annual Report 2020

MLZ is a cooperation between:

Front page:

Simulated electron (yellow) and positron (blue) trajectories in the magnetic field (purple) of a magnetic dipole trap.

Back page:

View of the Heinz Maier-Leibnitz area with new office, workshop and laboratory buildings in front of the Atomic Egg.

Bavarian State Ministry of
Science and the Arts



SPONSORED BY THE



Federal Ministry
of Education
and Research

The Heinz Maier-Leibnitz Zentrum (MLZ):

The Heinz Maier-Leibnitz Zentrum is a leading centre for cutting-edge research with neutrons and positrons. Operating as a user facility, the MLZ offers a unique suite of high-performance neutron scattering instruments. This cooperation involves the Technische Universität München, the Forschungszentrum Jülich GmbH and the Helmholtz-Zentrum hereon GmbH. The MLZ is funded by the German Federal Ministry of Education and Research, together with the Bavarian State Ministry of Science and the Arts and the partners of the cooperation.

The Forschungs-Neutronenquelle Heinz-Maier-Leibnitz (FRM II):

The Forschungs-Neutronenquelle Heinz-Maier-Leibnitz provides neutron beams for the scientific experiments at the MLZ. The FRM II is operated by the Technische Universität München and is funded by the Bavarian State Ministry of Science and the Arts.

Joint Annual Report 2020
of the MLZ and FRM II



Ready to deliver neutrons

The beginning of 2020 was promising, with a full cycle of neutrons for science, industry and medicine envisaged. However, the Corona pandemic with its lockdowns and travel restrictions, as well as the excess discharge of the nuclide C-14, thwarted us in our mission to deliver more neutrons in that year. Nevertheless, we have taken full advantage of the time to obviate these challenges in the future.

Regarding the discharge of C-14, relevant measures have been taken to prevent any excess release in the future. – In order to deal with the issue of ongoing Corona restrictions, we aim to make it possible to carry out experiments without travelling of the users. With this in mind, we have installed procedures for users to enable instrument control via remote access. In order to contribute to the worldwide effort on research into the Coronavirus SARS-CoV-2, a rapid access programme for proposals dealing with the study of this virus or the disease COVID-19 has been initiated.

Important achievements in 2020 relate to progress with the neutron guide hall east, which has been furnished with an interim level to house the measuring cabins. Furthermore, the whole building is now fully connected to the FRM II power supply. This enables all instruments to proceed with, or to begin, their installation in the guide hall east, namely SAPHiR, TOPAS, POWTEX, MEPHISTO/PERC, NEPOMUC and TRISP. For all construction and installation works, so-called modifications to the facility as well as permission for instrument construction are required, all of which involves a lot of paper work and documentation as well as approval by the authorities. All these tasks are making good process and we are working hard to complete the neutron guide hall east and to supply the instruments there with neutrons by the end of 2022.

We are very happy to announce that we will be able to move two high performance instruments from the neutron source in Berlin, which was shut down at the end of 2019. The Federal Ministry of Science and Research (BMBF) is funding the relocation and adaptation of the instruments to the tune of 5.62 million euros. The three axes spectrometer FLEXX, which will be called LaDiff in future and will accordingly also offer Larmor diffraction, and the fine resolution powder diffractometer FIREPOD, have already been in high demand in Berlin. They will complement and increase the appeal of our instrument suite.

In 2020, we celebrated the inauguration of our two new MLZ laboratory, workshop and office buildings. Due to the pandemic, the ceremony was very successfully held online as a live stream with more than 200 participants. Among the speakers, representatives of the funding bodies, the Bavarian State Minister for Science and the Arts, Bernd Sibler, and BMBF Parliamentary State Secretary, Thomas Rachel, as well as the chairman of the Board of Directors of the Forschungszentrum Jülich, Prof. Dr.-Ing. Wolfgang Marquardt, TUM president, Prof. Dr. Thomas F. Hofmann, and the architect of the buildings, Prof. Dr.-Ing. Gunter Henn, were present.

A further successful event has been moved to an online format: The yearly MLZ User Meeting. In 2020, it was held in conjunction with the German Neutron Scattering Conference (DN). The high number of 405 participants exemplifies the success of the online format.

On a personal note, we would like to thank and bid farewell to Dr. Anton Kastenmüller after two five-year terms as Technical Director of the FRM II and warmly welcome Dr. Axel Pichlmaier as his successor.

According to our new slogan: Neutrons for Research and Innovation, we hope for a year 2021 full of neutrons! We are prepared to deliver them and hopefully, all the challenging boundary conditions will allow us to do so.



Peter Müller-Buschbaum



Stephan Förster



Axel Pichlmaier



Robert Rieck

Scientific Highlights & Reports

Investigation of promising high strength materials	10
How stony-iron meteorites form.....	11
Sustainable method for disintegrating wood.....	12
Surprising reaction of magnetic nanoparticles to magnetic fields.....	13
New materials for next generation Lithium-ion batteries	14
Elucidating the reaction pathway of vitamin C.....	15
Nanostructures in a straight line.....	16
Understanding Multiple Sclerosis on a molecular level	17
North Pole without South Pole.....	18
A milestone on the road to creating an electron-positron plasma	19

Materials Science

Investigation of Li intercalation into Si/C anodes using neutron diffraction	20
The structure of a deep eutectic solvent at a solid electrode	21
Operando neutron depth profiling on battery electrodes	22
Martensite distribution in austempered ductile iron visualised by neutron imaging.....	23
Enhancing the high temperature strength of a Co-base superalloy	24
Work hardening and softening behaviour of pure Mg influenced by Zn addition	25
Magnetic flux guidance in electrical steel employing stress induced by embossing	26
Nondestructive residual stress assessment of post weld treatment effect.....	27
Neutron imaging of steel weldments using a B-alloyed filler material	28
Neutron imaging study of a thermochemical heat storage reactor	29
PGAA and ibNAA as tools to characterise biomonitors of air pollution.....	30

Quantum Phenomena

Multipolar excitations in a rotating field — new dimension to neutron spectroscopy	31
Stripe discommensuration and spin dynamics of half-doped $\text{Pr}_{3/2}\text{Sr}_{1/2}\text{NiO}_4$	32
Direct evidence for anisotropic 3D magnetic excitations in a hole-doped antiferromagnet.....	33
2D ferromagnetic behaviours in a van der Waals honeycomb lattice.....	34
Uniaxial c-axis pressure effects on the underdoped superconductor $\text{BaFe}_2(\text{As}_{0.72}\text{P}_{0.28})_2$	35
Low-temperature spin dynamics of ferromagnetic molecular ring $\{\text{Cr}_8\text{Y}_8\}$	36
Evolution of magnetocrystalline anisotropies in $\text{Mn}_{1-x}\text{Fe}_x\text{Si}$	37
Anisotropic fractal magnetic domain pattern in bulk $\text{Mn}_{1.4}\text{PtSn}$	38
Magnetic correlations in polycrystalline $\text{Tb}_{0.15}\text{Co}_{0.85}$ studied using magnetic SANS	39
Waveguide-enhanced PNR study of magnetism of iridate/manganite bilayer.....	40
Tuning the Co/Sr stoichiometry in $\text{SrCoO}_{2.5}$ by RHEED assisted MBE growth	41

Soft Matter

How do peptides kill bacteria – an insight from neutron scattering	42
Polymeric micelles and gels as nanocarriers for miltefosine delivery.....	43
Thylakoid membrane reorganisations and non-photochemical quenching	44
Smart bottle brushes as seen by neutrons.....	45

A new green surfactant based on sugars as a viscosity modifier in a wide temperature range	46
Fluctuation suppression in microgels by polymer electrolytes.....	47
Interaction between phosphocholine-decorated SPIONs and human plasma proteins	48
Characterisation of omega-3 enriched membranes sheds light on their biological role	49
Polymorphic phase transition in supercritical (SC) carbon dioxide.....	50
Calcium drives the structural organisation of iron-organic matter aggregates	51

Structure Research

Neutron diffraction experiments on green fluorescent protein.....	52
Structure and diffusion pathways in $\text{Li}_6\text{PS}_5\text{Cl}$ argyrodite	53
Quantification of lithium and electrolyte losses in Li-ion batteries	54
Li-ion battery degradation investigated using neutron powder diffraction	55
Single-crystal neutron diffraction of garnet-type $\text{Li}_6\text{La}_3\text{ZrTaO}_{12}$	56
Structural and chemistry changes in VO_2F cathode during Li insertion.....	57
In-situ neutron diffraction study of fatigue in Li-ion batteries	58
Low temperature crystal structure of the unconventional spin-triplet superconductor UTe_2	59
Magnetic structures of Eu and Mn sublattices in EuMnBi_2	60
Investigation of inelastic scattering of the orthorhombic $\text{Cs}_2\text{CuCl}_{1.8}\text{Br}_{2.2}$ compound.....	61
Neutron and X-ray single-crystal diffraction in diamond anvil cells	62
Semiconductor nanocrystals as scintillators for fast neutron imaging.....	63
Boron-based scintillator screens provide neutron imaging improvement.....	64
Fast neutron irradiation for green biodiesel production	65
GINSES: dancing of polymer chains at solid interfaces	66
Non-stationary neutron diffraction on surface acoustic waves	67
Neutron larmor diffraction on powder samples.....	68
Neutron MIEZE spectroscopy with focal length tuning.....	69
Clamp cells for high pressure neutron scattering at the MLZ.....	70
Determination of k_0 factors for non-1/v nuclides.....	71

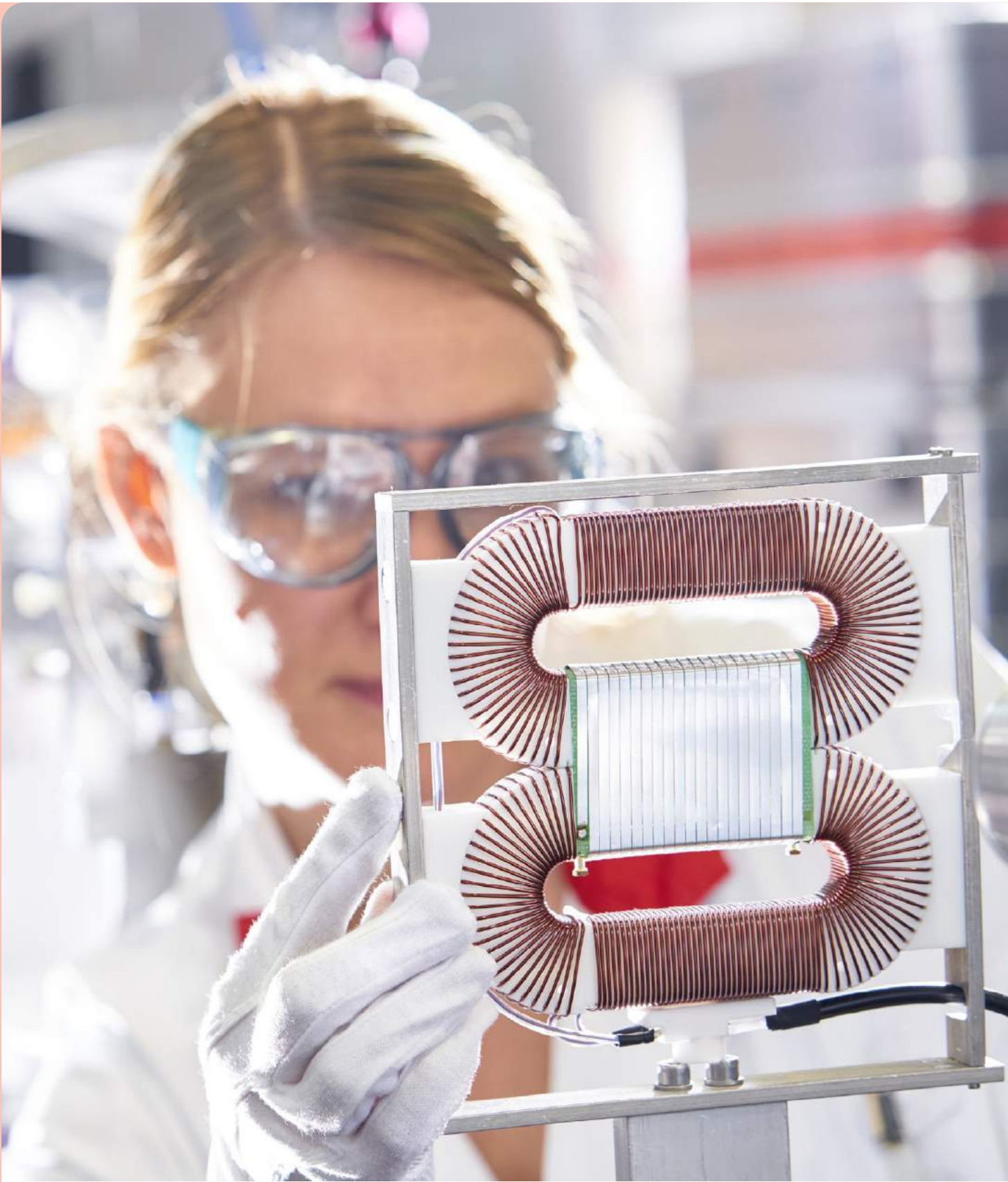
Reactor & Development

Finally: Fresh neutrons on the horizon	74
Conversion of the FRM II: Progress in fuel manufacturing and simulation.....	76

Facts & Figures

The year in pictures.....	80
Awards.....	84
Workshops, Conferences and Schools	85
Between dinosaur eggs and the discharge of C-14	86
At the User Office in the era of the pandemic.....	88
Organisation	90
Staff	92
Budget.....	93
Publications & Theses.....	94
Partner institutions.....	102
Imprint.....	106

Dr. Johanna Jochum, instrument scientist at the resonance spin echo spectrometer RESEDA, examining a resonant spin flipper.



Scientific Highlights & Reports

Investigation of promising high strength materials

Carbon nanotube reinforced aluminum matrix composites are a promising material for aerospace applications due to their high strength-to-weight ratio. However, a fundamental issue of this material is the lack of quantitative evaluation of the load transfer effect caused by the carbon nanotubes during loading. Therefore, Chinese and German scientists conducted in-situ neutron diffraction on the tensile deformation of the composite and the unreinforced aluminum alloy. A microstructure based computational model was also developed and verified to predict the mechanical behaviour of the composite. From the approach developed in this work, it is possible to track the load transfer effect of the carbon nanotubes during loading of their metal matrix composites. This will help researchers to optimise practical production methods for maximum utilisation of the spectacular mechanical properties of the carbon nanotubes, resulting in the development of new high-performance metal composites in the future.

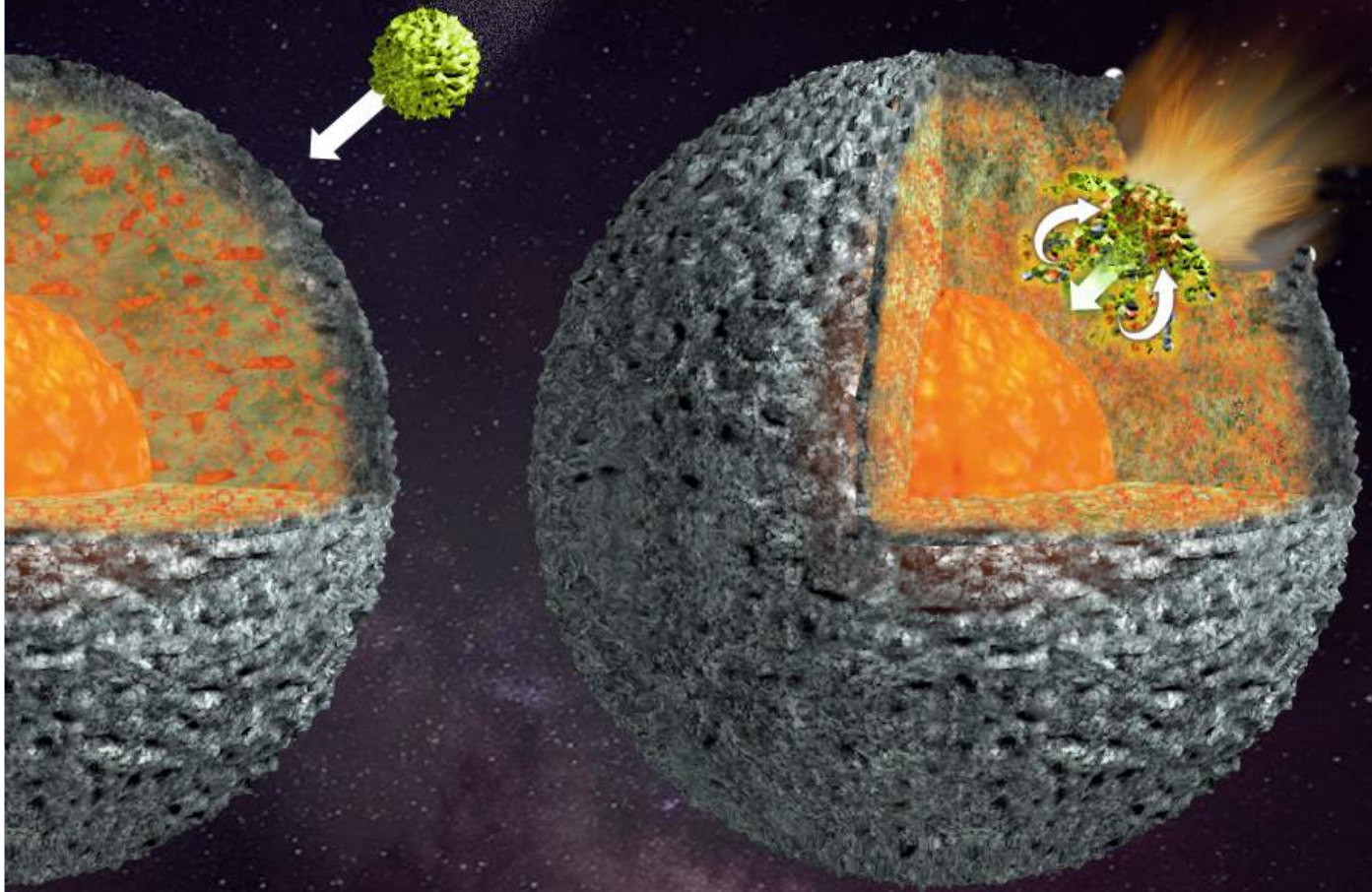
The experiments were carried out at STRESS-SPEC.

X. X. Zhang, J. F. Zhang, Z. Y. Liu, W. M. Gan, M. Hofmann, H. Andrä, B. L. Xiao, Z. Y. Ma, Microscopic stresses in carbon nanotube reinforced aluminum matrix composites determined by in-situ neutron diffraction, Journal of Materials Science & Technology, 54, 58 (2020)



First author, Dr. Xingxing Zhang, at the diffractometer STRESS-SPEC.

Impact of a small asteroid on a larger one. During the impact, molten iron from the core of the impacting body mixes with the olivine-rich coat of the parent body.



How stony-iron meteorites form

Meteorites are the oldest accessible building blocks of our solar system that provide a window into the processes that shaped the formation of Earth and the other planets 4.5 billion years ago. Pallasites belong to the noteworthy group of stony-iron meteorites whose exact origins have remained highly controversial despite decades of research.

To solve this puzzle, German and British scientists investigated pallasite formation by experimentally simulating one possible origin: a collision of two celestial bodies. This required rapid deformation at 1300°C and a pressure of 10 kbars. In a first, they succeeded in producing the structures of all types of pallasites, which has confirmed that pallasites are formed in the rocky mantle of an asteroid that is mixed with the liquid core of a colliding body. Their results also shed new light on the impact process and the evolution of the parent body before and after the collision, which will be investigated in more detail in future studies.

The experiments were carried out at SAPHiR.

N. P. Walte, G. F. D. Solferino, G. J. Golabek, D. Silva Souza, A. Bouvier, Two-stage formation of pallasites and the evolution of their parent bodies revealed by deformation experiments, Earth Planet Sci Lett, 546, 116419 (2020)

Sustainable method for disintegrating wood

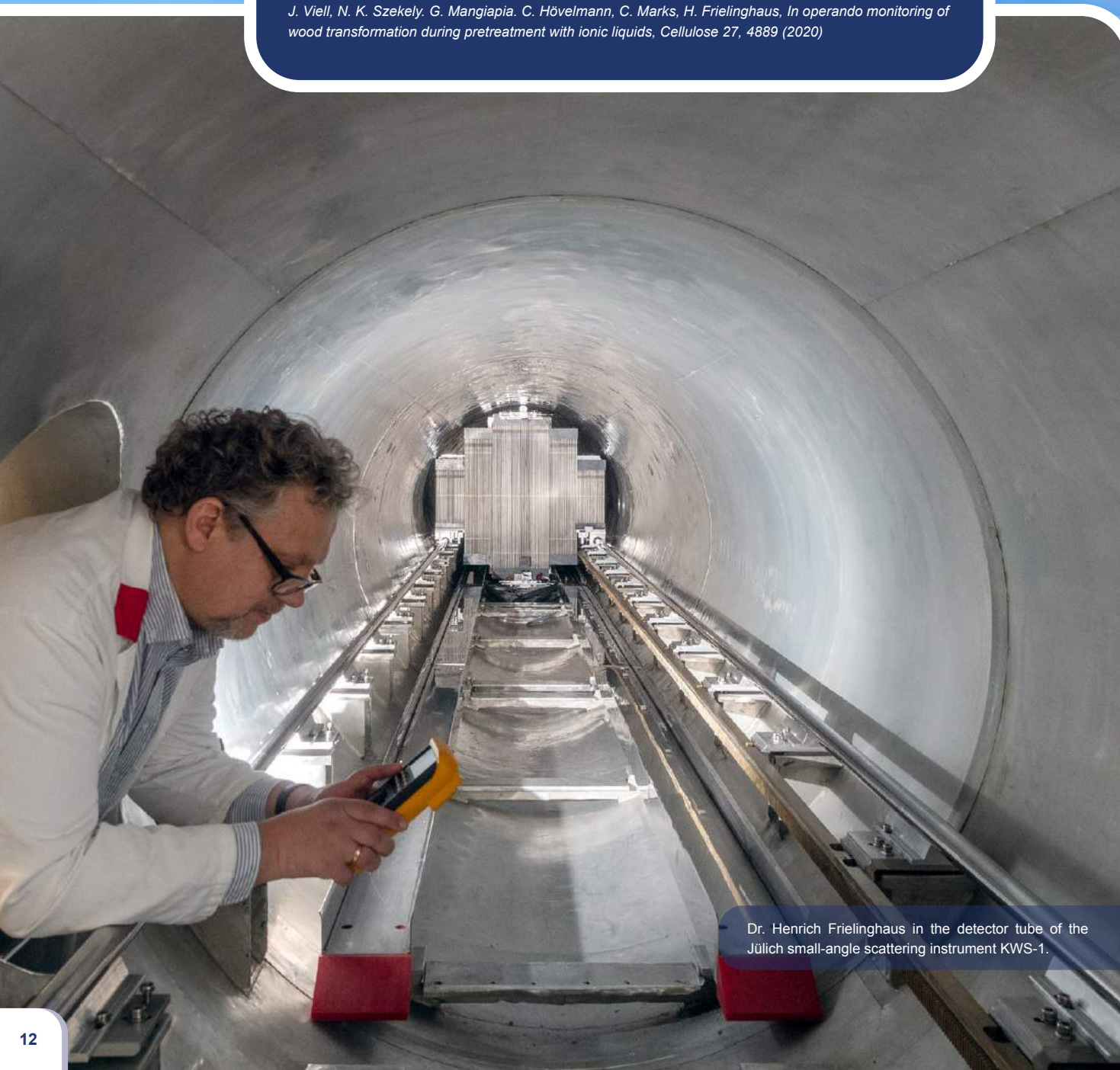
Wood contains cellulose and lignin. The molecules have great potential as a sustainable alternative to fossil resources, such as biodegradable plastics.

However, it is not easy to isolate cellulose and lignin from wood as the molecules are interwoven with each other and do not readily dissolve in common solvents. The energy- and water-intensive boiling processes used in paper production are too aggressive. Scientists from Germany used a more gentle process: ionic liquids, salts that liquefy at temperatures below 100°C. The liquids allow wood to swell and partially dissolve within minutes. Cellulose and lignin are then accessible for further processing.

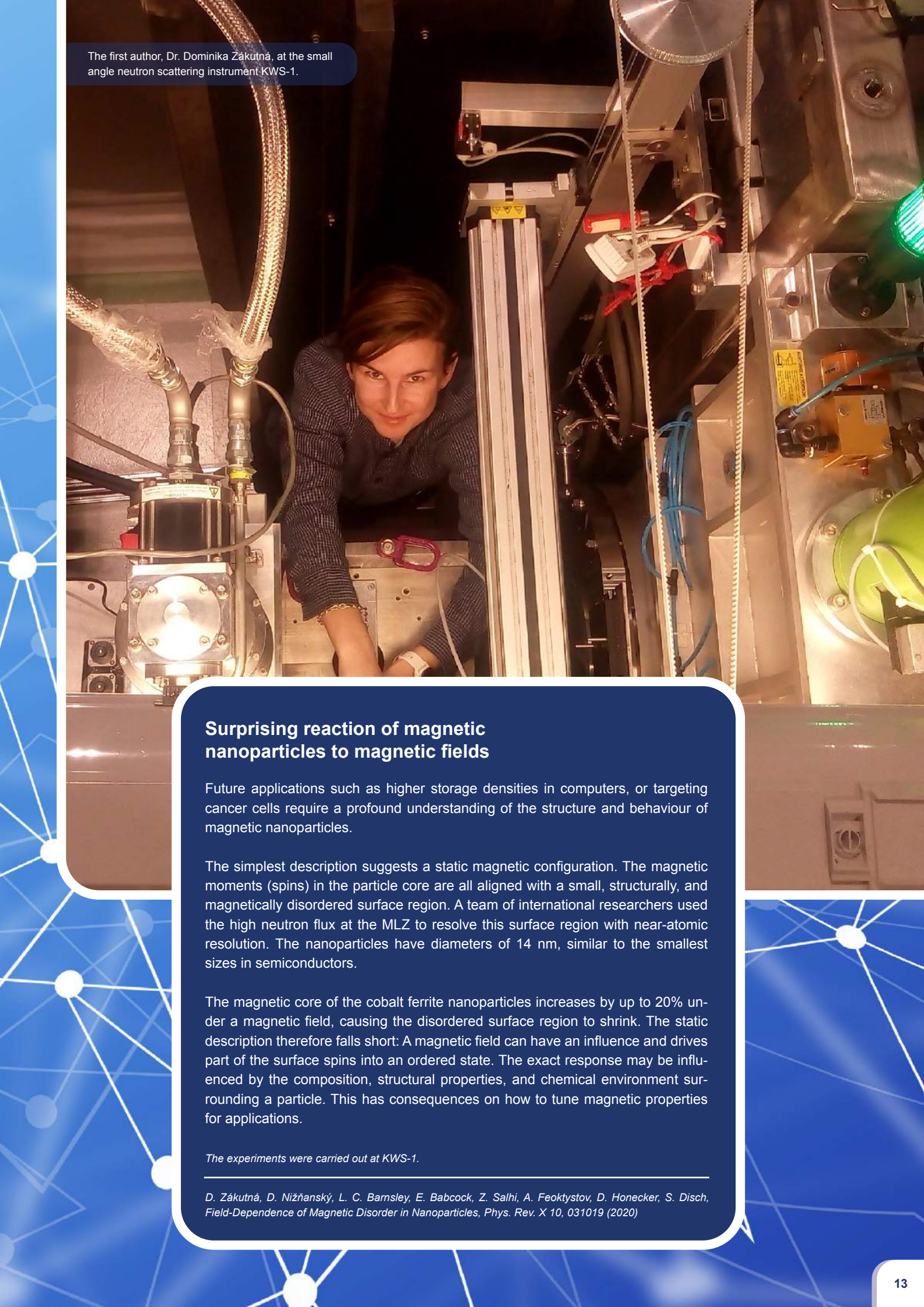
Ionic liquids are expensive, but can be largely reused. By optimising the soaking time or temperature, they stand to become of interest to industry. In order to understand how liquid and wood interact, the researchers used small angle neutron scattering. They followed the process for the first time and were thus able to divide it into individual stages and resolve them in space and time.

The experiments were carried out at KWS-1.

J. Viell, N. K. Szekely, G. Mangiapia, C. Hövelmann, C. Marks, H. Frielinghaus, In operando monitoring of wood transformation during pretreatment with ionic liquids, Cellulose 27, 4889 (2020)



Dr. Henrich Frielinghaus in the detector tube of the Jülich small-angle scattering instrument KWS-1.



The first author, Dr. Dominika Zákutná, at the small angle neutron scattering instrument KWS-1.

Surprising reaction of magnetic nanoparticles to magnetic fields

Future applications such as higher storage densities in computers, or targeting cancer cells require a profound understanding of the structure and behaviour of magnetic nanoparticles.

The simplest description suggests a static magnetic configuration. The magnetic moments (spins) in the particle core are all aligned with a small, structurally, and magnetically disordered surface region. A team of international researchers used the high neutron flux at the MLZ to resolve this surface region with near-atomic resolution. The nanoparticles have diameters of 14 nm, similar to the smallest sizes in semiconductors.

The magnetic core of the cobalt ferrite nanoparticles increases by up to 20% under a magnetic field, causing the disordered surface region to shrink. The static description therefore falls short: A magnetic field can have an influence and drives part of the surface spins into an ordered state. The exact response may be influenced by the composition, structural properties, and chemical environment surrounding a particle. This has consequences on how to tune magnetic properties for applications.

The experiments were carried out at KWS-1.

D. Zákutná, D. Nižňanský, L. C. Barnsley, E. Babcock, Z. Salhi, A. Feoktystov, D. Honecker, S. Disch, Field-Dependence of Magnetic Disorder in Nanoparticles, Phys. Rev. X 10, 031019 (2020)

New materials for next generation Lithium-ion batteries

$\text{LiNi}_x\text{Co}_y\text{Mn}_{1-x-y}\text{O}_2$ (NCM) intercalation compounds have been found to be promising cathode materials for next-generation lithium-ion batteries. The properties of the NCM cathodes are dependent on the relative amounts of Nickel, Cobalt, and Manganese, making it a challenge to control the exact structure of NCM cathode materials and to understand the mechanisms during electrochemical cycling. Therefore, a universal and simple synthetic strategy was developed to synthesise the NCM material composed of an inner Ni-rich core and a Mn-rich shell. The neutron experiments of an international group of scientists provide a new perspective for the rational design of layered Ni-based cathode materials with high energy density and long cycle life. As mining for Cobalt is especially detrimental to the environment, the synthetic route is currently being utilised to synthesise Co-free NCM cathode materials.

The experiments were carried out at SPODI.

*W. Hua, B. Schwarz, R. Azmi, M. Müller, M. Susana D. Darma, M. Knapp, A. Senyshyn, M. Heere, A. Missyul, L. Simonelli, J. R. Binder, S. Indris, H. Ehrenberg, Lithium-ion (de)intercalation mechanism in core-shell layered $\text{Li}(\text{Ni}, \text{Co}, \text{Mn})\text{O}_2$ cathode materials, *Nano Energy* 78, 105231 (2020)*



Dr. Anatoliy Senyshyn examining a Lithium-ion battery at the structure powder diffractometer SPODI.

Adjusting the crystal at the diffractometer BioDiff.

Elucidating the reaction pathway of vitamin C

Enzymes catalyse and control all biochemical reactions in organisms. The enzyme ascorbate peroxidase belongs to the group of haem enzymes and is responsible for converting toxic hydrogen peroxide into water. To do this, protons and electrons need to be transferred to hydrogen peroxide from ascorbic acid – better known as vitamin C.

The usual methods of X-ray crystallography do not show where protons reside in enzymes. To be able to examine the proton transfer in such biochemical reactions, neutrons are required to make them visible.

Using neutron scattering, German, British and French scientists clarified the path of proton transfer in ascorbate peroxidase. This path includes the release and uptake of protons by amino acids and the transport of protons via a chain of water molecules. They discovered that in the enzyme the normal solution balance of the proton chemistry of an amino acid is significantly altered to enable this pathway. The results open the way for an understanding of similar reactions in the whole class of haem enzymes.

The experiments were carried out at BioDiff.

H. Kwon, J. Basran, J. M. Devos, R. Suardiaz, M. W. van der Kamp, A. J. Mulholland, T. E. Schrader, A. Ostermann, M. P. Blakeley, P. C. E. Moody, E. L. Raven, Visualizing the protons in a metalloenzyme electron proton transfer pathway, PNAS 117, 6484 (2020)

Nanostructures in a straight line

Skyrmions can be described as nanoscale vortices in the magnetic alignment of atoms and were discovered using neutrons at the FRM II in 2009. Magnetism depends on the orientation of the atom spins. Spins can be imagined as bar magnets and can be arranged parallel or in a criss-cross fashion. By applying an electrical current, it is possible to create vortices of those spins, the skyrmions.

An international team of researchers has created a new type of skyrmion in which the interior spins are arranged in opposite, antiparallel directions to one another, which is referred to as antiferromagnetic. The advantage of these antiferromagnetic skyrmions is that they are much easier to control: They can be moved in a straight line under application of an electrical current.


Future technical applications of antiferromagnetic skyrmions could be an increase in the data density and energy efficiency in storage media, the improvement of classical data processing and quantum computing.

The experiments were carried out at PANDA.

S. Gao, H.D. Rosales, F.A. Gómez Albarracín, V. Tsurkan, G. Kaur, T. Fennell, P. Steffens, M. Boehm, P. Čermák, A. Schneidewind, E. Ressouche, D.C. Cabra, C. Rüegg, O. Zaharko, Fractional antiferromagnetic skyrmion lattice induced by anisotropic couplings, Nature 586, 37 (2020)



Instrument scientist Dr. Astrid Schneidewind at the three axes spectrometer PANDA.



The magnetic reflectometer MARIA in the neutron guide hall of the MLZ.

Understanding Multiple Sclerosis on a molecular level

In Multiple Sclerosis, the myelin layers surrounding the axons of the nerve cells are perturbed and disintegrate. Depending on the course of the disease, this leads to neurological deficits, cognitive disorders and, ultimately, to death. There is no cure for the disease, partly because very little is known about it at a molecular level. Previous studies observed that changes in the myelin lipid composition lead to instabilities and enhanced local curvature of Myelin Basic Protein-lipid multilayer structures.

The researchers used neutrons to investigate the molecular origin of the instability and found that the diseased lipid membrane exhibits lower bending stiffness, destabilising smooth structures with a radius of curvature greater than 1 μm . The findings might offer strategies for remyelination, thereby leading to a significant advance in the treatment of Multiple Sclerosis.

The experiments were carried out at KWS-2 and MARIA.

B. Krugmann, A. Radulescu, M.-S. Appavou, A. Koutsioubas, L. R. Stingaciu, M. Dulle, S. Förster, A. M. Stadler, Membrane stiffness and myelin basic protein binding strength as molecular origin of multiple sclerosis, Sci. Rep. 10, 16691 (2020)

North Pole without South Pole

If we break a magnet into two pieces, we expect to get a north and a south pole in each of them. An international team of researchers has now for the first time detected magnetic monopoles in a material that conducts electricity.

Atoms occupy fixed places in a strict order within crystals. This can sometimes be difficult because of the repulsive forces. For example, in frozen water the atoms obey the ice rule: Oxygen needs to have exactly two strong and two weak bonds to neighbouring hydrogen in order to fit into this fixed order.

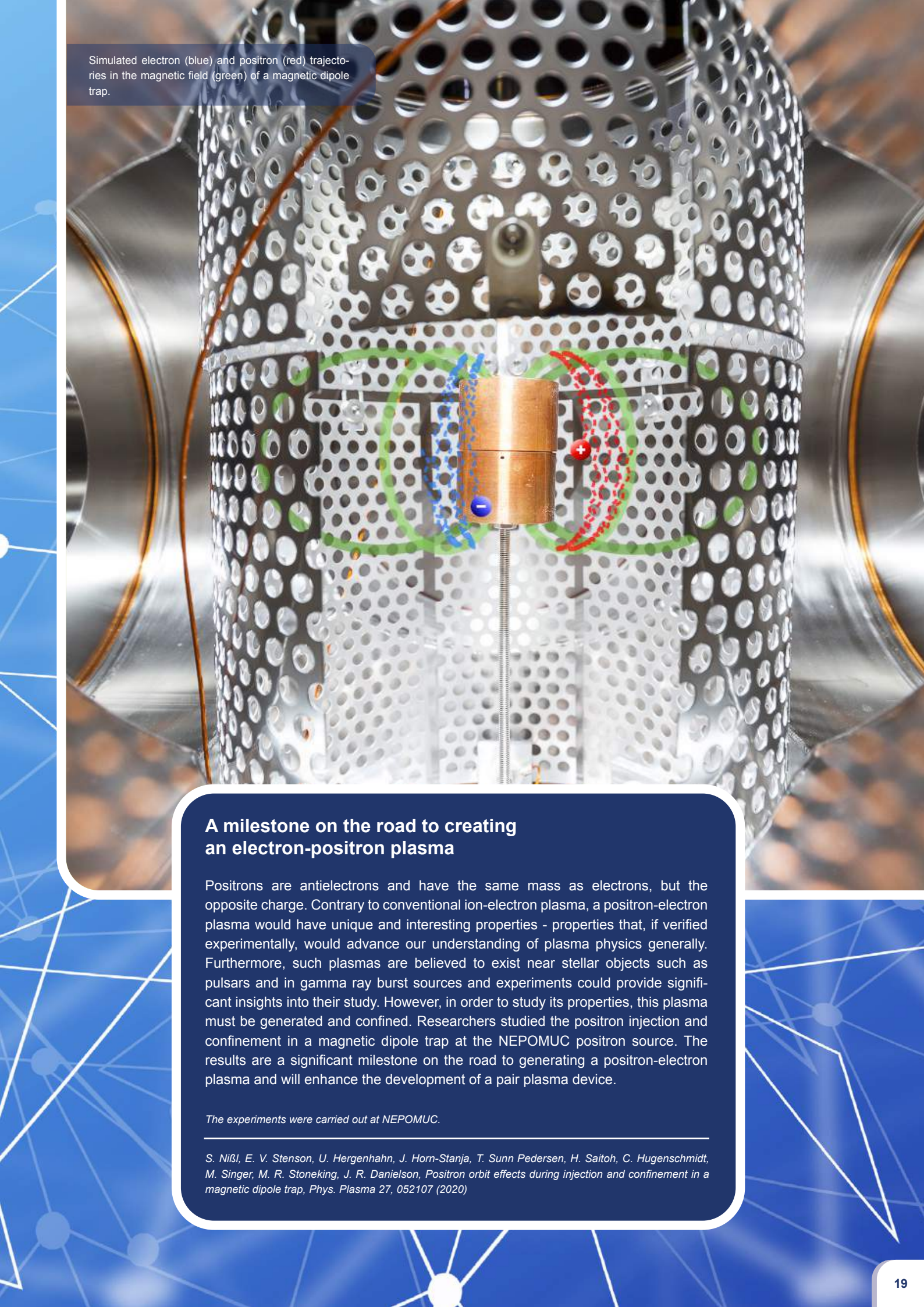
Similar behaviour was also proposed for the magnetic materials. Using neutron diffraction, the researchers have discovered Kagome spin-ice in intermetallic HoAgGe. „Kagome“ is the Japanese word for „basket grid“. The atomic arrangement similar to triangles that are connected as in woven baskets has been a theoretical concept until now. The triangular arrangement prevents the parallel alignment of atom spins, which is the reason for magnetism, in the usual way. As for water molecules in ice, the possibilities of spin orientations in HoAgGe are limited. Therefore, Kagome spin-ice behaves as if it contains magnetic monopoles.

The experiments were carried out at POLI.

K. Zhao, H. Deng, H. Chen, K. A. Ross, V. Petříček, G. Guenther, M. Russina, V. Hutanu, P. Gegenwart, Realization of the kagome spin ice state in a frustrated intermetallic compound, Science 367, 1218 (2020)



Instrument scientist and co-author Dr. Vladimir Hutanu with his colleague Henrik Thoma at the polarised neutron diffractometer POLI.



Simulated electron (blue) and positron (red) trajectories in the magnetic field (green) of a magnetic dipole trap.

A milestone on the road to creating an electron-positron plasma

Positrons are antielectrons and have the same mass as electrons, but the opposite charge. Contrary to conventional ion-electron plasma, a positron-electron plasma would have unique and interesting properties - properties that, if verified experimentally, would advance our understanding of plasma physics generally. Furthermore, such plasmas are believed to exist near stellar objects such as pulsars and in gamma ray burst sources and experiments could provide significant insights into their study. However, in order to study its properties, this plasma must be generated and confined. Researchers studied the positron injection and confinement in a magnetic dipole trap at the NEPOMUC positron source. The results are a significant milestone on the road to generating a positron-electron plasma and will enhance the development of a pair plasma device.

The experiments were carried out at NEPOMUC.

S. Nißl, E. V. Stenson, U. Hergenrohn, J. Horn-Stanja, T. Sunn Pedersen, H. Saitoh, C. Hugenschmidt, M. Singer, M. R. Stoneking, J. R. Danielson, *Positron orbit effects during injection and confinement in a magnetic dipole trap*, *Phys. Plasma* 27, 052107 (2020)

T. Waldmann¹, K. Richter¹, N. Paul², N. Jobst¹, R.-G. Scurtu¹, M. Hofmann², R. Gilles², M. Wohlfahrt-Mehrens¹

¹ZSW – Zentrum für Sonnenenergie- und Wasserstoff-Forschung, Baden-Württemberg, Ulm, Germany; ²Heinz Maier-Leibnitz Zentrum (MLZ), Technical University of Munich, Garching, Germany

The requirements for future generations of Li-ion batteries are high specific energy, a fast-charging capability, a high safety level, and longer life-time. In the current gradual improvement of batteries, Si compounds (<5% Si) are blended with graphite materials to increase the specific energy. However, there is a lack of knowledge e.g. on the charging mechanism and the reaction with deposited Li plating on Si/C composite anodes.

In our study at the neutron source FRM II [1], commercial 18650-type cells (anode: 3.5 wt.-% Si / graphite, cathode: NCA) were investigated at the STRESS-SPEC instrument. Diffractograms and electrochemical data acquired simultaneously during operation of the cells allowed an analysis of the mechanistic details during charging, as well as in the relaxation after charging.

Although the amorphous Si material did not allow the lithiation of the Si alloy to be followed directly, it can indirectly be observed by the relaxation of the LiC_6 and LiC_{12} Bragg peaks. We find that the speed of charging (investigated in the range of 0.1C to 0.75C) is decisive for the charging mechanism at -21°C . For charging at a rate of 0.75C, the data clearly indicate Li metal deposition on the anode during charging, as well as re-intercalation of the deposited Li into graphite upon the end of charging. As shown in Fig. 1, Li is transferred from graphite to the Si compound when the re-intercalation of Li has been completed.

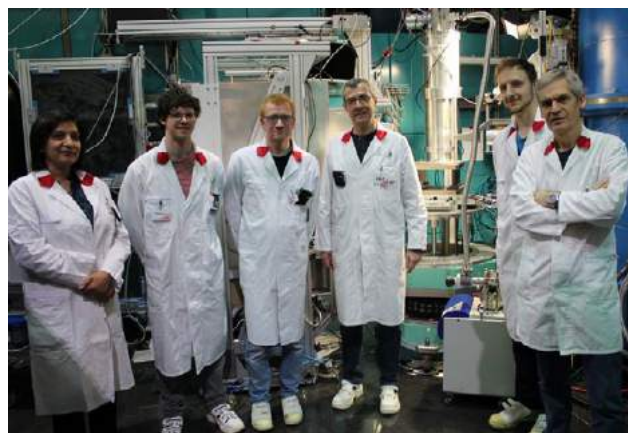


Fig. 2: Team conducting the experiments at the STRESS-SPEC instrument (left to right): Dr. Neelima Paul (TUM), Nicola Jobst (ZSW), Dr. Thomas Waldmann (ZSW), Dr. Rares-George Scurtu (ZSW), Dr. Karsten Richter (ZSW), Dr. Ralph Gilles (TUM).

Most interestingly, this reveals a synergetic effect of the Si compound and graphite: Graphite acts as a kinetic buffer to store Li^+ ions during charging. During the relaxation after charging, a proportion of the Li^+ ions are transferred from graphite to the Si compound. These results significantly enhanced our knowledge of the charging, relaxation and aging mechanisms of Li-ion batteries with Si/C composite anodes, and suggest possibilities for tailoring the anodes of future generations of batteries.

[1] K. Richter et al., *Low-Temperature Charging and Aging Mechanisms of Si/C Composite Anodes in Li-Ion Batteries: An Operando Neutron Scattering Study*, *ChemSusChem*, 13, 529 (2020)

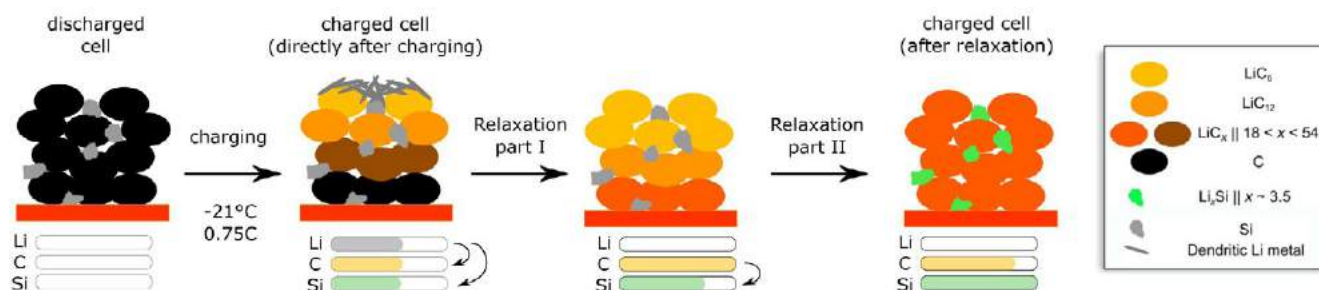


Fig. 1: Illustration of relaxation processes after charging of Si/C composite anodes. Image adapted from [1].

N. Zec¹, G. Mangiapia¹, M. Zheludkevich^{2,3}, S. Busch¹, J.-F. Moulin¹

¹German Engineering Materials Science Centre (GEMS) at MLZ, Helmholtz-Zentrum hereon GmbH, Garching, Germany; ²Institute of Surface Science, Helmholtz-Zentrum hereon GmbH, Geesthacht, Germany; ³Institute for Materials Science, Faculty of Engineering, Kiel University, Kiel, Germany

In the search for solvents for electrochemical applications, deep eutectic solvents (DES) have emerged as a game-changing class of materials. These environmentally friendly mixtures of hydrogen bond donors and acceptors offer outstanding stability with low production costs, and can be optimised for use down to sub-ambient temperatures. The present work focuses on the elucidation of the electrode/liquid interface structure in the context of using DES as electrolytes for the electrodeposition of metals.

Previous experimental work has suggested that an ordered layer of DES might build up at the electrode and prevent the diffusion of metallic ions from the solution to the interface, but no detailed description of this hypothetical layer is available. Our approach to this problem is based on the cross validation of experimental measurements and atomistic computer simulations. The interfacial structure was probed by neutron reflectometry (NR) at the instrument REFSANS, and the model used for data analysis was constructed using MD simulations. Three different isotopic compositions were used for the NR characterisation, some potentially enhancing the contrast of an interfacial layer (either component of the DES being in turn hydrogenated or deuterated). The measurements were repeated at three electrical potentials in order to identify electrostatic effects on the hypothetical layer.

As seen in Fig. 1, the simulated NR curves for a DES distribution without any layering deviate strongly from the measured ones, excluding this possibility. In contrast, the model including a layer modeled after the simulations reproduces all experimental curves accurately. Given the lack of strong scattering features, it would have been difficult to provide a detailed structural model based on the NR data alone. MD simulations alone hint at an interfacial layering but with no guarantee that the proposed structure is actually the one present at equilibrium.

Combining the experiments and the simulations offers the best of both worlds. It validates the existence of a dense interfacial layer hindering diffusion toward the electrode and provides details on its structure. These insights can now be used to develop new molecules in order to avoid this ordered layer and allow metallic ions to reach the surface. The work presented here is not only a contribution to the field of DES research, but also a methodological effort showing how scattering experiments and MD simulations can benefit from each other, in a good example of the so called "digital twin".

[1] N. Zec et al., *Revealing the interfacial nanostructure of deep eutectic solvents at a solid surface*, *Phys. Chem. Chem. Phys.* 22, 12104 (2020)

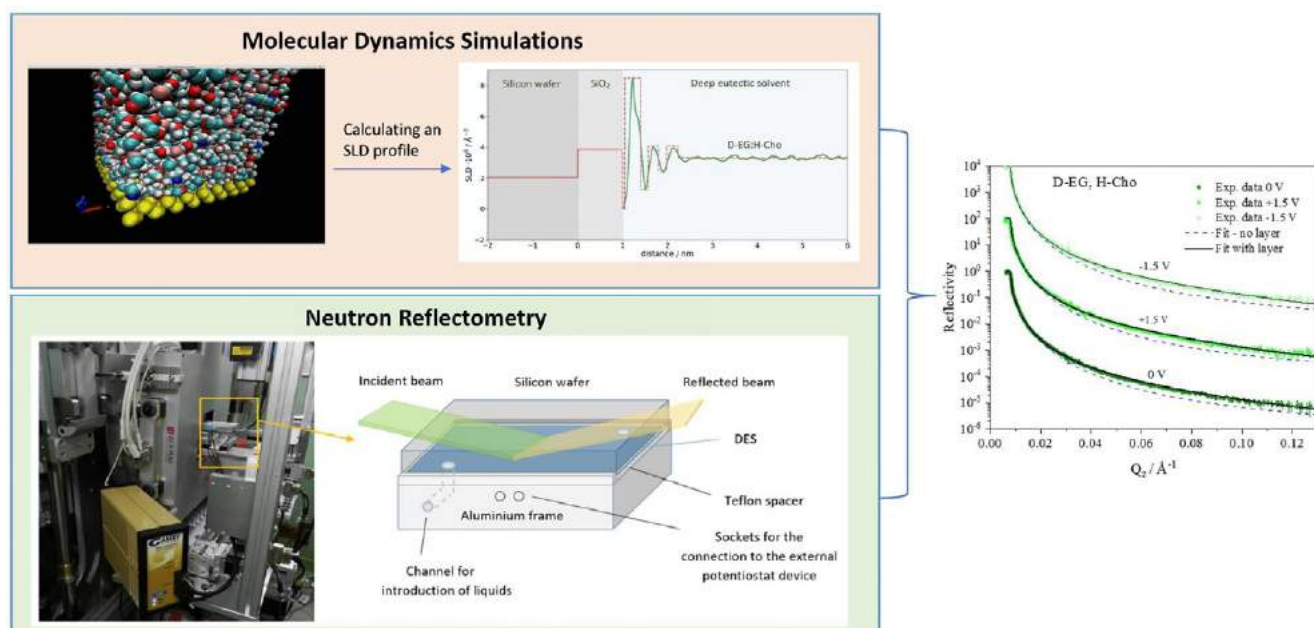


Fig. 1: Neutron reflectivity for different H/D contrasts as a function of momentum transfer Q_z for the Si/SiO₂/DES interface with and without applied potential. Reflectivity curves for +1.5 V and -1.5 V are scaled for clarity by factors 10^2 and 10^4 respectively. Dashed lines are calculated for a Si/DES model without a DES layer at the interface. Drawn-out lines include a structured DES layer at the interface.

Operando neutron depth profiling on battery electrodes

M. Trunk^{1,2}, F. Linsenmann³, P. Rapp³, L. Werner², R. Gernhäuser², R. Gilles¹, B. Märkisch², Z. Revay¹, H. A. Gasteiger³¹Heinz Maier-Leibnitz Zentrum (MLZ), Technical University of Munich, Garching, Germany; ²Physics Department, Technical University of Munich, Garching, Germany; ³Chair of Technical Electrochemistry, Department of Chemistry, Technical University of Munich, Garching, Germany

The recently installed Neutron Depth Profiling instrument 'N4DP' at the PGAA facility of the MLZ allows the non-destructive near-surface quantification of the concentration profiles of light nuclides such as ³He, ¹⁰B, ⁶Li, ¹⁴N, and ¹⁷O in almost any material matrix. Upon neutron capture, these nuclides emit charged particles that traverse through the host material. On their way, they lose energy and their depth of production can be determined with a high resolution down to tens of nanometers. NDP enables the quantification of the lithium concentration profile in electrodes for lithium-ion batteries, complementing electrochemical measurements of the performance of the whole battery. However, common battery casings such as coin, pouch or cylindrical cells cannot be penetrated by the charged particles. Hence, we used a newly designed coin-cell battery casing close to the commercial standard to measure thin electrodes for the first time, as shown in Fig. 1 [1]. A Kapton[®] foil with a nominal thickness of 7.5 μm is glued into the cap, thereby sealing the processed holes and preventing leakage of the liquid electrolyte. It acts as a substrate for the 100 nm thin copper current collector and the graphite electrode. The foil blocks α particles but is permeable for the ³H particles emitted by the ⁶Li(n,α)³H reaction. We obtained lithium concentration profiles during battery operation from the ³H spectra, taking into account the energy losses of the different layers and the stopping power of the electrode. The profile changes from the pristine state (1) during the first three half-cycles,

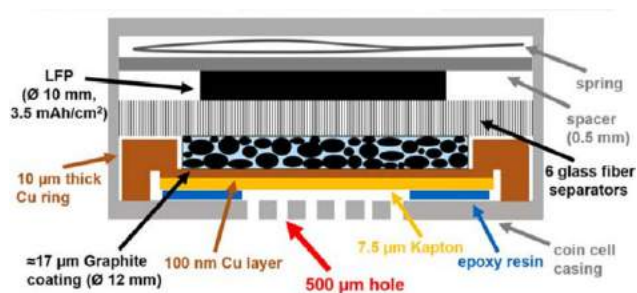


Fig. 1: Schematic overview of the battery cell developed for operando NDP. From [1].

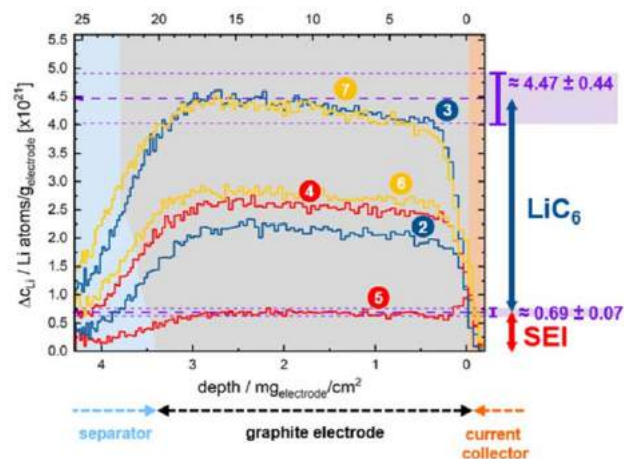


Fig. 2: Lithium concentration profiles measured in the graphite anode using NDP. During (dis)charging at C/16 the (de)lithiation of reversible and the formation of irreversible lithium can be monitored. From [1].

cycled at C/16, as shown in Fig. 2. Upon first charging (2, 3), the lithium concentration increases roughly homogeneously across the entire electrode. During discharging, lithium is reversibly extracted from the graphite electrode (4, 5) until the battery is fully discharged and only lithium remains in the electrode, which is irreversibly bound in the solid-electrolyte-interphase (SEI) (5). The reversibly extracted amount of lithium fits well to an expected LiC_6 phase measured electrochemically via the reversible capacity (difference between (3) and (5)). However, the electrochemically measured irreversible capacity is significantly higher than the lithium irreversibly bound in the SEI (5) measured via NDP. A possible explanation could be that significant amounts of Li-containing compounds in the SEI dissolve in the electrolyte during the first cycle. This project is supported by the Federal Ministry of Education and Research (BMBF) under contracts 03XP0081, 05K16WO1, and 05K19WO8.

[1] F. Linsenmann et al., A Liquid Electrolyte-Based Lithium-Ion Battery Cell Design for Operando Neutron Depth Profiling, *J. Electrochem. Soc.* 167 (10), 100554 (2020)

S. R. Soria^{1,2}, X. H. Li³, M. Schulz¹, M. Boin⁴, M. Hofmann¹

¹Heinz Maier-Leibnitz Zentrum (MLZ), Technical University of Munich, Garching, Germany; ²Laboratorio Argentino de Haces de Neutrones (LAHN), Comisión Nacional de Energía Atómica, Ciudad de Buenos Aires, Argentina; ³German Engineering Materials Science Centre (GEMS) at MLZ, Helmholtz-Zentrum hereon GmbH, Garching, Germany; ⁴Helmholtz-Zentrum Berlin für Materialien und Energie, Berlin, Germany

Austempered ductile iron (ADI) is a cast iron with high potential as a substitute for cast steels due to its lighter weight, higher tensile strength and significantly lower manufacturing cost. ADI has an ausferrite microstructure consisting of acicular ferrite (α -Fe) and high carbon enriched retained austenite (γ -Fe) as a result of dedicated heat treatment. Partial martensitic transformation of the metastable austenite to martensite (α' -Fe) was observed in ADI under plastic deformation. The evolution of the martensite content in ADI samples during a uniaxial compression test at different strain levels was studied at ANTARES by energy-selective neutron imaging. Images at different wavelengths were acquired using a double-crystal monochromator. Samples were compressed to strain levels of 10, 20, 30 and 45%. The results obtained were compared to previous studies on the same samples using neutron diffraction on the instruments STRESS-SPEC and SPODI at the MLZ.

The martensite content was determined using images acquired at wavelengths between 1.6 and 5.9 Å with a step size of 0.05 Å. The attenuation coefficient spectra obtained are presented in Fig. 1(a). An increase in the strain level is accompanied by an increase in the attenuation below the edge at $\lambda = 4$ Å, which is associated with a rise in the martensite content by the increase in the height of the α' -Fe (110) edge. Moreover, a reduction in the austenite content is seen as a reduction in the height of the γ -Fe (200) edge at around $\lambda = 3.5$ Å. The maximum difference with the neutron diffraction results was 7% vol. for a deformation level of 20% [1].

The ratio of the images acquired at $\lambda_1 = 3.9$ Å and $\lambda_2 = 4.5$ Å was used to determine the martensite distribution with a spatial resolution of 150 μm , as shown in Fig. 1(b). The incident neutron beam was normal to the load direction. An inhomogeneous distribution was found that is related to the friction between the contact faces even though lubrication was used between the samples and the compression platens. A relatively lower martensite content (white regions) is observed close to the contact faces between the samples and compression platens. On the other hand, an increase in the martensite content (dark regions) in the centre of the samples is clearly visible. Due to the friction, samples exhibit a triaxial stress state, which leads to an inhomogeneous strain field. This particular strain field may lead to an inhomogeneous distribution of the martensite in the samples with an enrichment in the regions with higher plastic strain.

These results are highly relevant as they prove that an inhomogeneous distribution of the martensite content results during the compression test. Changes in the martensite content can be followed by combining the results obtained using energy-selective neutron imaging and neutron diffraction to study the phase distribution in three dimensions.

[1] S. R. Soria et al., *Determination of martensite content and mapping phase distribution on Austempered Ductile Iron using energy-selective neutron imaging*, *Mater. Charact.* 166, 110453 (2020)

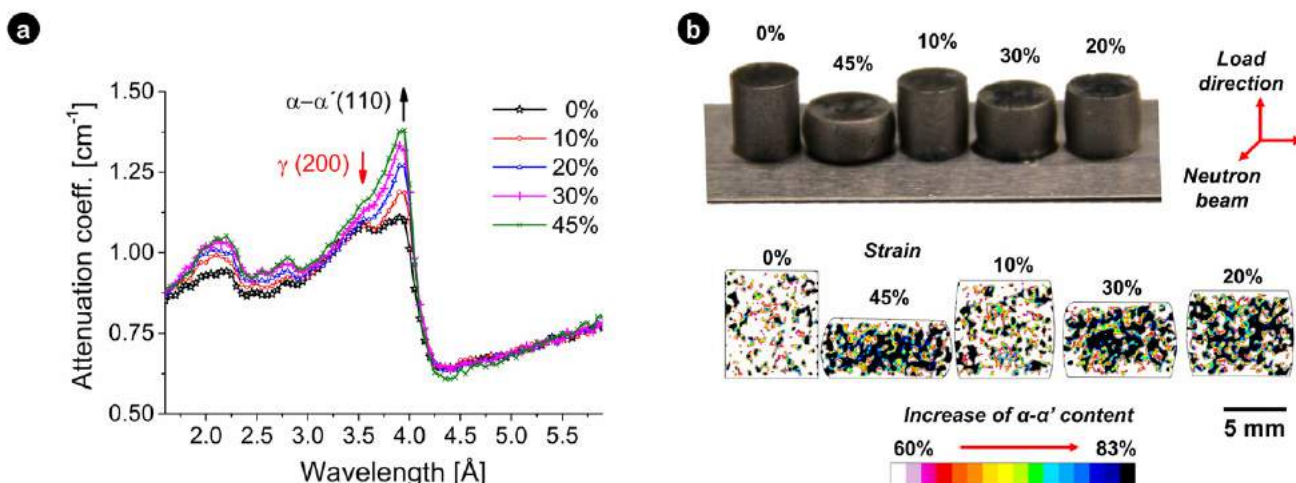


Fig. 1: (a) Experimental attenuation coefficient spectra at different deformation levels; (b) ADI samples and martensite distribution in ADI samples under different strain levels.

D. Hausmann¹, C. Solís², L. P. Freund¹, N. Volz¹, A. Heinemann², M. Göken¹, R. Gilles², S. Neumeier¹

¹Department of Materials Science and Engineering, Friedrich-Alexander-Universität Erlangen-Nürnberg, Erlangen, Germany; ²Heinz Maier-Leibnitz Zentrum (MLZ), Technical University of Munich, Garching, Germany

Compositionally complex γ/γ' CoNi-base superalloys are novel candidates with promising properties for high temperature applications. To maximise their high temperature strength, the trimodal microstructure with primary, secondary and tertiary γ' precipitates has to be optimised by adjusting the multi-step heat treatments. Since the determination of the γ' precipitate size and volume fraction is difficult via electron microscopy, in-situ and ex-situ heat treatments were performed at the small-angle neutron scattering instrument SANS-1. Due to the larger sample volume ($\approx 100 \text{ mm}^3$) with a huge number of precipitates studied, small-angle neutron scattering provides more details about the temporal evolution of the γ' precipitates at high temperatures.

The alloy CoWAlloy2 ($\text{Co}_{41}\text{-Ni}_{32}\text{-Cr}_{12}\text{-Al}_9\text{-W}_5\text{-Ti}_{0.3}\text{-Ta}_{0.2}\text{-Si}_{0.4}\text{-Hf}_{0.1}\text{-C-B-Zr}$ in at.%) investigated was vacuum arc melted, cast, homogenised at $1250^\circ\text{C} / 4 \text{ h}$ and recrystallised at $1000^\circ\text{C} / 4 \text{ h}$. Subsequent in-situ small-angle neutron scattering experiments were conducted during different age hardening heat treatments. The recorded scattering patterns were analysed, calibrated with water measurements and merged with the software BerSANS. The corrected data were fitted by log-normal size distributions for the secondary and tertiary γ' precipitates and a Porod signal that leveled out a constant incoherent background signal, using SASFit (Fig. 1d). The hardening γ' precipitates were modeled as spherical particles and the scattering factors of γ and γ' phase were calculated by using their chemical compositions, as determined by atom probe tomography.

Next to the large primary γ' precipitates (radius $\approx 150 \text{ nm}$) (Fig. 1a), only small γ' precipitates with a radius of about 5 nm were detected in the initial recrystallised condition. These γ' precipitates emerged and coarsened to a radius of about 30 nm during the first heat treatment step at 900°C (Fig. 1b). The second aging step at $750^\circ\text{C} / 16 \text{ h}$ (condition Full HT) led to a further increase of the γ' volume fraction from about 50% to 70% by precipitation of small tertiary γ precipitates with a radius of about 8 nm (Fig. 1c). Hardness as well as compression tests of the different conditions revealed that the condition $900^\circ\text{C} / 4 \text{ h} + 750^\circ\text{C} / 16 \text{ h}$ showed the maximum strength (Fig. 1e), which could be explained by the model for pair-coupling of dislocations using the SANS results.

In summary, in-situ SANS enabled the determination of the γ' volume fraction of above 70% , which is exceptionally high for a wrought alloy, and the optimum γ' precipitate size of about $30\text{-}40 \text{ nm}$ to reach the maximum strength. The in-situ monitoring of the γ' precipitate evolution at high temperatures improved the understanding of this new high temperature material significantly and led to an optimised microstructure with improved strength.

[1] D. Hausmann et al., *Enhancing the High-Temperature Strength of a Co-Base Superalloy by Optimizing the γ/γ' Microstructure*, *Metals* 10, 321 (2020)

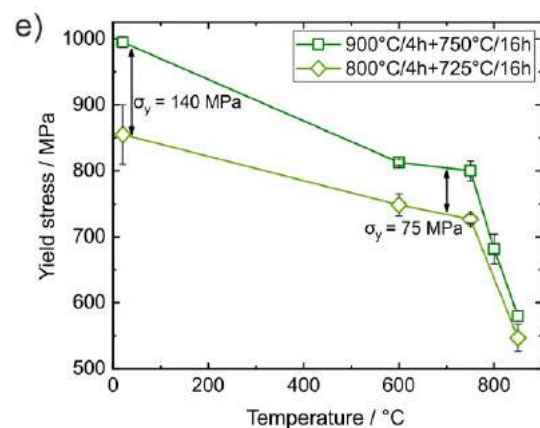
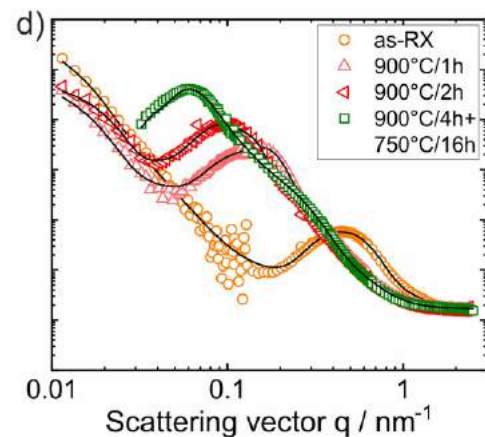
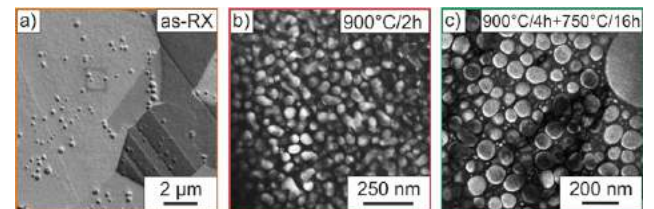


Fig. 1: a) SEM image of the recrystallised (as-RX) condition. Dark field TEM image of the condition after b) step 1 at $900^\circ\text{C} / 2 \text{ h}$ and c) full heat treatment at $900^\circ\text{C} / 4 \text{ h} + 750^\circ\text{C} / 16 \text{ h}$. d) Scattering curves of the conditions: as-RX, $900^\circ\text{C} / 1 \text{ h}$, $900^\circ\text{C} / 2 \text{ h}$ and $900^\circ\text{C} / 4 \text{ h} + 750^\circ\text{C} / 16 \text{ h}$. e) Yield stress under compression as a function of the testing temperature of the two fully heat-treated conditions.

K.K. Deng¹, Q. X. Shi¹, K. B. Nie¹, W. M. Gan², M. Hofmann³

¹College of Mater. Sci. & Eng., Taiyuan University of Technology, Taiyuan, China; ²German Engineering Materials Science Centre (GEMS) at MLZ, Helmholtz-Zentrum hereon GmbH, Garching, Germany; ³Heinz Maier-Leibnitz Zentrum (MLZ), Technical University of Munich, Garching, Germany

Alloying is an effective method to improve the room temperature strength and ductility of lightweight Mg alloys, which can widen their application in the fields of automobiles and electronics. Once the stress exceeds the yield tensile strength (YTS), work hardening strengthening effects occur during the subsequent deformation process. In order to optimise the mechanical properties, an understanding of work hardening and softening and the related mechanisms is essential for industry. In-situ neutron diffraction at the instrument STRESS-SPEC under tensile deformation was performed to clarify the effect of Zn addition to Mg-5Zn on this behaviour of the Mg matrix simultaneously. [1]

Fig. 1 shows the evolution of the peak width (FWHM, represents the dislocation density) of as-extruded pure Mg and Mg-5Zn with increasing load, respectively.

It is noted that the FWHM of all Bragg reflections in Mg-5Zn are larger than those of pure Mg at 0 kN load, indicating a higher defect content of the initial state in Mg-5Zn. In the elastic region, neither the pure Mg nor Mg-5Zn shows any change of the FWHM. However, as the tensile stress exceeds the YTS, the dislocation density increases in both materials. However, the FWHM in Mg-5Zn increases considerably more rapidly than that of pure Mg. This result reveals that the dislocation density in Mg-5Zn before and after tension is significantly higher than that of pure Mg, which indicates a stronger work hardening effect that is most likely due to the existence of MgZn₂ precipitates found in this alloy.

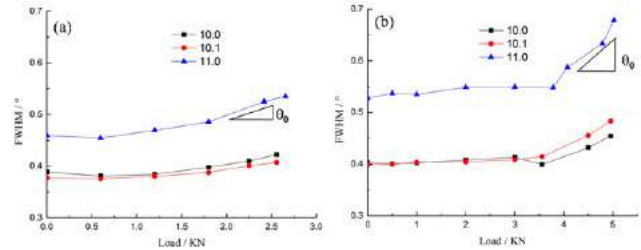


Fig. 1: Evolution of FWHM of (100), (101) and (110) Bragg peaks under tensile load for pure (a) Mg and (b) Mg-5Zn alloy.

Fig. 2 illustrates the in situ tensile stress-strain curves of the two materials. It demonstrates a sharp stress drop when the tensile displacement is kept constant. This phenomenon typically indicates the occurrence of softening. Fig. 2 (c) and (f) shows the stress reductions $\Delta P_{i(i=1, 2, 3)}$ of the two materials, respectively. It is interesting to note that the ΔP_1 and ΔP_2 of Mg-5Zn are lower than those of pure Mg, whereas the ΔP_3 of Mg-5Zn is higher. These results indicate that the addition of Zn can reduce the softening effect in Mg-5Zn at the early stage of tension. However, softening increases significantly at the later tensile stage, which is due to the finer grains in Mg-5Zn leading to a dominated grain boundary sliding.

[1] Q. X. Shi et al., Work hardening and softening behavior of pure Mg influenced by Zn addition investigated via in-situ neutron diffraction, Mater. Sci. Eng., A 772, 138827 (2020)

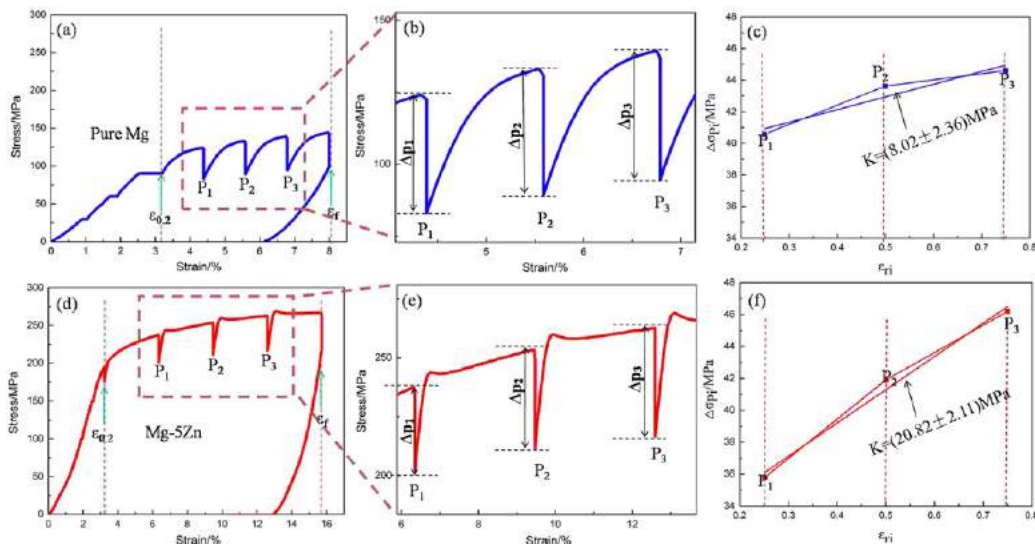


Fig. 2: In situ tensile curves of the as-extruded pure Mg and Mg-5Zn: (a) (d) low magnification, (b) (e) high magnification and (c) (f) variation of ΔP_1 .

Magnetic flux guidance in electrical steel employing stress induced by embossing

T. Neuwirth¹, I. Moll², B. Schauerte³, S. Sebold¹, A. Gustschin⁴, A. Backs¹, S. Vogt³, H. A. Weiss³, N. Leuning³, F. Pfeiffer⁴, K. Hameyer³, W. Volk², P. Böni⁵, M. Schulz¹

¹Heinz Maier-Leibnitz Zentrum (MLZ), Technical University of Munich, Garching, Germany; ²Chair of Metal Forming and Casting, Technical University of Munich, Garching, Germany; ³Institute of Electrical Machines and Chair in Electromagnetic Energy Conversion, RWTH Aachen University, Germany (IEM RWTH); ⁴Chair of Biomedical Physics, Technical University of Munich, Garching, Germany; ⁵Research area Strongly Correlated Electron Systems, Department of Physics Technical University of Munich, Garching, Germany

High energy efficiency is a key component in combatting global warming. In electric drives, especially in reluctance and permanent magnet synchronous machines, this can be achieved by optimising the magnetic flux guidance in their magnetic core. Conventionally, cutouts in the electrical steel sheets comprising the magnetic core are used for magnetic flux guidance. However, this compromises the mechanical strength of the rotating magnetic core and, as a result, reduces the maximum angular velocity.

In the DFG priority program SPP2013 the MLZ, in collaboration with the utg (TUM) and the IEM (RWTH), investigates the use of embossing the electrical steel to guide the magnetic flux. The stress induced by embossing changes the local magnetic properties and decreases the local magnetic permeability. By guiding the magnetic flux by embossing, we intend to increase the mechanical stability of the electrical steel and, consequently, the angular velocity as well as the power density of electric drives.

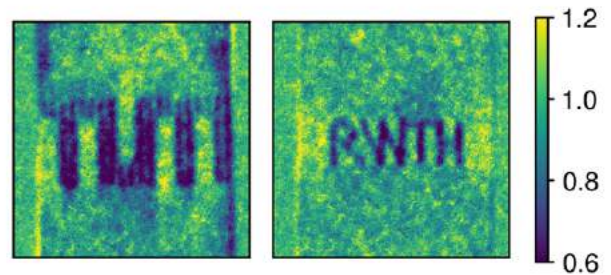


Fig. 2: Examples of finely distributed embossing points acting as magnetic flux barriers.

The neutron grating interferometry (nGI) setup installed at the ANTARES beamline makes it possible to probe the local magnetic properties of the embossed electrical steel. In particular, nGI maps the ultra-small-angle scattering of neutrons off magnetic domain walls.

During the first phase of the project, we used electrical steel sheets with a single large embossing acting as a magnetic flux barrier. Fig. 1 shows the variation in the signal arising from different punch geometries. Our results show that ideally the deformation of the electrical steel sheet is kept localised, which is achieved with a flat punch, as used in sample C. This also provides the highest stability of the flux barrier with respect to the applied magnetic field.

Building on these results, we have recently begun to study flux barriers comprised of finely distributed small embossing points. This change allows one to reduce the deformation of the electrical steel necessary to form a flux barrier. Examples of such embossing patterns are shown in Fig. 2. Using these results, we plan to develop an electric drive using embossing to guide the magnetic flux, resulting in increased angular velocity. The combination of measuring local magnetic (MLZ) and global magnetic properties (IEM) supported by mechanical simulations (utg) leads to a deeper understanding of the influence of embossing induced stress on the local magnetic properties of electrical steel sheets.

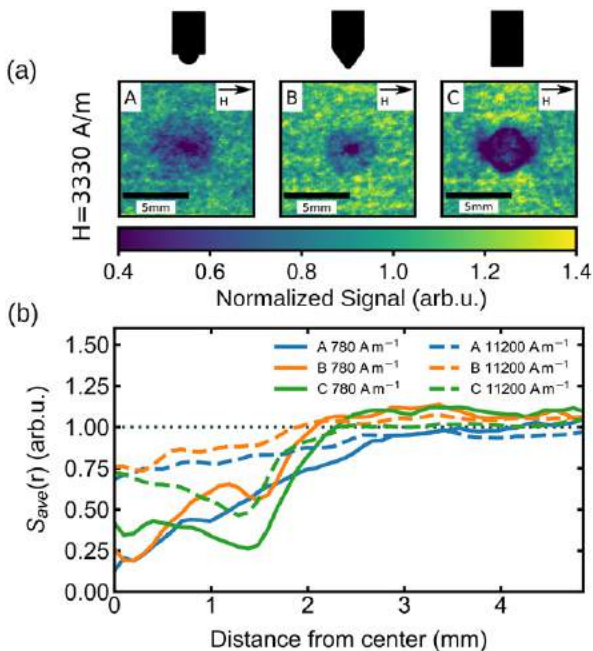


Fig. 1: Analysis of the influence of embossing on the scattering contrast. (a) DFI-signal of samples A, B and C in an applied magnetic field $H = 3330 \text{ A/m}$. The data is normalised using the reference sample also exposed to H . A signal smaller than $S = 1$ indicates more scattering in the embossed sample than in the non-embossed reference. (b) Normalised signal $S_{\text{ave}}(r)$ as obtained by radially averaging the images of samples A (blue), B (orange), and C (green) exposed to two different magnetic fields. Fig. taken from [1].

[1] T. Neuwirth et al., *A high visibility Talbot-Lau neutron grating interferometer to investigate stress-induced magnetic degradation in electrical steel*, *Sci. Rep.* 10, 1764 (2020)

[2] B. Schauerte et al., *The influence of residual stress on flux-barriers of non-oriented electrical steel*, *J. Magn. Magn. Mater.* 504, 166659 (2020)

J. Rebelo Kornmeier¹, M. Hofmann¹, W. M. Gan², V. Robin³, F. Valiorgue⁴, H. Pascal⁴, J. Gibmeier⁵, J. Šaroun⁶

¹Heinz Maier-Leibnitz Zentrum (MLZ), Technical University of Munich, Garching, Germany; ²German Engineering Materials Science Centre (GEMS) at MLZ, Helmholtz-Zentrum hereon GmbH, Garching, Germany; ³Département PRISME – Performance, Risque Industriel, Surveillance pour la Maintenance et l'Exploitation, EDF – R&D, Chatou Cedex, France; ⁴LTDS/ENISE, Saint Étienne, France; ⁵Institute for Applied Materials, Karlsruhe Institute of Technology (KIT), Karlsruhe, Germany; ⁶Nuclear Physics Institute of the CAS, Rez, Czech Republic

Welding typically introduces substantial residual stresses into engineering components due to the highly localised and extreme manner in which heat is applied. The subsequent elevated temperatures and thermal gradients give rise to spatial and temporal variations in thermal expansion and contraction, leading to non-uniform plastic flow of the thermally weakened material.

The determination of residual stress profiles in weldments is an exemplary illustration of the utilisation of neutron diffractometers in engineering applications. Neutron diffraction is eminently suitable in this case, since it advantageously allows one to evaluate the residual stresses from the surface into the bulk of most samples nondestructively.

Fig. 1 on the right shows the tensile stress profiles (open symbols) in an austenitic steel weld AISI316L (ITER) determined using the diffractometer STRESS-SPEC. This particular weld was made as a benchmark sample by tungsten inert gas (TIG) welding in the course of the TG4 project of the European Network on Neutron Techniques Standardisation for Structural Integrity (NeT). Usually, these local tensile

stress states are undesired on engineering components, hindering their high-quality performance in service. Familiar procedures to reduce the tensile residual stresses are post-heat treatments or mechanical surface treatments such as hammering or shot-peening. To consider the impact of post processing methods, the sample was also measured after finish milling (photo sequence on the left). Using new data analysis which additionally deconvolutes the data within the gauge volume, the determination of the stress profile close to the surface (surface detail Fig.), taking into account the milling process effect in the first millimeter depth of the sample, could be assessed and compared to destructive X-ray diffraction measurements and FEM modelling. Predicting the final residual stress fields following different machining processes, as well as the pre material production and post machining processes, is crucial in high safety exigence industrial technological processes such as those required in power plants technology.

[1] J. Rebelo Kornmeier et al., *Effects of finish turning on an austenitic weld investigated using diffraction methods*, *Int. J. Adv. Manuf. Technol.* 108, 635 (2020)

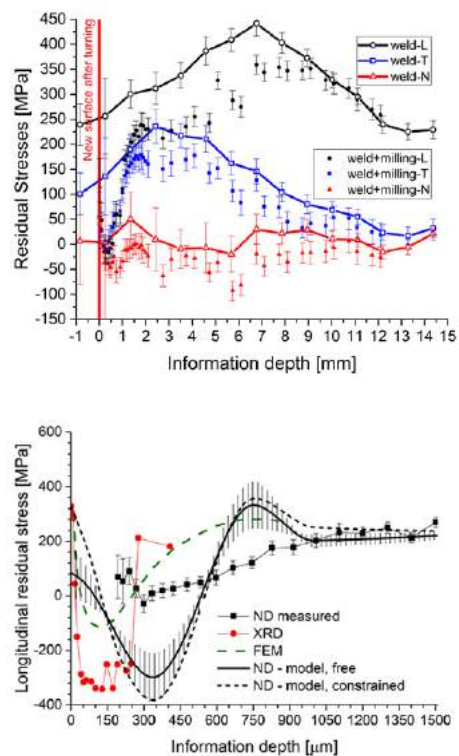


Fig. 1: Left: NeT-TG4, international benchmark weld plate after several passes of finish milling and by last machining state. Right: Residual stress profiles along the plate thickness for the as-welded (open symbols) and as-welded plus finish milling (full symbols) samples. Surface detail where comparison of longitudinal residual stress profiles, of the welded plus finish milling sample, measured by X-ray and neutron diffraction with finite element modelling, neutron spurious strain corrections and data deconvolution within the gauge volume are also pictured.

N. Di Luozzo¹, M. Schulz², M. Fontana¹

¹Laboratorio de Sólidos Amorfos, INTECIN, Facultad de Ingeniería (UBA-CONICET), Buenos Aires, Argentina; ²Heinz Maier-Leibnitz Zentrum, Technical University Munich, Garching, Germany

Transient liquid phase bonding (TLPB) is a diffusion welding technique enabling a weldment with mechanical properties comparable to the base metal. Steel tubes (Fe-0.12C-1.09Mn, wt.%) were welded by TLPB, using Fe-based B-alloyed foils (Fe-5Si-3B, wt.%) as filler material. Neutron radiography (NR) and tomography (NT) were performed on samples cut from the joint of the welded tubes on ANTARES.

The steel/filler material/steel assembly was heated by an induction furnace to 1300°C and held constant for 7 minutes, under a reducing atmosphere (10% H₂ + 90% Ar) and a uniaxial pressure of 5 MPa.

By means of NR and the proposed calibration method [1], a quantitative B concentration profile was measured across the joint in the region where the TLPB process was completed.

The calibration method consists of performing NR at a sample that contains both the steel, and regions where the B content reaches the equilibrium concentration in the steel. This condition was attained by means of a post-weld heat-treatment (PWHT) of samples from the joint, at a temperature for which the B solubility is well-known.

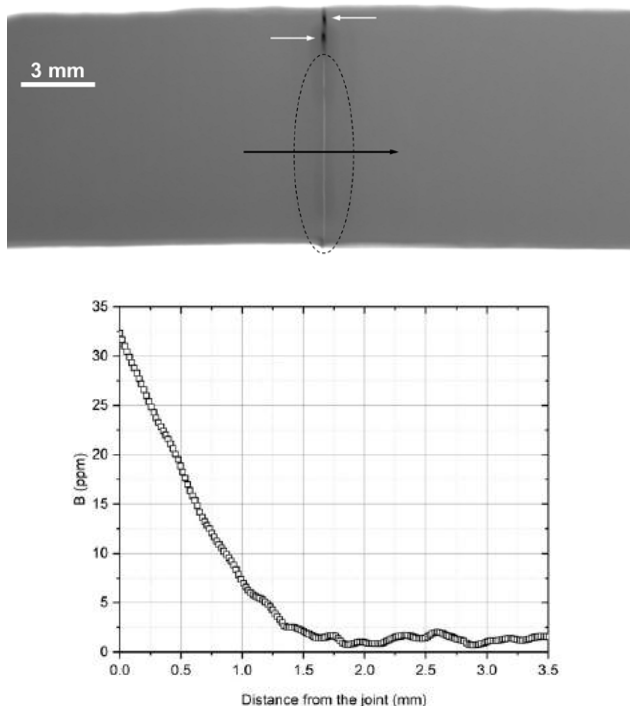


Fig. 1: (a) NR image of the sample in the as-welded condition; (b) Calculated B concentration profile vs. distance from the joint, along the black arrow mark indicated in (a).

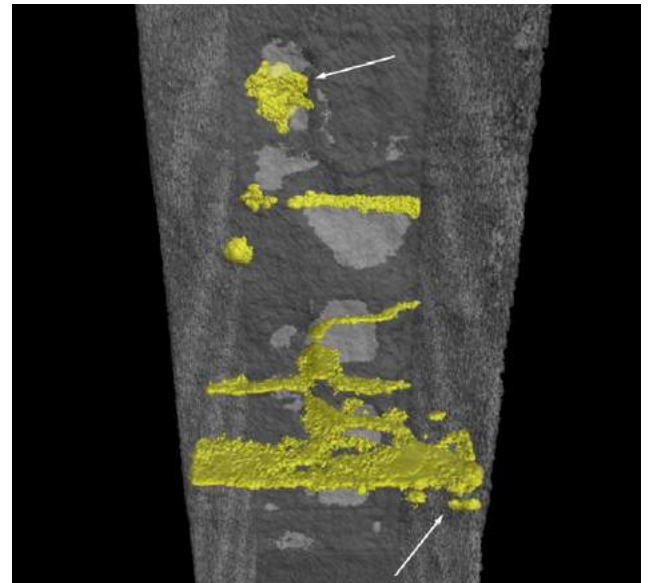


Fig. 2: 3-D reconstruction of the borides (yellow coloured) at the joint in the as-welded sample. In addition, borides outside the joint can be seen (white arrows).

Therefore, in a sample subjected to a PWHT (1 h at 930°C) we can define two calibration points: at the steel, and where a plateau in transmission was observed - corresponding to the B solubility limit at 930°C (11 ppm of B). With the corresponding transmission ratio, it allowed us to calculate the B concentration profile.

Fig. 1a shows an NR image of the sample in the as-welded condition. Considering the large neutron attenuation coefficient of natural B compared to that of Fe, the transmission decreases (Fig. 1a, darker areas) with increasing amounts of B concentration.

Particularly, the joint shows an appreciable difference in contrast depending on the completion of the TLPB process. An incomplete process leads to the presence of borides (Fig. 1a), white arrows), while boride-free regions are obtained when the process is complete (Fig. 1a, dotted line). Moreover, due to the Si from the filler material, the joint shows a higher transmission compared to the steel.

NT allowed a three-dimensional visualisation of the size and shape of borides, highlighting its potential as a non-destructive testing technique of TLPB weldments (Fig. 2).

[1] N. Di Luozzo et al., *Imaging of boron distribution in steel with neutron radiography and tomography*, *J Mater Sci* 18, 7927 (2020)

P. Berdiyeva¹, A. Karabanova², M. G. Makowska³, R. E. Johnsen², D. Blanchard², B. C. Hauback¹, S. Deledda¹¹Department for Neutron Materials Characterization, Institute for Energy Technology, Kjeller, Norway; ²Department of Energy Conversion and Storage, Technical University of Denmark, Lyngby, Denmark; ³Photon Science Division, Paul-Scherrer Institute, Villigen, Switzerland

Strontium chloride octammine $\text{Sr}(\text{NH}_3)_8\text{Cl}_2$ offers high volumetric and gravimetric NH_3 densities and can store and release heat upon exo-/ endothermal absorption and desorption of NH_3 . Thus, it is a promising material for thermochemical heat storage (THS) applications. To study mass transfer and heat distribution effects in a THS prototype reactor (Fig. 1a), we performed in-situ Neutron imaging during NH_3 uptake and release in the $\text{SrCl}_2/\text{Sr}(\text{NH}_3)_8\text{Cl}_2$ system. The THS prototype reactor contained SrCl_2 embedded in a stainless steel honeycomb structure to promote thermal conduction [1]. The high neutron scattering cross-section of hydrogen present in ammonia molecules allowed observation of the NH_3 sorption kinetics and distribution within SrCl_2 . The higher the NH_3 content in the salt, the darker the corresponding area in the image.

The imaging was performed at the NECTAR instrument using thermal neutrons ($L/D \sim 230$). A $\text{ZnS}^{60}\text{LiF}$ scintillator screen converted the neutron beam into light, which was then captured by CCD camera (Andor iKon-L-BV) with a 2048×2048 pixels resolution.

This in-situ neutron radiography study showed that the stainless-steel honeycomb structure is not ideal for transferring the heat from the heating element to the edges of

the honeycomb during the NH_3 desorption processes. The desorption of NH_3 from $\text{Sr}(\text{NH}_3)_8\text{Cl}_2$ occurs from the heat transfer through the powder rather than from the honeycomb, and slower desorption kinetics are observed in the regions farthest away from the heater (Fig. 1b). Along with the images collected perpendicular to the cell, we collected longitudinal images revealing the SrCl_2 volume changes during the ammonia cycling. Furthermore, investigations by neutron tomography showed that the back plate supporting the honeycomb structure was deformed following volume expansion during NH_3 absorption in the powder.

These results demonstrate that neutron imaging techniques are ideal and powerful tools for investigating NH_3 -based thermochemical heat storage prototype systems, and provide critical information on SrCl_2 powder behaviour upon NH_3 absorption and desorption reactions. Additionally, this work opened possibilities for utilising neutron imaging for the study of similar thermal energy storage (TES) materials, with the aim of designing a safe and efficient TES reactor/system.

[1] P. Berdiyeva et al., *In-situ neutron imaging study of NH_3 absorption and desorption in SrCl_2 within a heat storage prototype reactor*, *J. Energy Storage* 29, 101388 (2020)

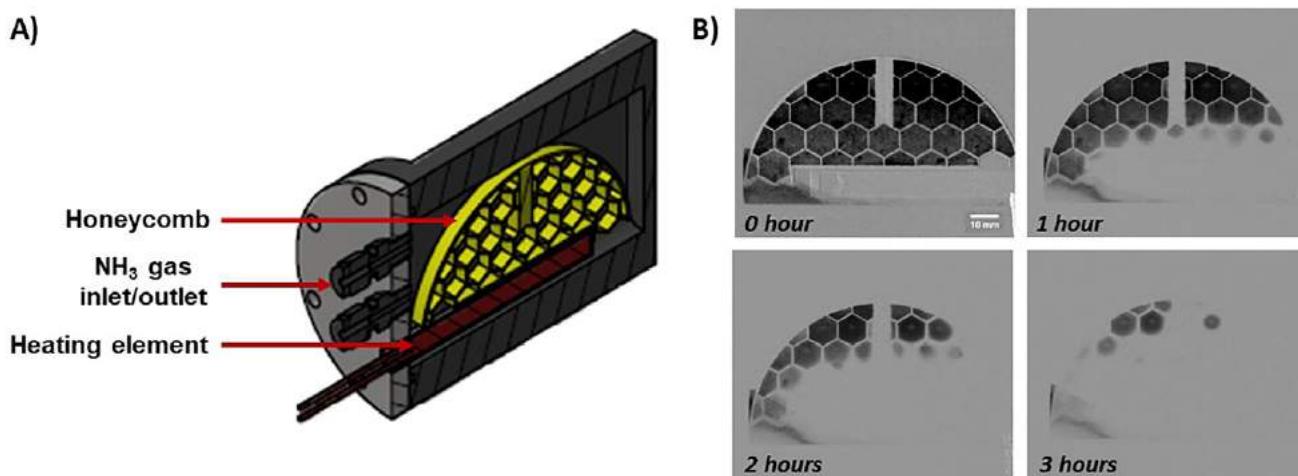


Fig. 1: (A) Schematic representation of the THS reactor prototype and its main components. (B) Normalised neutron radiography images during the NH_3 desorption at 100°C . The figure is adapted from [1].

N. Canha^{1,2}, A. R. Justino¹, C. Galinha¹, J. Lage¹, C. Stieghorst³, Z. Revay³, C. Alves², S. M. Almeida¹

¹Center for Nuclear Sciences and Technologies, Instituto Superior Técnico, Universidade de Lisboa, Bobadela LRS, Portugal; ²CESAM - Centre for Environmental and Marine Studies, Department of Environment and Planning, University of Aveiro, Aveiro, Portugal; ³Heinz Maier-Leibnitz Zentrum, Technical University Munich, Garching, Germany

This study provided a seasonal elemental characterisation of native lichens collected in rural areas of Portugal affected by charcoal kilns, using nuclear analytical techniques available at the PGAA facility of the MLZ, prompt gamma activation analysis (PGAA) and in-beam Neutron Activation Analysis (ibNAA). The electric conductivity of lichens was also assessed. Overall, the main goal was to evaluate the impact of traditional charcoal production on the local air quality by using lichens as biomonitors.

In short, native lichens *Flavoparmelia caperata* (L.) Hale that grow on the bark of olive trees (*Olea europaea* (L.)) were collected over two different seasons (autumn and spring) at the municipality of Ponte de Sor (Portugal), following a sampling grid with 12 sampling sites.

After treatment at the laboratory, amounts of 0.5 - 1 g of the lichen samples collected were sealed in Teflon bags and irradiated in the thermal equivalent neutron flux of $5 \times 10^9 \text{ cm}^{-2}\text{s}^{-1}$ for PGAA and of $3 \times 10^{10} \text{ cm}^{-2}\text{s}^{-1}$ for ibNAA for about 5 hours in both cases. Major and minor components could be detected using PGAA: H, B, C, N, Al, Si, Cl, K, Ca, Ti, Mn, Fe, Cd, Sm and Gd. Minor components and trace elements, such as Na, Mg, Al, Cl, K, Ca, Sc, V, Mn, Zn, Sr, and Br were determined by ibNAA. Overlaps between the two sets of elements were used to control the reliability of the two methods. In most cases, good agreements were found. Fig. 1 provides an overview of the experimental work-flow.



Fig. 1: The charcoal kilns emit the pollutants (1), which the lichens on the olive trees take up (2). Dr. Nuno Canha (r.) has analysed the lichens at the FRM II together with Dr. Christian Stieghorst (3).

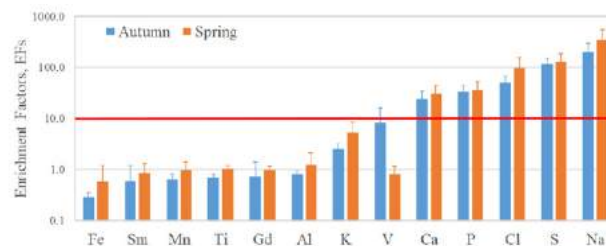


Fig. 2: Enrichment factors for the native lichens in both seasons. The red line represents the threshold of 10, an accepted minimum for enrichment from a non-crustal source.

ability of the two methods. In most cases, good agreements were found. Fig. 1 provides an overview of the experimental work-flow.

In autumn, it was possible to identify high levels of electric conductivity in the vicinity of charcoal kilns due to a higher oxidative stress of the lichens' membrane. Typical chemical elements associated with the emissions of wood burning, such as S and P, also presented the highest contents near the charcoal kilns.

However, the same phenomenon was not found in spring. Residential areas presented the highest levels of S and P, probably due to the impact of biomass burning from home heating that occurred during the winter period.

The enrichment factors (EFs), which are a metric for assessing the extent of anthropogenic pollution with respect to the Earth's crustal composition, were evaluated. If an element has a crustal origin, $EF \approx 1$, while an $EF > 10$ is indication of anthropogenic pollution or natural contributions other than crustal. Fig. 2 provides the enrichment factors for the native lichens in both seasons.

Overall, lichens were found to be enriched with elements that can be attributable to non-crustal sources, namely, sea salt spray (Cl and Na), fertilisers used in agriculture (P and Ca) and wood burning (P and S).

[1] N. Canha et al., *Elemental characterisation of native lichens collected in an area affected by traditional charcoal production*, *J. Radioanal. Nucl. Chem.* 325, 293 (2020)

P. Y. Portnichenko¹, A. Akbari^{2,3,4,5}, S. E. Nikitin^{1,2}, A. S. Cameron¹, P. Čermák^{6,7}, I. Radelytskyi⁶, A. Schneidewind⁶, P. Thalmeier², D. S. Inosov¹

¹Institute of Solid State and Materials Physics, Technische Universität Dresden, Dresden, Germany; ²Max Planck Institute for Chemical Physics of Solids, Dresden, Germany; ³Asia Pacific Center for Theoretical Physics, Pohang, Gyeongbuk, Korea; ⁴Department of Physics, POSTECH, Pohang, Gyeongbuk, Korea; ⁵Max Planck POSTECH Center for Complex Phase Materials, POSTECH, Pohang, Korea; ⁶Jülich Center for Neutron Science at MLZ, Forschungszentrum Jülich GmbH, Garching, Germany; ⁷Faculty of Mathematics and Physics, Department of Condensed Matter Physics, Charles University, Praha, Czech Republic

In contrast to magnetic order formed by the electrons' dipolar moments, more exotic magnetic architectures arising from higher-order multipoles, such as quadrupoles and octupoles, are more difficult to characterise. There is only a limited choice of experimental probes that can distinguish different multipolar moments. In certain cases, even neutron diffraction that is known as the most versatile probe of magnetic structures remains blind to such types of order, which are then referred to as “magnetically hidden”. Much can be learned, however, from the magnetic excitations and their dependence on the applied magnetic field.

In the conventional approach, inelastic neutron scattering (INS) is measured at a constant magnetic field, revealing the dispersion of multipolar excitations in momentum space. The field remains limited to a single high-symmetry direction in the crystal, which is dictated by the chosen scattering plane. In a recent work [1], we tested an alternative approach to the analysis of neutron-scattering data that consists in following the energy of a particular excita-

tion at fixed momentum transfer versus the magnitude and angle of the applied magnetic field. A magnetic field as a three-dimensional vector opens up a parameter space as rich in information as the momentum space. Therefore, the rotating-field technique at fixed momentum should complement conventional INS measurements of the dispersion at a constant field and holds great promise, especially for identifying the symmetry of multipolar order parameters and the details of intermultipolar interactions that stabilise hidden-order phases.

To demonstrate the power of this method, our group from TU Dresden and collaborators investigated the heavy-fermion compound CeB_6 , a well-studied material known to host long-range order of magnetic multipoles. Using combined data from the cold-neutron spectrometer PANDA at the MLZ and several other INS instruments worldwide, we found that not only the energy and intensity but even the number of multipolar excitations visible to neutron scattering depends on the direction of the magnetic field. To explain these effects, we compared the results with an effective theory of multipolar excitations based on a multipolar interaction model. Fig. 1 compares the experimental and calculated energies of low-lying excitations in CeB_6 as a function of the magnetic field direction in polar coordinates, demonstrating good agreement between theory and experiment.

Our approach opens up a new way of looking at correlated-electron systems with multipolar order parameters that should be applicable to a wide range of compounds. Just as we use ordinary measurements of spin-wave dispersions to fit exchange interactions between neighbour spins, measurements in field-angular space would allow us to extract additional parameters of the magnetic Hamiltonian including magnetocrystalline anisotropy, crystal electric field splitting, and interactions between different multipoles.

[1] P. Y. Portnichenko et al., *Field-Angle-Resolved Magnetic Excitations as a Probe of Hidden-Order Symmetry in CeB_6* , *Phys. Rev. X* 10, 021010 (2020)

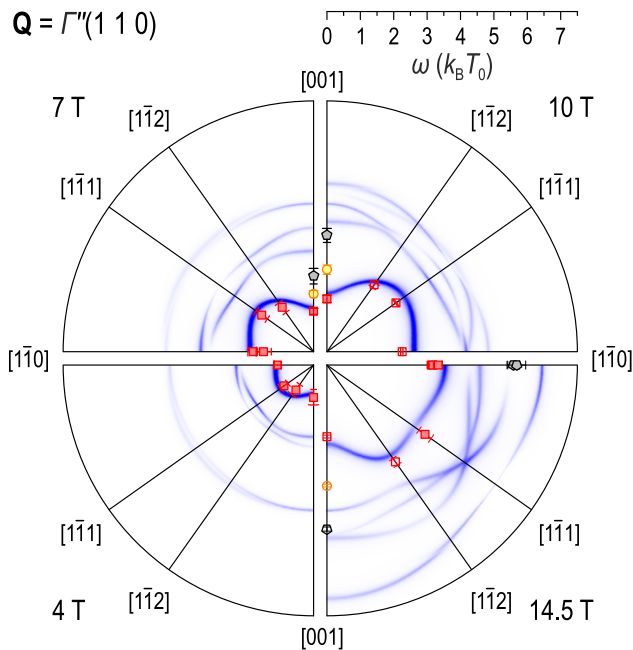


Fig. 1: Multipolar excitations in CeB_6 at the Brillouin zone center from the experiment (points) and from model calculations (blue lines). The radial coordinate corresponds to the excitation energy, and the angular coordinate to the magnetic field direction. The four segments of the Fig. show results for the magnetic field of 4, 7, 10, and 14.5 T.

A. Maity^{1,2}, R. Dutta^{3,4}, W. Paulus⁵

¹Institute of Physical Chemistry, Georg-August-Universität Göttingen, Göttingen, Germany; ²Heinz Maier-Leibnitz Zentrum (MLZ), Technical University Munich, Garching, Germany; ³Institute of Crystallography, RWTH Aachen University, Aachen, Germany; ⁴Jülich Centre for Neutron Science (JCNS) at MLZ, Forschungszentrum Jülich GmbH, Garching, Germany; ⁵Institute Charles Gerhardt Montpellier, University of Montpellier, Montpellier, France

Magnetic excitations in the spin-stripe phases of La-based 214 -nickelates have been vigorously explored using inelastic neutron scattering study for almost three decades and have still remained an exciting research field, especially when it comes to understanding their differences from, as well as their structural similarities to, high- T_c 214 -cuprates. In view of their two-dimensional antiferromagnetic nature reported so far, *out-of-plane* interaction is not generally expected in 214 -nickelates.

Recently, we performed inelastic neutron scattering (INS) measurement on a stripe discommensurated Sr-doped $\text{Pr}_{3/2}\text{Sr}_{1/2}\text{NiO}_4$ using the thermal triple axis spectrometer PUMA at the MLZ. Our results on the magnetic excitations of $\text{Pr}_{3/2}\text{Sr}_{1/2}\text{NiO}_4$, with stripe incommensurability $\epsilon = 0.4$, show very compelling evidence for the presence of a sizable *out-of-plane* interaction ($J_{\perp} \sim 2.2$ meV) [1], so far never reported in other hole-doped 214 -nickelates.

In the magnetic excitations measured, we observed a symmetrical shift of the spin wave dispersion from the antiferromagnetic (AFM) zone center in the energy transfer range of 35 to 45 meV (Fig. 1a). Owing to the large neutron flux, good instrumental resolution and low background of PUMA, the symmetrical outward shift has been unambiguously identified.

From the linear spin wave (LSW) theory based calculation using a three-dimensional model of discommensurated spin stripe (DCSS) unit combining a checker board (CB) unit and a $1/3$ -stripe unit for $\epsilon = 0.4$ (Fig. 1b), we were able to explicitly show that such an outward shift of the spin wave dispersion results from the overlap of a separate mode (type-III) (Fig. 1c), originating exclusively from the out-of-plane interaction. This rather suggests the presence of a three-dimensional nature of the magnetic excitations near the half-doped region of $\text{Pr}_{3/2}\text{Sr}_{1/2}\text{NiO}_4$, in contrast to the two-dimensional nature of the magnetic excitations reported in other hole-doped 214 -nickelates. Our spin wave simulation, taking into account *out-of-plane* in addition to the in-plane exchange interactions, shows very good agreement with the magnetic excitations measured.

Our study suggests that careful consideration of the out-of-plane coupling is necessary in the 3D-DCSS model to uncover many interesting features of magnetic excitations in the stripe discommensurated phases of strongly correlated 214 -nickelates.

[1] A. Maity et al., *Stripe Discommensuration and Spin Dynamics of Half-Doped $\text{Pr}_{3/2}\text{Sr}_{1/2}\text{NiO}_4$* , *Phys. Rev. Lett.* **124**, 147202 (2020)

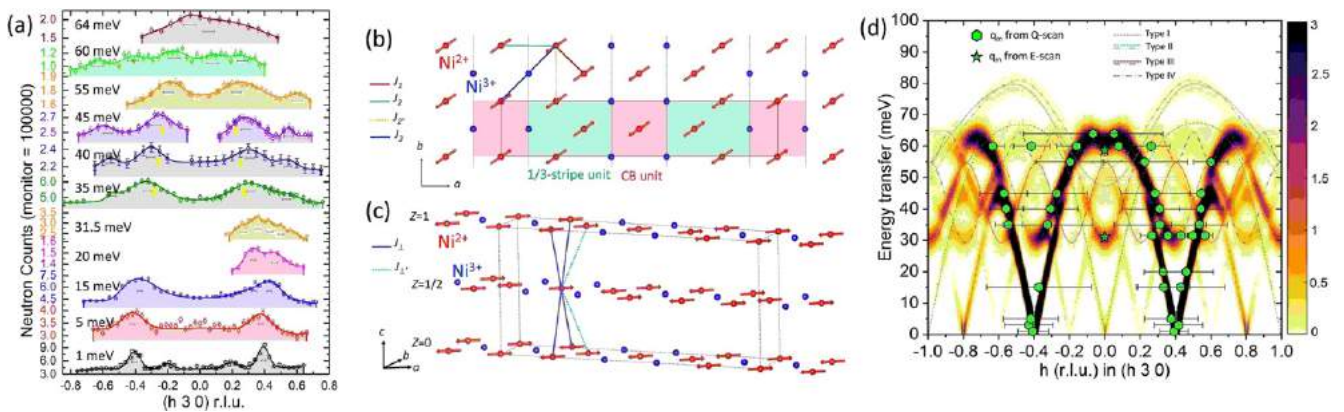


Fig. 1: (a) Constant-E scans through Q_{AFM} along h in the energy range from 1 to 64 meV. (b) Schematic representation of the site-centered DCSS unit in NiO_2 plane. Exchange interactions between Ni^{2+} spins are indicated with different colors. (c) 3D representation of the DCSS unit cell with the 1st nearest out-of-plane AFM interaction J_{\perp} and negligible FM interaction J_{\parallel} . (d) Intensity convoluted spin wave dispersion in the $(hk0)$ -plane from LSW over plotted with the measured wave vectors as indicated by green filled symbols. Dashed lines in different colors represent different type of modes.

R. Dutta^{1,2}, A. Maity^{3,4}, A. Marsicano⁵, J. R. Stewart⁶, M. Opel⁷, W. Paulus⁵

¹Institute of Crystallography, RWTH Aachen University, Aachen, Germany; ²Jülich Centre for Neutron Science (JCNS) at MLZ, Forschungszentrum Jülich GmbH, Garching, Germany; ³Institute of Physical Chemistry, Georg-August-Universität Göttingen, Göttingen, Germany; ⁴Heinz Maier-Leibnitz Zentrum (MLZ), Technical University of Munich, Garching, Germany; ⁵Institute Charles Gerhardt Montpellier, University of Montpellier, Montpellier, France; ⁶ISIS Neutron and Muon Source, Rutherford Appleton Laboratory, Didcot, United Kingdom; ⁷Walther-Meißner-Institute, Bavarian Academy of Sciences and Humanities, Garching, Germany

Strong electronic correlations in exotic Heisenberg antiferromagnets (AFM) ranging from one- to three-dimensional are of the utmost interest in general condensed matter physics. Long-range 3D-AFM ordering has been observed in both stoichiometric 214-type nickelates and cuprates. Hole doping in the normal state of high-Tc La-based cuprates partially suppresses 3D-AFM ordering, whereas studies on La-based nickelates suggest hole doping leads to a strong two-dimensional (2D) charge and spin ordering in the stripe to checkerboard fashion. Most studies have predominantly suggested hole-doped 214-type nickelates to be quasi- or purely 2D-AFM, neglecting the possible out-of-plane interactions between the interlayer stripes, and accordingly the related effects on the in-plane excitations have not been discussed. In our previous study on a half-doped $\text{Pr}_{2-x}\text{Sr}_x\text{NiO}_4$ a sizable out-of-plane interaction (J_{\perp}) was predicted by linear spin wave theory (LSWT) [1]. However, it is very important to understand whether the presence of such out-of-plane interaction is common for any underlying spin microstructure, especially in $\text{Pr}_{2-x}\text{Sr}_x\text{NiO}_4$ systems.

Here, we present a spin wave study of a $\text{Pr}_{1.5}\text{Sr}_{0.5}\text{NiO}_4$ single crystal with magnetic incommensurability $\epsilon = 0.461$ at 10 K, using inelastic neutron scattering performed at the thermal triple-axis spectrometer PUMA, MLZ and time-of-flight spectrometer MAPS, ISIS. Our results provide a detailed

picture of the $[Q_x, Q_y, Q_z]$ dependence of the spin excitations in $\text{Pr}_{1.5}\text{Sr}_{0.5}\text{NiO}_4$ over several Brillouin Zones, demonstrating its anisotropic three-dimensional nature shown in Fig. 1.

The magnetic spectrum is adequately described in an unconventional model of two-layer stacking of discommensurated spin stripe (DCSS) NiO_2 planes along the c -axis. The value of the out-of-plane interaction $J_{\perp} \approx 1.9$ meV obtained is consistent with the relation to its in-plane spin correlation length. Nevertheless, the maximum magnon band-width and the spin wave velocities along the in-plane and out-of-plane acoustic modes indicate the three-dimensional nature of spin dynamics [2].

Our results signify that the presence of L-dependent spin dispersion is more likely to be common at least in Pr-based 214-nickelates near half-doping, while the in-plane exchange interactions and the presence of single-ion anisotropy are highly dependent on the underlying spin microstructure.

[1] A. Maity et al., *Stripe Discommensuration and Spin Dynamics of Half-Doped $\text{Pr}_{3/2}\text{Sr}_{1/2}\text{NiO}_4$* , *Phys. Rev. Lett.* **124**, 147202 (2020)

[2] R. Dutta et al., *Direct evidence for anisotropic three-dimensional magnetic excitations in a hole-doped antiferromagnet*, *Phys. Rev. B* **102**, 165130 (2020)

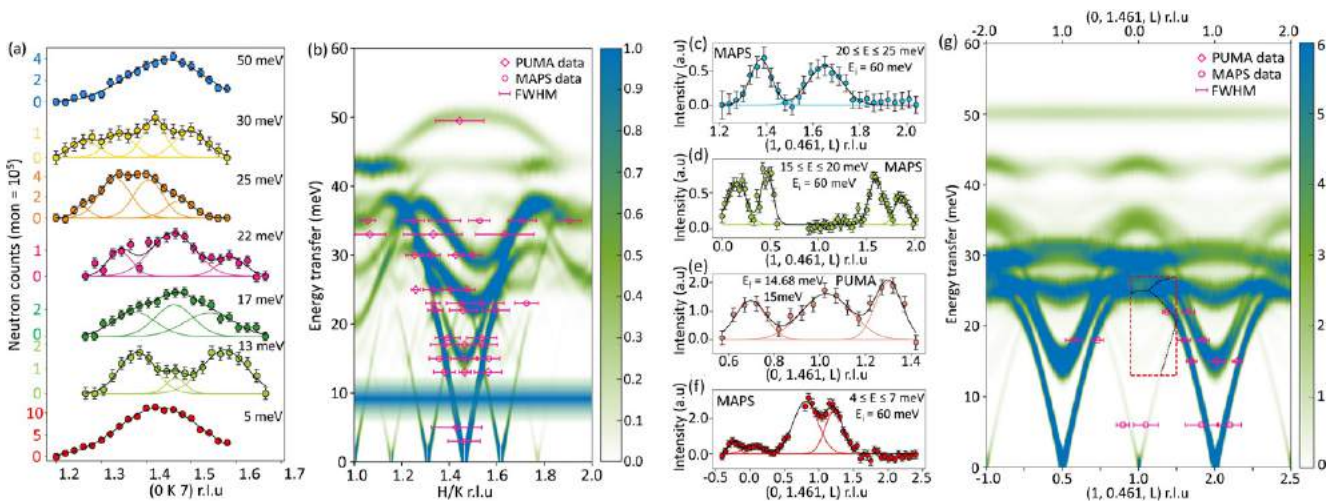


Fig. 1: (a) In-plane magnetic excitations measured at PUMA. (c-f) Out-of-plane magnetic excitations measured at both PUMA and MAPS. (b) and (g) display the corresponding calculated in- and out-of-plane spin dispersion overlapped with experimental dispersion points.

2D ferromagnetic behaviours in a van der Waals honeycomb lattice

Z. Fu¹, Y.-Q. Zhai², Y.-F. Deng², Y.-Z. Zheng², E. Feng³, Y. Su³

¹Neutron Scattering Platform, Songshan Lake Materials Laboratory, Dongguan, China; ²Frontier Institute of Science and Technology (FIST), State Key Laboratory for Mechanical Behavior of Materials, School of Science, Xi'an Jiaotong University, Xi'an, China; ³Jülich Centre for Neutron Science (JCNS) at MLZ, Forschungszentrum Jülich GmbH, Garching, Germany

Two-dimensional (2D) ferromagnetic (FM) materials have been intensively studied for the purpose of next-generation spintronic device fabrication, owing to their atomic thickness and controllable electron-spin degree of freedom. However, the discovery of 2D FM materials in experiment is quite challenging. Only a very limited number of 2D ferromagnets have been successfully fabricated so far. Herein, a spin integer ($S = 2$) dimerised honeycomb lattice in an Fe^{2+} -azido layered compound $[\text{Fe}(4\text{-etpy})_2(\text{N}_3)_2]_n$ (4-etpy = 4-ethylpyridine), denoted as FEN, is reported (Fig. 1a-c). Microscopy characterisations show that the thickness of thin-film FEN can be reduced to only 13 nm, which is about ten layers of FEN. The bulk magnetic property suggests FM contributions emerged at 28 and 39 K. AC susceptibility reveals a spin glass phase at around 22.2 K, due to intra-layer competing FM and antiferromagnetic exchange interactions.

To understand the complicated magnetism of FEN, we carried out a polarised neutron scattering investigation on the cold neutron time-of-flight spectrometer DNS. The flipping ratios were measured for the strongest (100) Bragg reflection from 8 to 49 K (Fig. 1d). We observed two drops in the flipping ratio at around 28 and 39 K, in agreement with the bulk magnetic property. The gradual change of the flipping ratios from 28 to 39 K suggests an in-plane spin reorientation. In order to find out whether long-range FM phase transitions occur in FEN, the total neutron scattering intensi-

ties collected at 3.3, 43 and 100 K are compared in Fig. 1d. The scattering profiles and intensities are nearly identical. To further verify this point, the temperature dependence of the peak intensity of the (100) Bragg reflection was measured from 10 to 48 K. There is no sharp change when the temperature crosses 28 and 39 K. The slow decrease in peak intensity with increasing temperature is due to the increasing thermal vibrational amplitude of the atoms. The magnetic scattering intensity obtained from xyz-polarisation analysis could be explained by the spin correlation of a Fe^{2+} spin pair with free in-plane rotation, indicating a strong intra-dimer coupling and a 2D feature of the magnetic layers. Therefore, we have found no evidence for long-range magnetic order in FEN. The FM contributions occurring at 28 and 39 K are more likely to be due to collective in-plane canting and reorientation of Fe^{2+} spin pairs.

In conclusion, our neutron scattering investigation shows that the magnetic layers of FEN are well isolated and therefore FEN is a promising candidate for 2D van der Waals ferromagnets. [1] In addition to optimising the geometry by chemical means, future work will endeavor to reduce the number of material layers.

[1] Y.-Q. Zhai et al., *Reentrant Spin Glass and Large Coercive Field Observed in a Spin Integer Dimerized Honeycomb Lattice*, *Adv. Funct. Mater.* 31(1), 2004744 (2021)

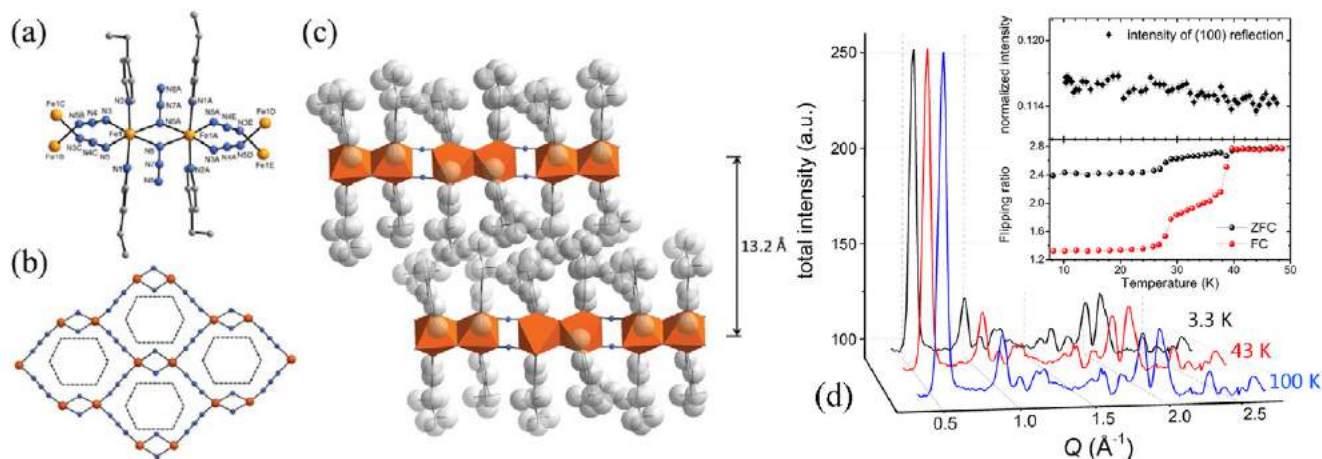


Fig. 1: (a) The asymmetric unit; (b) The 2D dimerised honeycomb structure; (c) interlayer-packing view; (d) neutron scattering patterns collected at 3.3, 43, 100 K and the intensity of the strongest (100) reflection vs. temperature.

D. Hu^{1,3}, R. Georgii², B. Pedersen², P. Dai³
¹Department of Physics, Hangzhou Normal University, Hangzhou, Zhejiang, China; ²Heinz Maier-Leibnitz Zentrum, Technical University of Munich, Garching, Germany; ³Department of Physics and Astronomy, Rice University, Houston, Texas, USA

High-temperature superconductivity in iron-based superconductors can be induced by element substitution or hydrostatic pressures that act to suppress long-range antiferromagnetic order and the associated tetragonal to orthorhombic lattice distortion (T_s/T_N). To understand the microscopic origin of superconductivity, it is important to sort out the interplay amongst magnetism, lattice distortion and superconductivity. Compared with element substitution, pressure can tune the electronic phases of the system without inducing additional lattice distortion.

The optimal superconductivity ($T_c \approx 30$ K) in $\text{BaFe}_2(\text{As}_{1-x}\text{P}_x)_2$ can be reached when the coupled T_N and T_s are suppressed to zero temperature with an increase of the P concentration to $x = 0.30$, which is located at the center of the V-shaped

non-Fermi-liquid zone connecting to the putative quantum critical point (QCP) in the system. In the underdoped $\text{BaFe}_2(\text{As}_{0.72}\text{P}_{0.28})_2$ with $T_N = T_s \approx 40$ K, we found that the kink in the resistance-temperature (RT) measurement has a nonmonotonic dependence on the c-axis uniaxial pressure, before vanishing at pressure above 280 MPa. In previous experiments under ambient condition, the kinks in RT correspond to T_N/T_s in iron pnictides. Due to the nonmonotonic dependence and applied uniaxial pressure, it is necessary to carry out neutron scattering experiment to establish that it is from the AF phase transition.

Benefiting from the in-situ uniaxial pressure sample environment on MIRA, we can control the pressures added onto the sample systematically and compare the results obtained with transport measurements. As shown in Fig.1, with increasing c-axis pressure, T_N and T_s are slightly enhanced around $P_c \sim 33$ MPa firstly. Using the in situ pressure cell, we can compare the scattering intensity directly. Although it is hard to determine the T_N precisely at 66 and 100 MPa, we can clearly see the reduction in the magnetic scattering intensities below ≈ 28 K is due to the appearance of superconductivity. This neutron result is consistent with the evolution of RT curves found in the transport measurements under a c-axis uniaxial pressure.

Our results reveal the importance of the magnetoelastic coupling in $\text{BaFe}_2(\text{As}_{1-x}\text{P}_x)_2$, suggesting that the c-axis pressure can be used as a tuning parameter to manipulate the electronic phases in iron pnictides.

[1] Ding Hu et al., *Uniaxial c-axis pressure effects on the underdoped superconductor $\text{BaFe}_2(\text{As}_{0.72}\text{P}_{0.28})_2$* , *Phys. Rev. B* 101, 020507(R) (2020).

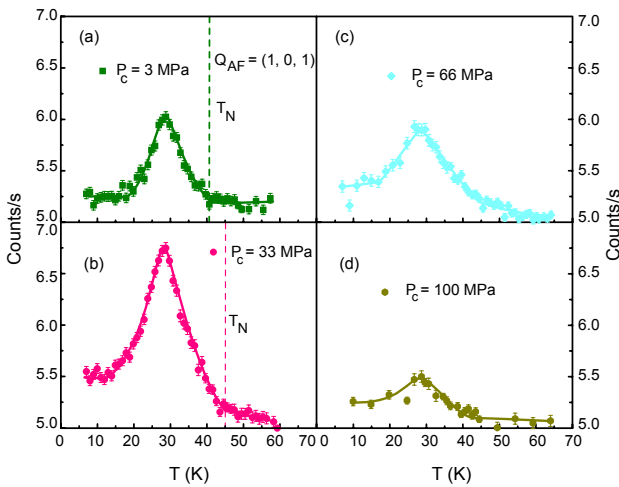


Fig. 1: Temperature dependence of the magnetic scattering intensity measured on MIRA-II for $\text{BaFe}_2(\text{As}_{0.72}\text{P}_{0.28})_2$ with a c-axis pressure of (a) $P_c = 3$ MPa, (b) 33 MPa, (c) 66 MPa, and (d) 100 MPa at $\mathbf{Q}_{\text{AF}} = (1, 0, 1)$. The solid lines are guides to the eye. Four figures are plotted in the same vertical scale so that the pressure-induced magnetic scattering intensity change can be directly compared. Dashed lines in (a) and (b) mark the AF transition temperature T_N .

Z. Fu¹, L. Qin², Y.-Z. Zheng², W. Lohstroh³

¹Neutron Scattering Platform, Songshan Lake Materials Laboratory, Dongguan, China; ²Frontier Institute of Science and Technology (FIST), State Key Laboratory for Mechanical Behavior of Materials, School of Science, Xi'an Jiaotong University, Xi'an, China; ³Heinz Maier-Leibnitz Zentrum (MLZ), Technical University of Munich, Garching

Cyclic magnetic molecules possess remarkable spin dynamic properties at the crossover between classical and quantum regimes, holding much potential for magnetic storage, spintronics, and quantum information processing. As some of the best characterised cyclic magnetic molecules so far, chromium molecular rings have shown remarkable quantum properties such as quantum oscillations and quantum coherence. However, ferromagnetic (FM) chromium rings are really uncommon. The heterometallic molecular ring $\{\text{Cr}_8\text{Y}_8\}$ represents a rare example of weak FM rings, as revealed by magnetic property experiments. As Y^{3+} ions are diamagnetic and intermolecular magnetic interactions are negligible, FM interactions should exist among the eight Cr^{3+} moments ($s = 3/2$) within single molecules. It is vital to

study microscopically how Cr^{3+} moments interact with each other in $\{\text{Cr}_8\text{Y}_8\}$. This knowledge will be helpful in understanding the more complicated magnetism of isostructural cases of $\{\text{Cr}_8\text{Ln}_8\}$, where Ln stands for magnetic rare earth elements. In this respect, inelastic neutron scattering (INS) is a powerful tool for studying the spin dynamics and determining the parameters of exchange interactions.

In the heat capacity (HC) data of $\{\text{Cr}_8\text{Ln}_8\}$, we observed two Schottky anomalies originating from the thermal population of low-lying discrete spin levels. The fit to HC data collected at 0 T yielded two energy gaps of 0.009 and 0.130 meV. In order to unambiguously measure the low-lying magnetic energy spectrum, we performed an INS experiment on the TOFTOF spectrometer with an incident neutron wavelength of 10 Å. Distinct INS intensities were observed on both the neutron-energy gain and loss sides. Fig. 1 shows the integrated scattering intensities of the neutron-energy loss spectra collected at 0.5 and 20 K. A strong INS peak is clearly observed at 0.133(13) meV, in good agreement with the energy gap obtained from HC data. The intensity of this peak decreased when the temperature increased from 0.5 to 20 K, indicating that it is a cold transition from the $S = 12$ ground state to the $S = 11$ excited state. We propose a single- J model as an approach to the spin dynamics of $\{\text{Cr}_8\text{Y}_8\}$. In this model, we consider only the nearest-neighbour interaction with a single FM exchange constant J . The calculation shows that the first excited state lies $0.879|J|$ above the ground state. Therefore, J is determined to be 0.151(15) meV. The small energy gap of 0.009 meV obtained in HC data is tentatively attributed to the zero field splitting of the ground state, but this cannot be verified due to the limited resolution of TOFTOF.

In conclusion, we have investigated the low-lying spin levels of $\{\text{Cr}_8\text{Y}_8\}$ by means of HC and INS methods. The exchange constant has been determined for the single- J model, which is a good approach to the low-temperature spin dynamics of $\{\text{Cr}_8\text{Y}_8\}$. [1]

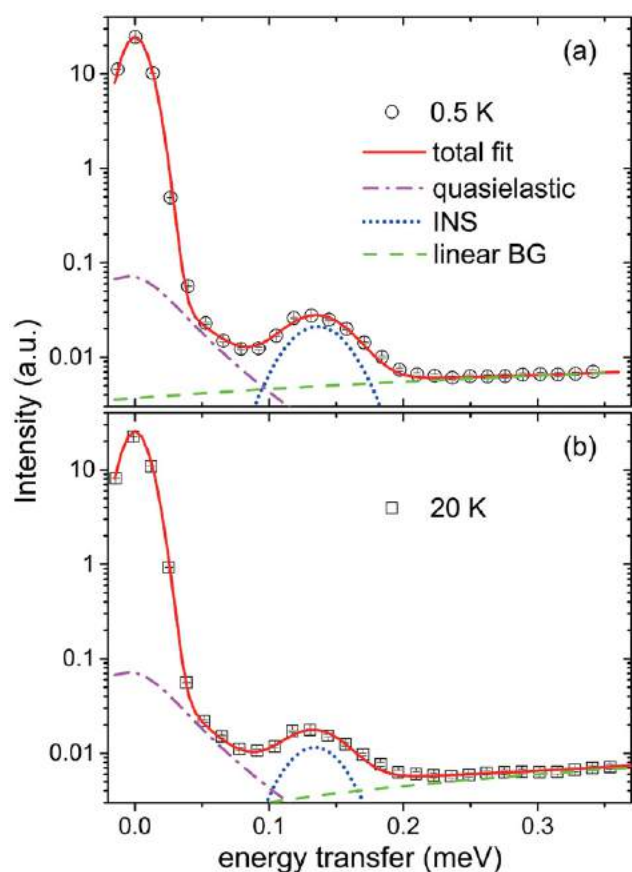


Fig. 1: Zero-field INS spectra collected on TOFTOF at 0.5 (a) and 20 K (b), with inclusion of least-squares fits as red solid lines. A linear background (green dashed line) is assumed. The INS transition (blue dotted line) is described by a Gaussian function. The quasielastic term (purple dash-dot line) consists of a minor Gaussian function representing the INS contribution of zero-field splitting, and a Lorentzian function due to the static disorder. The error bars represent the standard deviation of the intensity.

[1] Z. Fu et al., *Low-temperature spin dynamics of ferromagnetic molecular ring $\{\text{Cr}_8\text{Y}_8\}$* , *npj Quantum Mater.* 5, 32 (2020)

J. Kindervater¹, T. Adams¹, A. Bauer¹, F. X. Haslbeck¹, A. Chacon¹, S. Mühlbauer², F. Jonietz¹, A. Neubauer¹, U. Gasser³, G. Nagy³, N. Martin^{1,2}, W. Häußler^{1,2}, R. Georgii^{1,2}, M. Garst^{4,5}, C. Pfleiderer¹

¹Physics Department, Technical University of Munich, Garching, Germany; ²Heinz Maier-Leibnitz Zentrum (MLZ), Technical University of Munich, Garching, Germany; ³Laboratory for Neutron Scattering and Imaging, Paul Scherrer Institut, Villigen, Switzerland; ⁴Institute of Theoretical Physics, Technische Universität Dresden, Dresden, Germany; ⁵Institut of Theoretical Solid State Physics, Karlsruhe Institute of Technology, Karlsruhe, Germany

Cubic chiral magnets stabilise incommensurate modulated magnetic structures, exhibit weak itinerant-electron magnetism and have allowed the study of quantum phase transitions under high pressure. Recently, their potential for spintronic applications has been driven by the discovery of topological spin textures, the so-called magnetic skyrmion. To this day, the role that magnetocrystalline anisotropies (MCA) play in these phenomena remains a topic of interest and a possible avenue to manipulate the different compounds' behaviour.

At zero magnetic field, the ground state consists of a helical magnetic order propagating along the preferred directions of the system as determined by the MCA. We have characterised the spontaneous magnetic correlation in $Mn_{1-x}Fe_xSi$ ($x = 0.0-0.1$) via small angle neutron scattering experiments carried out on the beamlines RESEDA and MIRA at the MLZ and at the beamline SANS-II at the PSI [1].

The precise distribution of magnetic scattering was obtained by recording data at 40 different orientations of the incoming neutron beam, covering a sample rotation of 180°. The experimental results show a change of the preferred axis of propagation from the $\langle 111 \rangle$ directions, for $x = 0$

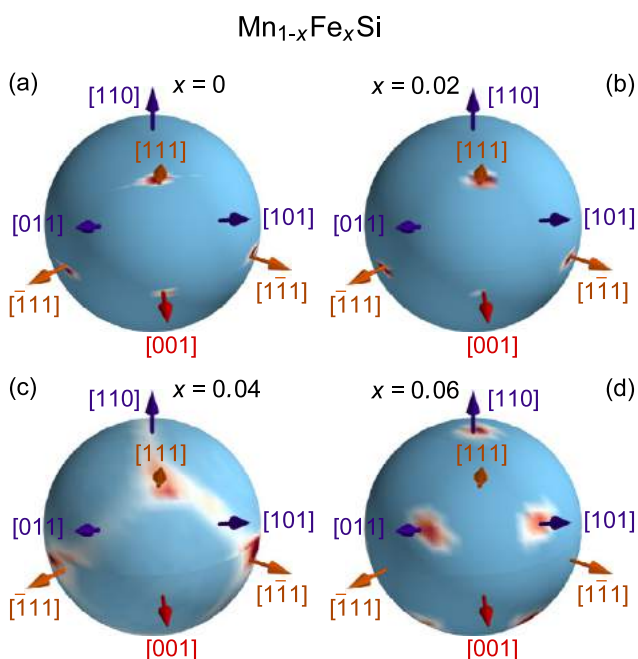


Fig. 1: Depiction of the experimentally observed neutron scattering intensity in zero magnetic field on spheres in reciprocal space.

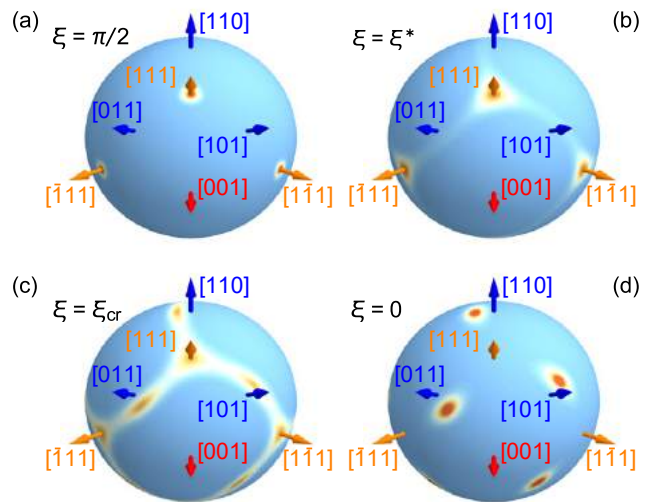


Fig. 2: Scattering pattern associated to the calculated potential landscape.

to $\langle 110 \rangle$, for $x = 0.06$ (Fig. 1). This evolution is surprising, since the lowest order magnetocrystalline contributions allow for $\langle 111 \rangle$ and $\langle 100 \rangle$ easy-axes only. Additionally, increasing doping results in a shorter propagation length and the observed maxima become broader due to the added disorder.

A theoretical analysis of the orientation of helical magnetic order by means of an effective MCA potential identifies a change in character in the anisotropic terms from 4th order in spin orbit coupling to 6th order as a simple explanation for the observed behaviour. The latter term allows for easy-axes close to a $\langle 110 \rangle$ direction and the experimental results can be reproduced in excellent qualitative agreement by tuning the contribution from both terms in the minimal magnetocrystalline anisotropy potential (Fig. 2).

The change in the MCA contribution provides a simple explanation for the observation of broad intensity maxima for the $\langle 110 \rangle$ directions in the partial ordered state of MnSi under pressure. Furthermore, it provides an alternative solution to observed discrepancies to the Brazovskii scenario, which has been very successful in describing pure MnSi.

[1] Kindervater et al., Evolution of magnetocrystalline anisotropies in $Mn_{1-x}Fe_xSi$ and $Mn_{1-x}Co_xSi$ as inferred from small-angle neutron scattering and bulk properties. *Phys. Rev. B* 101, 104406 (2020)

A. S. Sukhanov^{1,2}, B. E. Zuniga Cespedes^{1,3}, P. Vir¹, A. S. Cameron², A. Heinemann⁴, N. Martin⁵, G. Chaboussant⁵, V. Kumar⁶, P. Milde³, L. M. Eng^{3,7}, C. Felser^{1,7}, D. S. Inosov^{2,7}

¹Max Planck Institute for Chemical Physics of Solids, Dresden, Germany; ²Institute for Solid State and Materials Physics, Technische Universität Dresden, Dresden, Germany; ³Institute of Applied Physics, Technische Universität Dresden, Dresden, Germany; ⁴German Engineering Materials Science Centre (GEMS) at MLZ, Helmholtz-Zentrum hereon GmbH, Garching, Germany; ⁵Université Paris-Saclay, CEA, CNRS, Laboratoire Léon Brillouin, CEA Saclay, Gif-sur-Yvette, France; ⁶Physics Department, Technical University of Munich, Garching, Germany; ⁷Dresden-Würzburg Cluster of Excellence on Complexity and Topology in Quantum Matter (ct.qmat), Technische Universität Dresden, Dresden, Germany

The mutual noncoplanar orientation of the neighbouring spins in the magnetic structures twisted by the Dzyaloshinskii-Moriya interaction can be described by the topological charge that differentiates two types of the topologically-protected magnetic structures – skyrmions and antiskyrmions. Whilst an increasing number of skyrmion-hosting compounds have been discovered, antiskyrmions have so far only been observed in thin plates of Mn_{1.4}PtSn, which belongs to the D_{2d} symmetry class. In agreement with the symmetry-based theoretical predictions, the Lorentz transmission microscopy (LTEM) measurements of Mn_{1.4}PtSn demonstrated the presence of antiskyrmions in a magnetic field applied perpendicular to the (001) surface of a thin lamella sample.

Since previous studies conducted with thin lamellae of Mn_{1.4}PtSn indicated that the sample geometry can influence the magnetic texture of the material, characterisation of the magnetic structure of Mn_{1.4}PtSn in bulk single crystals is required. To this end, SANS serves as the ideal technique due to the very high penetration depth of the neutron radiation. In addition to the reciprocal-space imaging performed via SANS at the instrument SANS-1, we also employed magnetic force microscopy (MFM) to complement our SANS data with the real-space imaging of the surface of a bulk crystal. As the result of this approach, we were able to demonstrate that the magnetic structure of the bulk Mn_{1.4}PtSn differs dramatically from the LTEM observations made on thin plates reported previously.

Fig. 1(a) shows a typical SANS pattern of Mn_{1.4}PtSn. The sample was oriented with its tetragonal *c* axis parallel to the incident neutron beam. Thus, the scattering pattern in Fig. 1(a) represents spin-texture modulations in the *ab* plane of Mn_{1.4}PtSn. As can be seen, the scattering is diffuse and does not have sharp features, such as the Bragg peaks one would expect in SANS from helimagnets. This is in strong contrast to the LTEM observations of the helical spin structure with the period of ~100 nm in the thin lamellae samples, and implies that the magnetic ground state of the bulk Mn_{1.4}PtSn is not a spin helix, as was previously

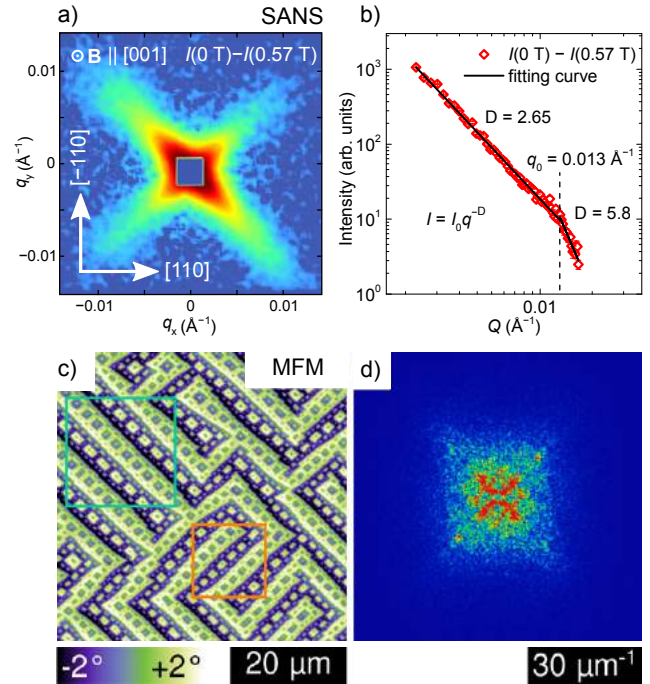


Fig. 1: Anisotropic fractal domain walls in bulk Mn_{1.4}PtSn. SANS intensity pattern (a) and the SANS intensity profile vs *Q* parallel to (100) (b) MFM measurement of the (001) surface of the crystal (c) and its Fourier transform (d).

anticipated. The SANS pattern observed is diffuse yet strongly anisotropic and can be viewed as four streaks, which point to the crystallographic $\langle 100 \rangle$ directions.

The analysis of the SANS intensity profiles [Fig. 1(b)] revealed that the radial intensity distribution follows $I \propto q^{-D}$ with $D = 2.65$ for momenta below 0.013 \AA^{-1} down to the lowest accessible momentum of $\sim 0.002 \text{ \AA}^{-1}$, which is the signature of scattering from fractal objects. The latter implies a complex intertwined arrangement of the domain walls of the rectangular domain pattern. In agreement with SANS, the MFM image of the surface of a bulk crystal [Fig. 1(c)] shows the lamellar magnetic domains with smaller nested closure domains arranged in a way that is reminiscent of the fractals with an upper boundary of $\sim 3 \text{ \mu m}$. In the Fourier transform of the MFM image [Fig. 1(d)], the same cruciform pattern as in SANS is visible.

[1] A. S. Sukhanov et al., Anisotropic fractal magnetic domain pattern in bulk Mn_{1.4}PtSn, *Phys. Rev. B* 102, 174447 (2020)

M. Bersweiler¹, P. Bender¹, I. Peral¹, L. Eichenberger², M. Hehn², V. Polewczyk³, S. Mühlbauer⁴, A. Michels¹

¹Department of Physics and Materials Science, University of Luxembourg, Luxembourg, Grand Duchy of Luxembourg; ²Institut Jean Lamour (UMR CNRS 7198), Université de Lorraine, Nancy, France; ³Istituto Officina dei Materiali (IOM)-CNR, Laboratorio TASC, Trieste, Italy; ⁴Heinz Maier-Leibnitz Zentrum (MLZ), Technical University of Munich, Garching, Germany

Ferrimagnetic rare-earth transition-metal alloys (RE-TM) are promising candidates for various technological applications such as magneto-optical recording media, permanent magnets, or spintronic devices. Previously, all-optical switching was observed in some selected RE-TM alloys. More recently, it has been demonstrated that all-optical helicity switching occurs in more complex RE-TM systems such as multilayers, rendering them suitable candidates for optically-controlled magnetic data storage devices.

In this study, we used unpolarised small-angle neutron scattering (SANS) in combination with more conventional characterisation techniques such as magnetometry and x-ray diffraction to estimate the temperature dependence of the magnetic correlation length in a polycrystalline bulk Tb-Co ferrimagnetic alloy, one of the most promising candidate systems for the next generation of magnetic memories based on all-optical switching.

We conducted the experiments at SANS-1 at the MLZ on a polycrystalline $Tb_{0.15}Co_{0.85}$ sample. The measurements were carried out at room temperature (300 K) and at low temperature (5 K). By subtracting the total SANS cross section measured at the highest field (near saturation) from that at

remnance, we obtained the purely magnetic SANS cross section, which we have further analysed.

Our magnetometry results (Fig. 1a) suggest that the reversal at 300 K is similar to that expected for a soft polycrystalline ferrimagnet, whereas at 5 K the characteristic shape of the hysteresis indicates the nucleation and propagation of magnetic domains (see Fig. 1b). In Fig. 1c, the magnetic SANS cross section at 300 K exhibits at low- q a Porod-like behaviour, which confirms that at room temperature both the Co and Tb moments are correlated over large volumes with correlation lengths of at least 100 nm. At 5 K, on the other hand, the magnetic SANS signal deviates from the room-temperature measurement, and analysis in terms of a Lorentzian-squared scattering function reveals a reduced correlation length of around 4.5 nm. This result, in combination with the magnetisation data, indicates the formation of domains within the ferrimagnet, one dimension being in the nm range. We relate our results to the temperature dependence of the magnetic anisotropy of $TbCo_5$, which is dominated by the Tb sublattice for temperatures below 300 K.

[1] M. Bersweiler et al., *Magnetic correlations in polycrystalline $Tb_{0.15}Co_{0.85}$* *J. Phys. D: Appl. Phys.* **53**, 335302 (2020)

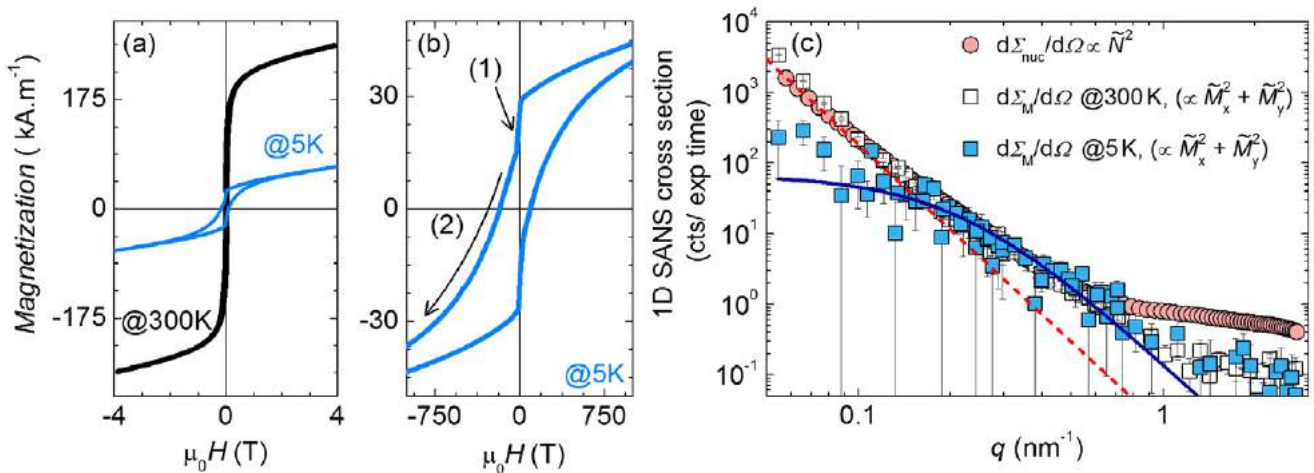


Fig. 1: (a) Magnetisation curves measured in a field range of ± 4 T at 300 K and 5 K. (b) Zoom of the magnetisation curve measured at 5 K in a field range of ± 1 T. The onset of nucleation and propagation of the magnetic domains are sketched by the arrows (1) and (2), respectively. (c) Red filled circles: nuclear SANS cross section $d\Sigma_{nuc}/d\Omega$ as a function of momentum transfer q . Colored filled squares: radially-averaged magnetic SANS cross sections $d\Sigma_M/d\Omega$ along the field direction at 300 K (white filled squares) and at 5 K (blue filled squares). Red dashed line: power law $d\Sigma_{nuc}/d\Omega \propto q^{-4}$. Blue solid line: Lorentzian-squared fit of the transverse scattering contribution at 5 K to determine the magnetic transverse correlation length l_c . Note: the magnetic SANS cross section intensities at 300 K and at 5 K have been rescaled to the nuclear 2D SANS cross section intensity for better comparison. (log-log scale).

Yu. N. Khaydukov^{1,2}, A. M. Petrzikh³, T. A. Shaikhulov³, K. L. Stankevich³, N. V. Andreev⁴, G. A. Ovsyannikov³

¹Max Planck Institute for Solid State Research, Stuttgart, Germany; ²Max Planck Society Outstation at the MLZ, Garching, Germany; ³Kotel'nikov Institute of Radio Engineering and Electronics RAS, Moscow, Russia; ⁴National University of Science & Technology (MISIS), Moscow, Russia

Transition metal oxides (TMOs) are nowadays a subject of intense activity in condensed matter physics. The 3d-TMOs have various functionalities, including ferromagnetism due to the strong electron-electron correlation. However, the spin-orbit interaction is usually weak or insignificant in 3d-TMOs. On the other hand, 5d-TMOs attract considerable interest due to the occurrence of a strong spin-orbit interaction, which coexists along with the electron-electron interaction. The combination of spin-orbit interaction and electron-electron interaction makes it possible to realise several new quantum states of matter, such as the topological Mott insulator, quantum spin and the anomalous Hall effect, Weyl semimetals and high-Tc superconductivity. The contact between 3d- and 5d-TMOs provides a unique interface in which the existence and interaction of electron-electron and spin-orbit interactions are possible, unlike the well-studied 3d/3d-TMO-interfaces.

In our recent work [1], we studied the magnetic and transport properties of a 3d/5d $\text{La}_{0.7}\text{Sr}_{0.3}\text{MnO}_3/\text{SrIrO}_3$ (LSMO/SIO) heterostructure by means of several techniques, including polarised neutron reflectometry (PNR) conducted at the reflectometer NREX. For the PNR experiment we designed the sample such that it functions as a neutron waveguide. To do this, we covered the studied LSMO(50 nm)/SIO(44 nm) heterostructure with a Au(70 nm) capping layer. Fig. 1a shows the PNR data measured at $T = 275$ K at practical remanence (a small guide field $H = 50$ e was applied along

the [100] LSMO axis to keep polarisation). The waveguide structure allowed us to observe a strong spin-flip (SF) peak $\text{RSF}(\text{QWG}) = 12\%$ at the resonant position $= 0.16 \text{ nm}^{-1}$. At the same time, we observed a non-zero spin asymmetry with a maximum of $S = -20\%$ above the critical edge. This state can be quantitatively described by a LSMO moment of $2 \mu_B/\text{Mn}$ tilted by an angle $\alpha = 38^\circ$ with respect to the external field. This angle within the experimental accuracy corresponds to the [110] axis of LSMO, its magnetic easy axis. On cooling the sample down to 3 K, we observed that the SF intensity was reduced by a factor of 3 while the spin asymmetry was increased by a factor of ~ 2 (Fig. 1b). This behaviour can naturally be explained by the rotation of the magnetisation vector of LSMO closer to the external field. Quantitatively we can describe the data at 3 K by an LSMO moment of $3.7 \mu_B/\text{Mn}$ tilted by an angle $\alpha = 26^\circ$.

Thus, in the PNR experiment we observed the rotation of the LSMO magnetic vector at remanence upon cooling of the sample. This rotation can be explained by the emergence of an exchange interaction at the LSMO/SIO interface, which is non-collinear to the direction of the LSMO easy axis. Competition between the anisotropy energy within the LSMO layer and the exchange energy at the LSMO/SIO interface leads to the rotation of the remanent magnetic moment of LSMO out from the [110] LSMO direction.

[1] G. A. Ovsyannikov, *Magnetism at an iridate/manganite interface: Influence of strong spin-orbit interaction*, *Phys. Rev. B* 102, 14402 (2020)

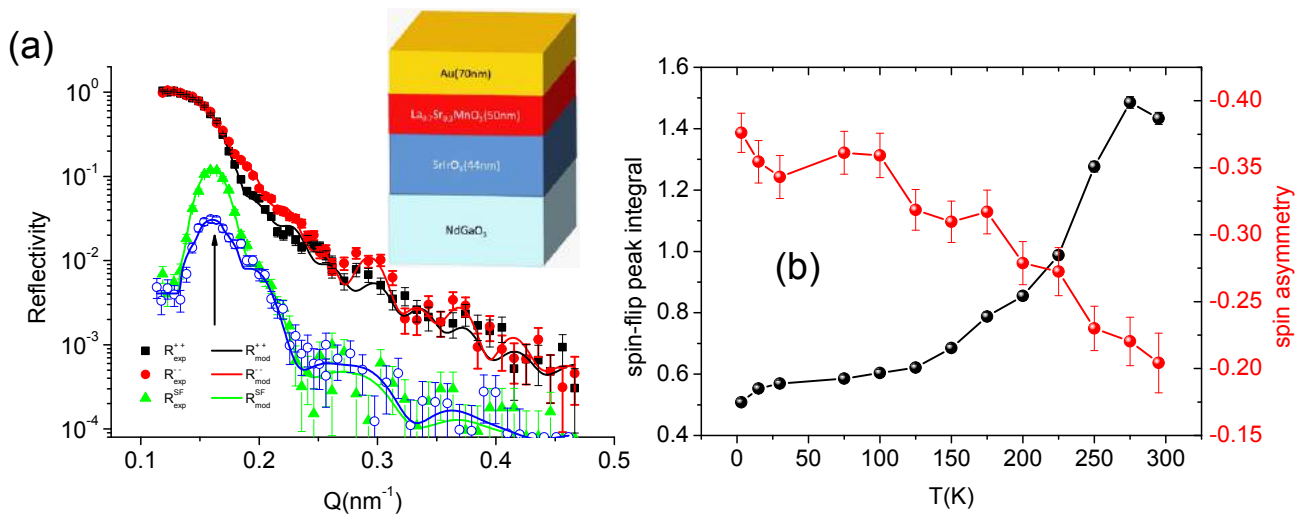


Fig. 1: (a) Experimental (dots) and model (lines) polarised neutron reflectivities measured at $T = 275$ K. Additionally spin-flip channel at 3 K is shown by blue color. Arrow in (a) shows the position of the waveguide peak. Inset in (a) shows the sketch of the structure. (b) The temperature dependence of the integrated spin-flip scattering (black) and averaged spin-asymmetry (red).

S. Pütter¹, P. Schöffmann^{1,2}, J. Schubert³, W. Zander³, J. Barthel⁴, P. Zakalek⁵, M. Waschk⁵, R. Heller⁶, T. Brückel^{2,5}

¹Jülich Centre for Neutron Science (JCNS) at MLZ, Forschungszentrum Jülich GmbH, Garching, Germany; ²Lehrstuhl für Experimentalphysik IVc, Jülich-Aachen Research Alliance, JARA-FIT, RWTH Aachen University, Aachen, Germany; ³Peter Grünberg Institute (PGI-9) and JARA-Fundamentals of Future Information Technology, Forschungszentrum Jülich GmbH, Jülich, Germany; ⁴Ernst Ruska-Centre for Microscopy and Spectroscopy with Electrons Materials Science and Technology (ER-C-2), Forschungszentrum Jülich GmbH, Jülich, Germany; ⁵Jülich Centre for Neutron Science (JCNS-2) and Peter Grünberg Institute (PGI-4), JARA-FIT, Forschungszentrum Jülich GmbH, Jülich, Germany; ⁶Institute of Ion Beam Physics and Materials Research, Helmholtz-Zentrum Dresden-Rossendorf e.V., Dresden, Germany

Prerequisite for a successful scattering experiment is a high quality sample. JCNS at MLZ provides the opportunity to grow high quality thin film samples by Molecular Beam Epitaxy (MBE) on-site. In the case of a compound such as strontium cobaltite (SrCoO_{2.5+δ}, SCO), high quality also refers to the stoichiometry, especially the ratio of the Co/Sr content. For MBE growth, Co and Sr deposition rates can be tuned independently. Hence, to distinguish different stoichiometries, in-situ methods are preferred to methods that can only be applied after sample preparation, such as Rutherford backscattering spectroscopy (RBS) or X-ray diffraction (XRD).

We have found that the reflection high energy electron diffraction (RHEED) pattern of SCO thin films is very sensitive to Co/Sr stoichiometry. A stoichiometric sample exhibits well-defined Bragg spots and a Laue ring as well as faint indications of Kikuchi lines, Fig. 1a. The stoichiometry was calibrated by RBS measurement. The corresponding Atomic Force Microscopy (AFM) image (Fig. 1c) exhibits terraces with length of about 0.2 μm and height of 0.9 nm, which is close to half of a unit cell of SCO, and a rms roughness of 0.45 nm.

Co excess of 12% adds small and sharp speckles to the RHEED pattern which correlates with additional 3-dimensional structures with good crystallinity (Fig. 1b). A comparison of the corresponding XRD measurement does not reveal any difference for the samples (Fig. 1d). Only if the Co excess is further increased (30%) peaks of CoO are detected in XRD (not shown). Hence, we may conclude that surplus Co is precipitated into CoO crystallites. This was also cross checked by transmission electron microscopy (TEM) and energy dispersive X-ray spectroscopy (EDX). Accordingly, we may assign the elongated structures of

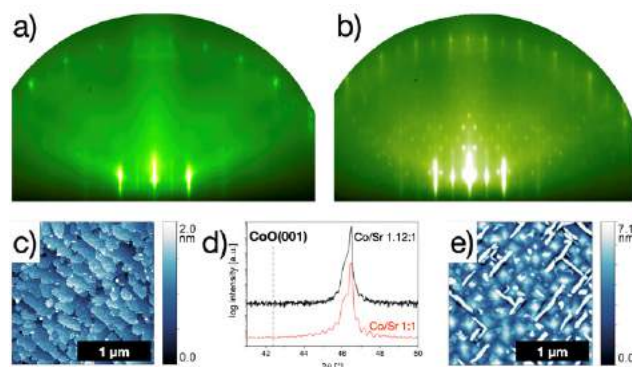


Fig. 1: RHEED patterns of SrCoO_{2.5} thin films grown on SrTiO₃(001) with a) Co/Sr ratio of 1:1 and b) 12% Co excess. Corresponding AFM measurements of same samples with c) stoichiometric and e) 12% Co excess and d) comparison of the corresponding XRD peaks. RHEED at 15 keV.

average length of 163 nm and width of 60 nm in the AFM image of the 12% Co excess sample to CoO precipitates (Fig. 1e). In contrast, for Co deficiency the RHEED pattern becomes washy, indicating diminishing crystallinity which is also proven by XRD.

Analysing the evolution of the RHEED patterns with varying Co/Sr stoichiometry during growth enables quick and easy determination of Co excess or deficiency in the SCO film. RHEED turns out to be extremely sensitive to even small amounts of Co excess and it makes it possible to adjust the growth rates during sample preparation to finally obtain a RHEED pattern of the stoichiometric sample. This is especially helpful since one of the major advantages of MBE growth is the ability to adjust the stoichiometry at will and study the influence of stoichiometric variation on the properties of the film. In this way, the stoichiometry and crystallinity are assessed in-situ and fast.

[1] P. Schöffmann et al., *Tuning the Co/Sr stoichiometry of SrCoO_{2.5} thin films by RHEED assisted MBE growth*, *Mater. Res. Express* 7, 116404 (2020)

How do peptides kill bacteria – an insight from neutron scattering

J. E. Nielsen¹, V. Pipich², H. Jenssen³, R. Lund¹

¹Department of Chemistry, University of Oslo, Norway; ²Jülich Centre for Neutron Science (JCNS) at MLZ, Forschungszentrum Jülich GmbH, Garching, Germany; ³Department of Science and Environment, Roskilde University, Roskilde, Denmark

Bacterial resistance towards conventional antibiotics represents a major stumbling block in modern medicine and desperately calls for new compounds. Antimicrobial peptides (AMPs) occur in many species in nature and form the first line of defense in the so-called innate humane system to fight a broad spectrum of bacteria, fungi, viruses and even cancer cells. However, there is no clear general consensus for the mechanism of AMPs, although it is generally believed that they primarily insert and form some kind of “pore” in the cell membrane which causes cell death.

We set out to investigate the exact microscopic mechanism using small-angle neutron/X-ray scattering (SANS/SAXS) techniques [1]. Contrary to previous studies, we have focused both on changes in the structure and the dynamics of the lipid membrane upon interaction with the antimicrobial peptides. A model was developed to describe the scattering from the different contributions of the lipid/peptide components demonstrating that the AMP, indolicidin, preferentially sits on the interface between the hydrophobic lipid tails and head groups (Fig. 1A). Given the weak perturbation of the membrane and the apparent absence of “pores” at physiologically relevant concentrations, the killing mechanism of indolicidin remained a bit of a mystery.

Using time-resolved SANS (TR-SANS) at KWS-1 and KWS-2, MLZ we showed that the lipid dynamics is considerably accelerated in the presence of AMPs [1]. The method, illustrated in Fig. 1B, is based on mixing fully deuterated and proteated vesicles in a zero average contrast buffer solution. Upon molecular diffusion, the contrast decreases over time and minimal contrast is only achieved if the lipids undergo so-called flip-flop, i.e. inter-bilayer diffusion from one leaflet to another. The results show that the peptides significantly accelerate both molecular exchange and lipid flip-flop. However, the SAXS data fits did not reveal any significant protrusion through the membrane that would indicate a pore. We thus speculate that the increasing lipid flip-flop rate drives the transport of ions and scrambles the lipid composition, which may lead to bacterial death.

In summary, by using X-ray and neutron scattering techniques, we show that a wide range of AMPs cause a general acceleration of essential lipid transport processes, without necessarily significantly altering the bilayer or creating specific pores. This provides a plausible mode of action that can be exploited to design new antibiotics against multi-drug resistant bacteria.

[1] J. E. Nielsen et al., *Beyond structural models for the mode of action: How natural antimicrobial peptides affect lipid transport*, *J. Coll. Int. Sci.* 582, 793 (2021)

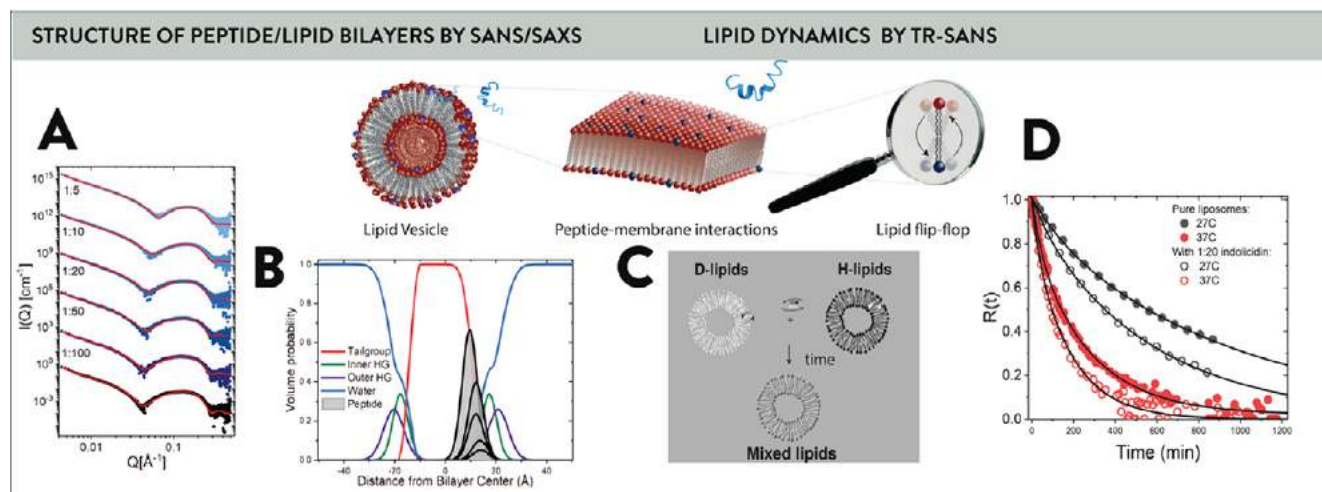


Fig. 1: Study of indolicidin, and the interactions with lipid membranes (A) SAXS analysis of the peptide interaction with lipid vesicles revealing the preferred location within the bilayer. (B) Resulting density profiles across the bilayer including all lipid and peptide components. (C) Illustration of the TR-SANS contrast variation method based on mixing deuterated and proteated lipid vesicles in a buffer that matches the average H/D composition. (D) Shows the resulting experimental decay function describing the extent of lipid “flip-flop” and exchange as a function of time. Both processes are accelerated in the presence of AMPs (open data points).

¹Departamento de Química, Facultad de Ciencias, University of Navarra, Pamplona, Spain; ²ISTUN Instituto de Salud Tropical, Department of Microbiology and Parasitology, University of Navarra, Navarra Institute for Health Research (IDISNA), Pamplona, Spain; ³IQMAAB, Department of Materials Science and Engineering, Universidad Carlos III of Madrid, Leganés, Spain; ⁴Jülich Centre for Neutron Science (JCNS) at MLZ, Forschungszentrum Jülich GmbH, Garching, Germany

Miltefosine (MF), an alkylphospholipid originally developed to treat breast cancer, has become the first effective oral treatment against leishmaniasis, a neglected tropical disease considered the world's second leading cause of death by a parasitic agent after malaria. MF exhibits dose-limiting gastrointestinal side effects in patients and its penetration through lipophilic barriers is reduced. These drawbacks can be overcome by using nanocarriers.

To this end, we propose a reformulation of MF by incorporating the drug into micelles formed of block copolymers whose hydrophilic part is poly(ethylene)oxide (PEO). On the one hand, we have used D- α -tocopheryl polyethylene glycol succinate (TPGS), a pegylated derivative of vitamin E approved by the FDA. The other type of block copolymers considered are poloxamines (Tetronic[®]), X-shaped block copolymers of PEO and polypropylene oxide (PPO). Specifically, we have investigated the structures formed with Tetronic 904 (T904), relatively small and lipophilic, and 1107 (T1107), a larger poloxamine that can form gels under certain conditions.

Small angle neutron scattering (SANS) experiments conducted at the instrument KWS-2 revealed that MF self-aggregates into stable monodisperse micelles. When MF and

the three polymeric surfactants are combined, spherical core-shell micelles form over a wide range of temperatures. The lipophilic blocks of the copolymers are in close contact with the hydrophobic tail of the drug, and a highly hydrated hydrophilic shell is formed by the PEOs and the zwitterion head group of the drug.

The precise composition of the MF-loaded copolymer micelles was assessed using SANS, TPGS being the surfactant that incorporates most MF unimers. In the case of the Tetronic copolymers, certain differences in the structure were observed depending on the block length of the molecule. In T904-MF, the number of MF molecules per mixed micelle is independent of the temperature and the aggregates are fully formed at 37°C (Fig. 1), while T1107-MF requires higher temperatures (50°C) to load the same number of MF molecules, in accordance with the micellisation behaviour of both poloxamines. At high concentrations of T1107 (> 20%), the gelation of the system occurs, and the analysis of the SANS data using different paracrystal models reveals a BCC (body centered cubic) structure of the gel (inset Fig. 1), in which the mixed micelles are packed, with little effect on the structure when the drug is incorporated.

MF leishmanicidal activity is increased for all the formulations with the copolymers, particularly for the T904-MF composition. The effectiveness on intracellular amastigotes, the form of the parasite within the host, at low concentrations of the drug is only observed with this formulation. This is most likely due to its more efficient formation of micelles under biological conditions. Hence, considering that amastigotes inside the macrophages are the principal target for leishmaniasis treatment, the incorporation of MF in T904 to form polymeric mixed micelles seems a promising formulation to treat this disease, which would permit reducing the concentration of MF to attain the same therapeutic effect of the drug alone.

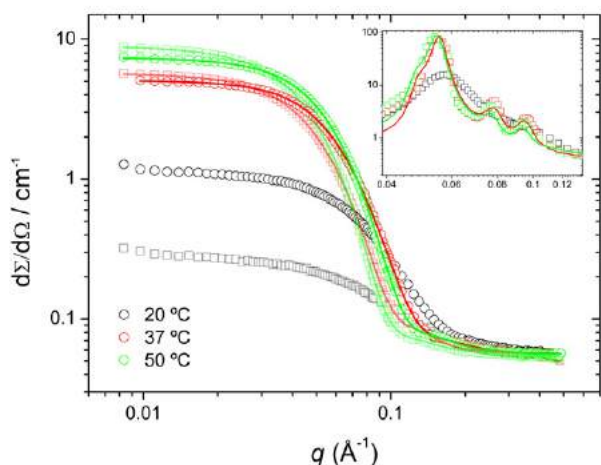


Fig. 1: SANS curves of 1% T904 (□) and 1% T904 + 0.2% MF (○) in D₂O at 20, 37 and 50°C. Solid lines correspond to the fits to a core-shell spheres with a hard spheres structure factor model. Inset: results on 25% T1107 + 0.2% MF in D₂O with fits to a BCC paracrystal model.

[1] J. Puig-Rigall et al., *Structural characterization by scattering and spectroscopic methods and biological evaluation of polymeric micelles of poloxamines and TPGS as nanocarriers for miltefosine delivery*, *Int. J. Pharm.* 578, 119057 (2020)

Thylakoid membrane reorganisations and non-photochemical quenching

R. Ünneper¹, S. Paul², O. Zsiros³, L. Kovács³, N. K. Székely⁴, G. Steinbach³, M. S. Appavou⁴, P. Porcar⁵, A. R. Holzwarth², G. Garab³, G. Nagy⁶

¹Centre for Energy Research, Budapest, Hungary; ²Max Planck Institute, CEC, Mühlheim, Germany; ³Biological Research Centre, Szeged, Hungary; ⁴Jülich Centre for Neutron Science (JCNS) at MLZ, Forschungszentrum Jülich GmbH, Garching, Germany; ⁵Institut Laue-Langevin, Grenoble, France; ⁶Oak Ridge National Laboratory, Oak Ridge, USA

Photosynthesis is the energetic basis of virtually all life on Earth; it also creates and maintains the oxygenic atmosphere of our planet. In oxygenic photosynthetic organisms the energy-transducing functions are accommodated in the thylakoid membranes, which are assembled into robust multilamellar structures. In green plants, these membranes are differentiated into stacked granum and unstacked stroma regions. Photosynthetic organisms often experience extremely large and rapid variations in the intensity of incident solar radiation, which thus require quick adjustments of their photosynthetic machinery – to warrant high efficiency of energy conversion in low-light and safe dissipation of the excess excitation energy in high-light. One of the most important photoprotective mechanism is the non-photochemical quenching (NPQ) of the first singlet excited state of chlorophyll-a, which occurs on a time-scale of minutes. Although NPQ has been extensively studied, its relationship with putative changes in the thylakoid membrane ultrastructure has not been elucidated.

To monitor membrane reorganisations *in vivo*, non-invasive techniques are required that are capable of providing time-resolved structural information on the mesoscopic scale. Thus, we performed small angle neutron scattering (SANS) experiments under NPQ conditions. The measurements were performed, with a time-resolution of 1 min using the KWS-2 beamline, on living leaf segments of the rainforest plant *Monstera deliciosa* - possessing giant grana with dozens of stacked thylakoids and intense NPQ.

We have shown that NPQ-inducing illuminations caused strong diminishments in the periodic order of the stacked membranes and slightly decreased their average repeat distance (Fig. 1). Similar to NPQ, these reorganisations occurred faster upon increasing the light intensity and were accelerated upon repeated illumination of the leaves; the relaxation kinetics of NPQ and variation of the SANS profiles also resembled each other. Surprisingly, however, in the presence of the electron transport inhibitor diuron, which suppresses NPQ, only the relaxation kinetics of NPQ was impeded while the structural changes were hardly inhibited. Hence, our data revealed that the light-induced dark-reversible reorganisations on the mesoscopic scale do not activate but appear to enable microscopic changes, conditioning NPQ, which occurs on the microscopic scale. Further, by using magnetically aligned isolated thylakoid membranes, oriented in different directions, and special illumination of the leaves, we have shown that the decrease of the SANS peak does not originate from light-induced redistribution and reorientation of chloroplasts inside the cells, a light-avoidance mechanism. In general, our studies show that thylakoid membranes cannot be portrayed as merely scaffolding the protein complexes, but appear to actively participate in regulatory processes, and that SANS is ideally suited to monitor changes in their multilamellar organisation.

[1] R. Ünneper et al., *Thylakoid membrane reorganizations revealed by small-angle neutron scattering of *Monstera deliciosa* leaves associated with non-photochemical quenching*, *Open Biol.* 10, 200144 (2020)

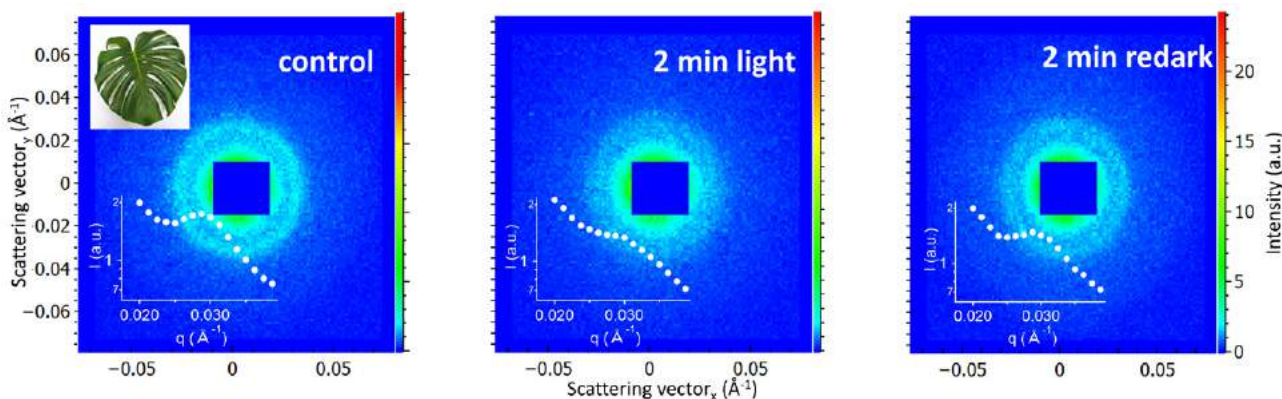


Fig. 1: Two-dimensional and one-dimensional (insets) small angle neutron scattering profiles of heavy-water infiltrated *M. deliciosa* leaf segment in the dark (left), upon illumination with white light of $300 \mu\text{mol photons m}^{-2} \text{s}^{-1}$ (middle), and in redark (right).

J.-J. Kang¹, K. Shehu¹, F. A. Jung¹, C.-H. Ko¹, L. C. Barnsley², C. Sachse³, R. Jordan³, C. M. Papadakis¹¹Physics Department, Soft Matter Physics, Technical University of Munich, Garching; ²Jülich Centre for Neutron Science (JCNS), Forschungszentrum Jülich GmbH, Garching; ³Fakulty of Chemistry and Food Chemistry, Technische Universität Dresden, Dresden

Molecular bottle brushes (MBBs) are comb-like polymers featuring a backbone that is densely grafted with side chains (Fig. 1). These offer numerous possibilities for tuning their properties and functionality, enabling applications such as smart nanocarriers. When the side chains exhibit lower critical solution temperature (LCST) behaviour, their dehydration is expected to result in strong structural changes of the entire MBB.

In the present work, the LCST behaviour of a $PiPOx_{100}$ - g - $PEtOx_{17}$ MBB in aqueous solution is investigated, where $PiPOx$ and $PEtOx$ stand for poly(2-isopropenyl-2-oxazoline) and poly(2-ethyl-2-oxazoline) [1]. $PEtOx$ homopolymers feature LCST behaviour with a cloud point $T_{cp} \approx 67^\circ\text{C}$. For aqueous solutions of $PiPOx_{100}$ - g - $PEtOx_{17}$, however, the cloud point turned out to be 40.5°C , thus strongly reduced compared to the homopolymer solution. To characterise the changes in the size, shape and inner structure of the MBBs around the cloud point, small-angle neutron scattering (SANS) measurements were performed on a MBB solution in D_2O at the SANS instrument KWS-1.

The SANS data (Fig. 1a) feature a shallow maximum along with a shoulder in the range of momentum transfers $q = 0.1$ - 2 nm^{-1} , which are attributed to the structure factor of the MBBs, describing their correlation and their form factor, describing their size and shape. The form factor of cylinders is used for modeling the data. The cross-sectional radius R is constant at $\sim 2.7\text{ nm}$ in the entire temperature range, whereas the length L increases from 12.5 nm at 25°C to 20 nm at the cloud point and decreases again upon further heating to 12.4 nm at 50°C (Fig. 1b). Thus, as the cloud point is approached, the MBBs stretch along the long axis, which is attributed to the dehydration of the $PEtOx$ side chains that leads to a straightening of the brush due to the spatial limitation in the central part of the molecule. At the cloud point, the overall collapse of the MBB results in a decrease of their length (Fig. 1c). In summary, SANS allowed us to characterise in detail the temperature-dependent structures of a MBB with thermoresponsive side arms. These results pave the way for studies of more complex smart MBBs.

[1] J.-J. Kang et al., A molecular brush with thermoresponsive poly(2-ethyl-2-oxazoline) side chains: a structural investigation, *Colloid. Polym. Sci.* 299, 193 (2021)

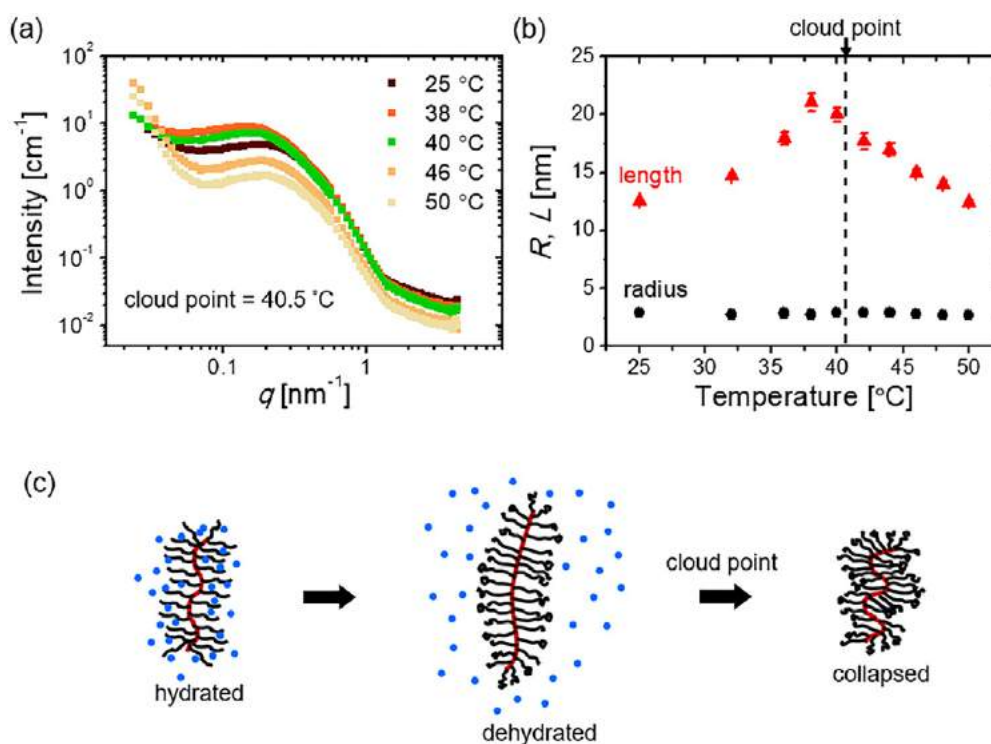


Fig. 1: (a) SANS data from a 30 g L^{-1} solution of $PiPOx_{100}$ - g - $PEtOx_{17}$ in D_2O . (b) Resulting cross-sectional radius and length of the MBBs in dependence on temperature across T_{cp} (vertical dashed line). (c) Schematic representation of the structural evolution of the MBBs upon heating. The blue spheres indicate the water molecules.

J. Larsson¹, A. E. Leung², C. Lang³, B. Wu³, M. Wahlgren⁴, T. Nylander^{1,5}, S. Ulvenlund^{4,6}, A. Sanchez-Fernandez⁴

¹Physical Chemistry, Department of Chemistry, Lund, Sweden; ²European Spallation Source, Lund, Sweden; ³Jülich Centre for Neutron Science (JCNS) at MLZ, Forschungszentrum Jülich GmbH, Garching, Germany; ⁴Food Technology, Engineering and Nutrition, Lund, Sweden; ⁵NanoLund, Lund University, Lund, Sweden; ⁶EnzaBiotech AB, Scheelevägen Lund, Sweden

Since society strives towards using more environmentally friendly products, it becomes important to find sustainable amphiphilic molecules that can be used in formulated products such as cosmetics, food and drugs. Here, sugar-based surfactants are particularly interesting as they can be produced from renewable resources and their solution and interfacial behaviour can be controlled by changing the molecular structure of the surfactant. Long-chain maltoside surfactants have been shown to act as rheological modifiers, but suffer from limited solubility at room temperature that limits their applicability. Here, we present for the first time the synthesis, self-assembly and rheology of the corresponding sugar-based surfactant with an unsaturated chain.

Palmitoleyl- β -D-maltoside (β -C₁₆₋₁G₂) was synthesised at the DEMAX, the European Spallation Source Deuteration Laboratory. The double bond in the surfactant tail was introduced to reduce the Krafft point compared to the saturated analogue, and thereby extend the stability to significantly lower temperatures. The β -C₁₆₋₁G₂ surfactant solution was shown to behave as a non-Newtonian fluid with viscoelastic

properties, rather similar to the corresponding surfactant with a saturated chain. Understanding the self-assembly of the surfactant will not only help us to understand the rheological behaviour, but also guide the design of formulated products using sustainable surfactants (e. g. formulations for drug delivery). Therefore, the nanostructure of the system was probed using small-angle neutron scattering (SANS) at the Heinz Maier-Leibnitz Zentrum. The combined capabilities of the KWS-2 and KWS-3 instruments made it possible to simultaneously investigate the wide range of length-scales in the micelle structure (Fig. 1). In addition, the neutron contrast was co-refined with small-angle X-ray scattering data in order to resolve the internal structure and composition of the micelle. These investigations showed the formation of worm-like micelles (contour length = 9200 Å, persistence length = 215 Å) with a hydrophobic core (radius = 15.1 Å) surrounded by a hydrated shell (thickness = 14.5 Å) at room temperature. The combination of scattering methods also showed that micelle structures prevail in a wide temperature range. This is not possible with the saturated surfactant analogue hexadecylmaltoside which precipitates out of solution below ca. 35°C, although it shows similar self-assembly structures. These results suggest that the worm-like micelles form an entangled network above the crossover concentration, which is reflected in the rheological properties of the system.

The unsaturated surfactant presented here expands the applicability of sustainable long-chain surfactants at an extended temperature range between 0 and 100°C. This study also shows the key role of the headgroup interactions in the saturated and unsaturated surfactants as they have surprisingly similar self-assembly and rheological behaviour.

[1] Larsson et al., *Tail unsaturation tailors the thermodynamics and rheology of a self-assembled sugar-based surfactant*, *J. Colloid Interface Sci.* 585, 178 (2021)

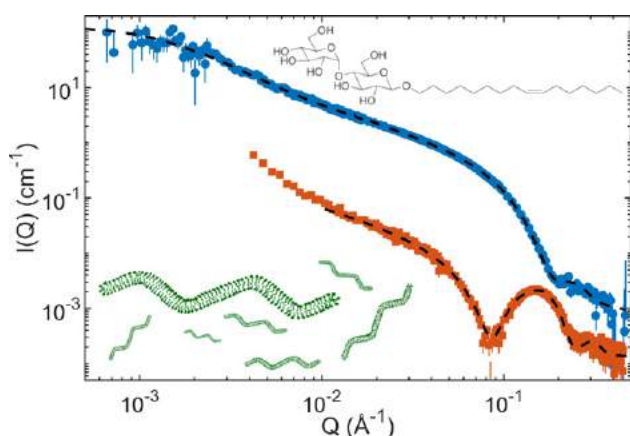


Fig. 1: SANS (blue circles) and SAXS (orange squares) data and best fits of 10 mM β -C₁₆₋₁G₂. Inset: schematic representation of the structure of WLM.

S. Pasini¹, S. Maccarrone¹, N. K. Székely¹, L. R. Stingaciu², A. P. H. Gelissen³, W. Richtering⁴, M. Monkenbusch⁵, O. Holderer¹

¹Jülich Centre for Neutron Science (JCNS) at MLZ, Forschungszentrum Jülich GmbH, Garching, Germany; ²NScD, Oak Ridge National Laboratory, Oak Ridge, Tennessee, USA; ³Institute of Physical Chemistry, RWTH Aachen University, Aachen, Germany; ⁴Institute of Physical Chemistry, RWTH Aachen University, Aachen and JARA-SOFT, Aachen, Germany; ⁵Jülich Centre for Neutron Science (JCNS) & Institute for Complex Systems (ICS), Forschungszentrum Jülich GmbH, Jülich, Germany

The structural properties of thermoresponsive, cationically poly(N-iso-propylacrylamide-co-methacrylamido propyl trimethyl ammonium chloride) microgels and the influence of the anionic electrolyte polystyrene sulfonate (PSS) on the structure and dynamics of cationic microgels have been investigated via a combination of small angle neutron scattering (SANS) and neutron spin echo (NSE) techniques. The main result of this work is the suppression of the segmental dynamics of the microgels after adding PSS to the solution.

Microgels consist of chemically cross-linked polymer chains with a typical size of the order of 100 - 1000 nm. Many microgels are thermoresponsive, which means that the solvent properties change from good to bad solvents when the temperature rises above the volume phase transition temperature (VPTT). For this reason, microgels can be designed to respond not only to changes in temperature but also pressure and acidity, and thereby making them

promising candidates for drug delivery and nanoreactors. Moreover, a better understanding of the interactions that exist between the polymer chains and added guest molecules, for example electrolytes, could help to improve the design of microgels for a specific functionality.

The cationic microgel, called PNIPAM-co-MAPTAC, was prepared in solution with heavy water, to which the anionic electrolyte polystyrene sulfonate (PSS) was added. The aim of this work was to investigate the interaction of the PNIPAM with the PSS on molecular length- and time-scales by means of a combination of SANS (KWS-2 at MLZ) and NSE (SNS–NSE).

We found that the electrolyte suppresses the segmental dynamics of the microgel's polymer chains. In the presence of PSS, the microgel transforms from its original swollen state to a more compressed state, inhibiting polymer segment movements between the crosslinks.

Indeed, prior to the addition of PSS, the microgel's polymer chains exhibit both density fluctuations and Zimm dynamics, which are segmental fluctuations in response to temperature. However, after the addition of PSS, the microgel appears in a sort of shrunken state where only density fluctuations and no Zimm dynamics are present. We believe this is due to the interaction between the ions and the unbalanced charges of the gel that tend to reduce the polymer length in a sort of pinning effect. Thus, the segmental dynamics of the crossed-linked polymer is reduced.

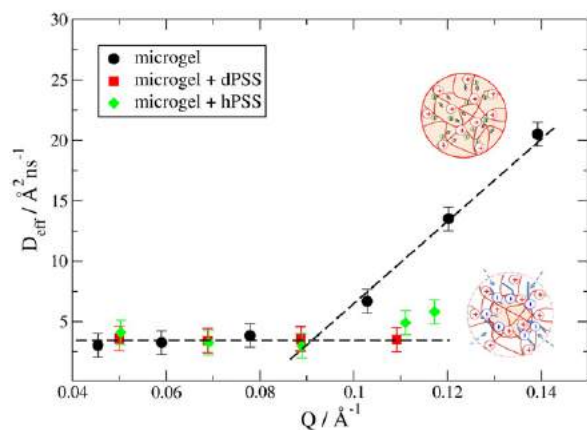


Fig. 1: Effective diffusive coefficient (normalised to Q^2) of the microgel in solution and possible representation of the interaction between the microgel and the PSS (blue segments in the sketch). Whereas the microgel alone follows a power-law ($D_{\text{eff}} \propto Q^{-3}$) typical of the Zimm dynamics, at the same length scales the effective diffusive coefficient of the samples with PSS scales “only” quadratically with the momentum transfer.

[1] S. Pasini et al., *Fluctuation suppression in microgels by polymer electrolytes*, *Struct. Dyn.* 7, 034302 (2020)

I. Russo Krauss^{1,2}, A. Picariello¹, G. Vitiello^{2,3}, A. De Santis^{1,2}, A. Koutsioubas⁴, J. E. Houston⁵, G. Fragneto⁶, L. Paduano^{1,2}

¹Department of Chemical Sciences, University of Naples Federico II, Naples, Italy; ²CSGI, Center for Colloid and Surface Science, Sesto Fiorentino (FI), Italy; ³Department of Chemical, Materials and Production Engineering, University of Naples Federico II, Naples, Italy; ⁴Jülich Centre for Neutron Science (JCNS) at MLZ, Forschungszentrum Jülich GmbH, Garching, Germany; ⁵European Spallation Source ERIC, Lund, Sweden; ⁶Institut Laue-Langevin (ILL), Grenoble, France

Superparamagnetic nanoparticles (SPIONs) are promising tools as magnetic resonance contrast agents, local heaters for hyperthermia and nanoplatforms for multimodal imaging and theranostic. However, to develop them properly, it is necessary to make them biocompatible and to investigate thoroughly their encounter with the biological world. In this respect, we studied the interaction of small iron oxide SPIONs covered by an amphiphilic double layer of oleic acid/oleylamine and 1-octadecanoyl-sn-glycero-3-phosphocholine with two abundant human plasma proteins, albumin (HSA) and transferrin (HTF). Since interaction with NPs can cause protein unfolding and result in toxic effects, we verified that SPIONs do not unfold HSA and HTF, nor significantly affect protein structure stability, by means of circular dichroism and fluorescence spectroscopy. Spectroscopic data also suggest that only HSA significantly binds SPIONs, as confirmed by fluorescence quenching experiments. With

the aim of characterising these SPION/HSA assemblies, we performed dynamic light scattering (DLS) before and after the removal of excess protein. In the presence of protein excess, DLS spectra show a population of $R_H \approx 25$ nm co-existing with the isolated HSA population; upon extensive washing of the protein excess, only SPION/HSA assemblies with $R_H \approx 10$ nm are observed, indicating that HSA is able to form both a hard and a soft corona on the SPION surface. Deeper insights into the structural feature of SPION/HSA assemblies are obtained by small angle neutron scattering (SANS) data collected on the KWS-2 instrument at the MLZ. Taking into account the structural features of SPIONs and SPION/HSA as determined by SANS and HSA shapes, we revealed a so-called side-on protein binding mode, involving one of the triangular HSA faces, and the binding of about 7 protein molecules, a value significantly lower than the maximum number of HSA molecules required to form a monolayer on the NP. HSA forms an incomplete protein shell tightly bound on the SPION surface. This modification may affect the behaviour of NPs in vivo, particularly their interaction with cells and internalisation pathways. Since the first step of NPs entry into cells is determined by their interaction with the cell membrane, we analysed the SPIONs/HSA interaction with model membranes by means of Neutron Reflectivity (NR) experiments performed on the MARIA instrument at the MLZ. Analysis of NR profiles proves that HSA/SPIONs are able to interact with and adhere to the surface of model lipid bilayers without removing lipids or affecting the membrane structure, as required for their use as imaging contrast agents. In short, the present findings reinforce the idea of amphiphiles-coated SPIONs as a biocompatible nanodevice for biomedical applications and suggest the possibility of exploiting the HSA's layer being tightly bound to the SPIONs for further functionalisation of NPs, by taking advantage of the carrier properties of this protein.

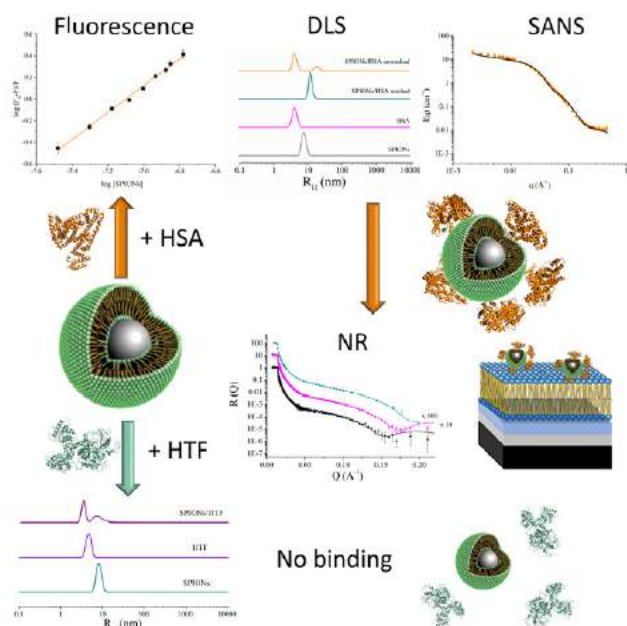


Fig. 1: Phosphocholine-decorated SPIONs (green) do not interact significantly with human transferrin (light cyan), whereas they form a well-defined assembly with human serum albumin (orange), as proved by an extensive chemico-physical characterisation including CD and fluorescence spectroscopies, DLS and SANS. NR measurements also indicate that these assemblies interact with model membranes without affecting their structures.

[1] I. Russo Krauss et al., *Interaction with human serum proteins reveals biocompatibility of phosphocholine-functionalized SPIONs and formation of albumin decorated nanoparticles*, *Langmuir* 36(30), 8777 (2020)

A. de Santis^{1,2}, G. Vitiello^{2,3}, M.-S. Appavou⁴, E. Scoppola⁵, G. Fragneto⁶, L. C. Barnsley^{4,7}, L. A. Clifton⁸, M. F. Ottaviani⁹, L. Paduano^{1,2}, I. Russo Krauss^{1,2}, G. D'Errico^{1,2}

¹Department of Chemical Sciences, University of Naples Federico II, Naples, Italy; ²CSGI, Center for Colloid and Surface Science, Sesto Fiorentino (FI), Italy; ³Department of Chemical, Materials and Production Engineering, University of Naples Federico II, Naples, Italy; ⁴Jülich Centre for Neutron Science (JCNS) at MLZ, Forschungszentrum Jülich GmbH, Garching, Germany; ⁵Max Planck Institute of Colloids and Interfaces, Potsdam, Germany; ⁶Institut Laue-Langevin (ILL), Grenoble, France; ⁷Current address: Australian Synchrotron, ANSTO, Clayton, Australia; ⁸SIS Facility, Science and Technology Facilities Council, Rutherford Appleton Laboratory, Harwell Oxford, Didcot, United Kingdom; ⁹Department of Pure and Applied Sciences, University of Urbino, Urbino, Italy

Omega-3 fatty acids, including docosahexaenoic acid (DHA), play many biological and pharmacological roles, whose origin is still debated. In particular, it has been proposed that DHA affects the function of the cell membrane and related proteins through DHA-phospholipid effects on the lipid bilayer structure. Since most studies have concerned themselves with its influence on lipid-rafts, neglecting the analysis of effects on liquid disordered (Ld) phases that constitute most of the cell membranes, we chose to fill this gap by analysing the microscopic and mesoscopic features of Ld bilayers formed by the naturally abundant 1-palmitoyl-2-oleoyl-sn-glycero-3-phosphocholine (POPC) and the increasing contents of a di-DHA glycerophosphocholine, 22:6-22:6PC. Analysis of neutron reflectivity profiles indicates that, up to 40% 22:6-22:6PC molar percent, bilayer structural features change slightly, while at high

omega-3 concentration (80% mol/mol) detachment of the lipid bilayer occurs. Cryo-TEM images, obtained at the MLZ, clearly show that in the former cases vesicles are present; while in the latter clusters of small spherical particles with no ordered repetitive units coexist with larger structures. This massive lipid rearrangement is probably the cause of the observed lipid detachment. Structural characterisation of these systems by means of small angle neutron scattering (SANS), performed on the KWS-1 instrument at the MLZ, indicates that the lamellarity of vesicles increases as the omega-3 concentration increases, up to 40% molar percent. Beyond this concentration value, the fitting of SANS data also suggests the coexistence of the different aggregates seen in micrographs, a hypothesis confirmed by dynamic light scattering measurements. Finally, by means of electron paramagnetic resonance (EPR) spectroscopy, we investigated the microstructure of POPC/22:6-22:6PC aggregates. At 40% 22:6-22:6PC molar percent, an abrupt increase of disorder of the terminal ends of acyl tails, as well as of the polarity they experience, further proves the existence of a threshold value for a structural transition. Below this threshold 22:6-22:6PC only induces a slight increase of acyl chain mobility freedom, sufficient to favour mesoscopic changes such as the increase of lamellarity seen by SANS; above it, it causes a rearrangement of the local lipid self-organisation, disfavours the formation of lamellar phases. Overall cryo-TEM, SANS and EPR indicate that, at high omega-3 concentrations, small spherical lipid aggregates are present, in which DHA acyl chains fold, exposing both the headgroup and the tail termini to the solvent, driving cluster formation. The conclusion that the omega-3 phospholipids strongly disfavour the formation of lamellar phases and induce assembly in non-lamellar structures provides a reasonable key to interpreting many different physico-chemical properties of polyunsaturated lipids and opens a new pathway towards a comprehension of their biological role.

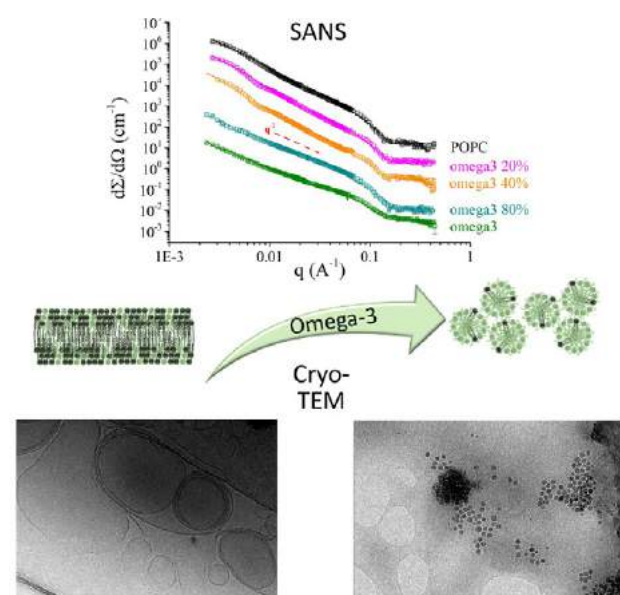


Fig. 1: Increasing the content of an omega-3 phospholipid, 22:6-22:6PC (light green), into POPC (dark green) bilayers induces a structural transition as evidenced by SANS data. In particular Cryo-TEM images of POPC rich systems (on the left) indicate the presence of vesicles, while those of omega-3 rich ones (on the right) show the presence of small spherical aggregates.

[1] A. de Santis et al., Not just a fluidizing effect: omega-3 phospholipids induce formation of non-lamellar structures in biomembranes, *Soft Matter* 16(46), 10425 (2020)

Polymorphic phase transition in supercritical (SC) carbon dioxide

V. Pipich¹, D. Schwahn²

¹Jülich Centre for Neutron Science (JCNS) at MLZ, Forschungszentrum Jülich GmbH, Garching, Germany; ²Jülich Centre for Neutron Science (JCNS-1), Forschungszentrum Jülich GmbH, Jülich, Germany

Classical thermodynamics regards supercritical fluids (SCFs) as a homogeneous phase, which opens up a pathway to transform the gas phase into the liquid phase without passing any phase transition line. This perception has changed recently, as visualised in the pressure-temperature projection of the phase diagram of CO₂ in Fig. 1 showing the gas-liquid phase transition line (solid line), the critical point (CP), as well as the Widom and Frenkel lines in the SCF regime together with SANS experimental points described in the figure caption. Both lines characterise different types of molecular density fluctuations. The Widom line is defined at the position of maximum strength of thermal density fluctuations and correlation length, whereas the Frenkel line was originally defined as a dynamic borderline between gas-like and liquid-like phases. Surprisingly, we found formation of droplets at larger pressure fields above the Widom line, as visualised in Fig. 2. These droplets differ only in number density from the SCF phase, thereby representing a polymorphic, i.e. liquid-liquid phase transition. We identified this borderline as a Frenkel line.

Molecular density is the order parameter and driving force of polymorphic phase transitions, in contrast to the chemical potential in multicomponent systems. Polymorphism has been extensively explored in supercooled liquids, whose prominent example is water showing evidence of two distinct liquid phases and a second critical point on the basis of molecular dynamic simulation. Our SANS data obtained at KWS-1 yield less complex results. In a first step, spherical droplets of dilute concentration, constant radius and increasing forward scattering $d\Sigma/d\Omega(0)$ are formed, which in a second step transform into droplets of rod-like shape and globular morphology at increasing pressure. Globular droplets do not follow the form factor of spheres at large Q , but have to be fitted with a combination of Guinier's and Porod's laws. The spherical droplets show no coarsening below ~ 130 bar, which might be attributed to small surface tension of the droplets in SCF. Furthermore, there is no indication of droplet nucleation and coarsening nor of spinodal decomposition indicating an unstable regime and a second critical point.

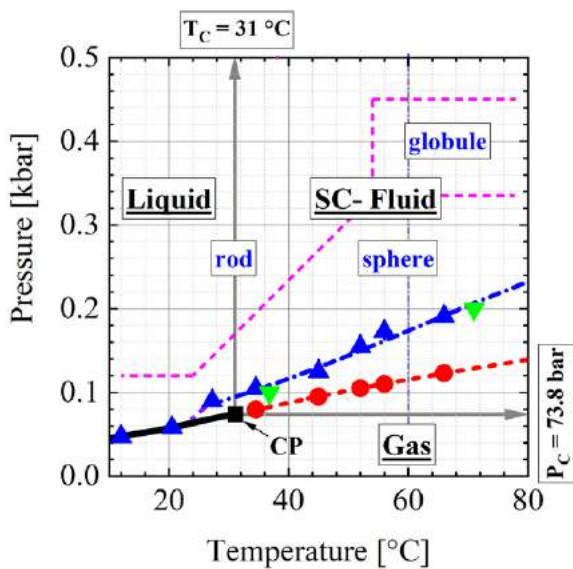


Fig. 1: Temperature-pressure plane of the CO₂ phase diagram. The solid line represents the gas-liquid phase boundary with the critical point (CP) at its endpoint. The solid grey lines with an arrow represent the borderlines of gas, liquid, and supercritical (SC) fluid phases. The dashed and dashed-dotted lines, respectively, show the Widom (red circles) and Frenkel (blue triangles (isotherm), green triangles (isobar)) lines obtained from SANS. Droplets of different shapes form above the gas-liquid and Frenkel line, obeying the class of polymorphic phase transition of one-component disordered systems such as liquid and glasses.

[1] V. Pipich and D. Schwahn, *Polymorphic phase transition in liquid and supercritical carbon dioxide*, *Sci. Rep.* 10, 11861 (2020)

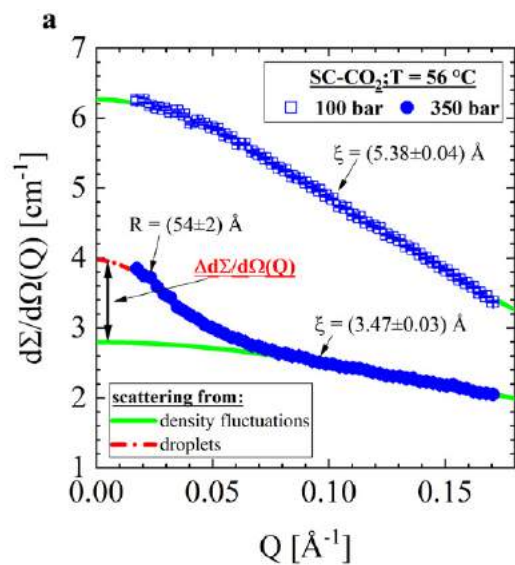


Fig. 2: Scattering pattern below and above the Widom line ($P_w = 110$ bar). At 100 bar scattering from thermal density fluctuations, whereas at 350 bar scattering (dashed-dotted line) from thermal density fluctuations (solid line) and from droplets (double arrow).

A. Beauvois^{1,2,3}, D. Vantelon², J. Jestin³, C. Rivard^{2,4}, M. B.-L. Coz¹, A. Dupont⁵, V. Briois², T. Bizien², A. Sorrentino⁶, B. Wu⁷, M.-S. Appavou⁷, E. Lotfi-Kalahroodi¹, A.-C. Pierson-Wickmann¹, M. Davranche¹

¹CNRS, Géosciences Rennes – UMR 6118, University of Rennes, Rennes, France; ²Synchrotron SOLEIL, L'Orme des Merisiers, Gif-sur-Yvette Cedex, France; ³Laboratoire Léon Brillouin, CEA Saclay, Gif-sur-Yvette Cedex, France; ⁴INRAE – UAR 1008 Transform, Nantes, France; ⁵CNRS, Inserm, BIOSIT – UMS 3480, University of Rennes, Rennes, France; ⁶ALBA Synchrotron Light Facility, Cerdanyola del Vallès, Spain; ⁷Jülich Centre for Neutron Science (JCNS) at MLZ, Forschungszentrum Jülich GmbH, Garching, Germany

Natural iron-organic matter (Fe-OM) nanoaggregates are ubiquitous in environmental systems and are known to play a crucial role in the mobility of many pollutants. The ability of Fe-OM nanoaggregates to adsorb metal(loid)s is controlled by their size, morphology and the structural arrangement between the Fe and OM phases. However, all these properties are strongly influenced by the physico-chemical conditions prevailing in the environment. The presence of calcium (Ca) is of particular interest as it is a common major cation in natural waters exhibiting high affinity for OM. In the present study, we investigated the impact of Ca on the multiscale structural organisation of Fe-OM aggregates at various Fe and Ca content for a given organic carbon (OC) concentration.

Our work demonstrates the dramatic impact of Ca on the macroscopic behaviour of Fe-OM aggregates. At low Ca content, Fe-OM aggregates stayed in a colloidal state and their observation by cryo-TEM reveals the presence of aggregates of a hundred nm. At high Ca content, we noticed a settlement of the samples for which cryo-TEM and cryo-TXM observations highlight the formation of a micrometric network. SANS (KWS-2 spectrometer) and VSANS (KWS-3 spectrometer) measurements bring out a typical size of ~400 nm in radius for OM within the colloidal suspension, while a size more than double is observed in the settling

samples. More precisely, this OM size transition occurred for $\text{Ca}/\text{OC} \geq 0.026$, showing the role of Ca in the formation of the OM network. It is confirmed by XAS at the Ca K-edge which provided evidence of the formation of Ca dimers bound to OM carboxylic groups. Calcium acts as a bridge between organic colloids and macromolecules, leading to the formation of an OM Ca-branched micrometric network, with consequences for Fe phases.

Fe is organised as Fe(III)-oligomers and ferrihydrite-like nanoparticles (Fh-like Np). For $\text{Ca}/\text{OC} < 0.026$, Fh-like Np are either isolated or bound to the OM matrix. For $\text{Ca}/\text{OC} \geq 0.026$, Fe species are embedded in the OM Ca-branched network, distant from each other. The binding of OM by Ca partially screened the interactions between OM and Fe. Consequently, the availability of Fh-like Np size and binding sites increased with the increasing Ca/OC ratio.

Our study shed new light on the behaviour of Fe-OM aggregates in environmental systems: Ca controls the mobility of Fe-OM aggregates and associated elements through the formation of a micrometric network (Fig. 1).

[1] A. Beauvois et al., *How does calcium drive the structural organization of iron-organic matter aggregates? A multi-scale investigation*, *Environ. Sci.: Nano* 7, 2833 (2020)

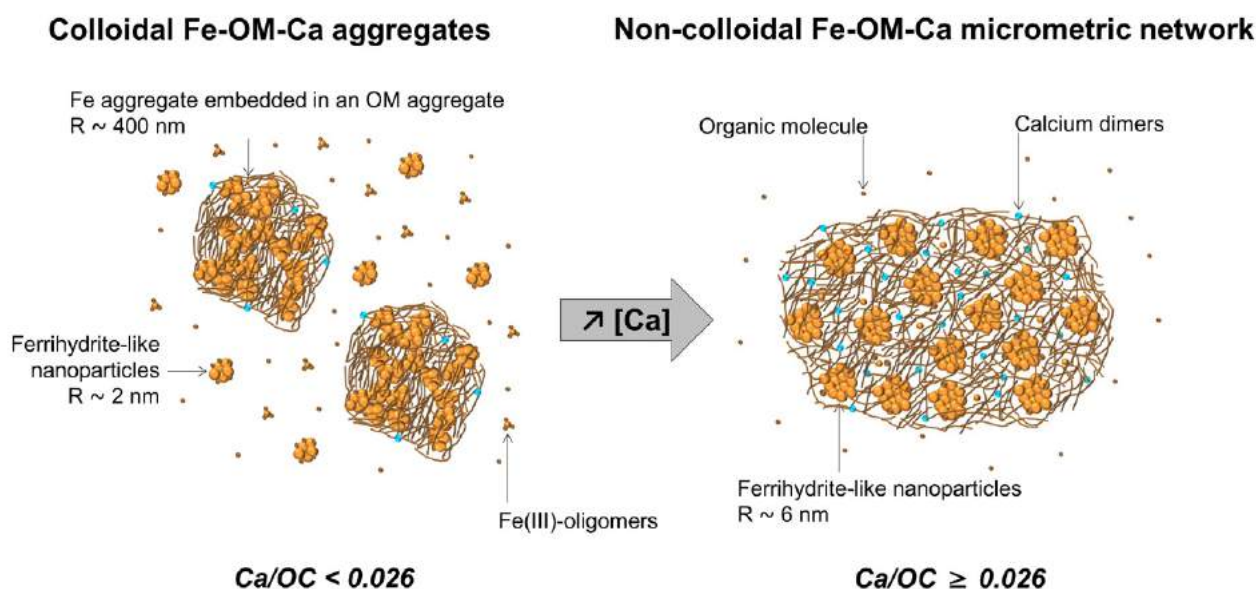


Fig. 1: Schematic representation of the structural organisation of Fe-OM aggregates depending on the Ca/OC ratio.

C. Shibazaki¹, R. Shimizu¹, Y. Kagotani¹, A. Ostermann², T. E. Schrader³, M. Adachi¹

¹Institute for Quantum Life Science, National Institutes for Quantum and Radiological Science and Technology (QST), Tokai, Japan; ²Heinz Maier-Leibnitz Zentrum (MLZ), Technical University of Munich, Garching, Germany; ³Jülich Centre for Neutron Science (JCNS) at MLZ, Forschungszentrum Jülich GmbH, Garching, Germany

Fluorescent proteins (FPs) have revolutionised imaging technology in the biological sciences. The green fluorescent protein (GFP) is one of the key FPs, both as a representative and pioneering molecule. The isolation of not only GFP but also other FPs and their protein engineering has provided the coloring diversity, with additional functions such as photoswitching leading to super-resolution microscopy. A better understanding of the structure and function for FPs will help to develop new molecular designs to generate further practical devices. Recently, we reported on a structural analysis of GFP to show the characteristic protonation (deuteration) states of the chromophore and surrounding key residues with their hydrogen-bonding network, including water molecules, via neutron crystallography (Fig. 1). The structure shows a deprotonated tyrosine hydroxyl group in the fluorescent chromophore. In addition, the protonation states of His148, as well as the state of a critical water molecule (DOD323 in Fig. 2) in direct contact with the chromophore, could be determined.

Interestingly, the DE2 atom of the imidazole ring of His148 seems to be located out of plane since the NE2 atom adopts a tetrahedral configuration rather than a sp^2 configuration, which indicates that the ND1 of His148 could have a positive charge. The configuration must be advantageous for the negative charge of the deprotonated tyrosine hydroxyl group of the chromophore. The results demonstrate that the deprotonated hydroxyl group in the chromophore and the nitrogen atom ND1 in His148 are charged negatively and positively, respectively, forming an ion pair.

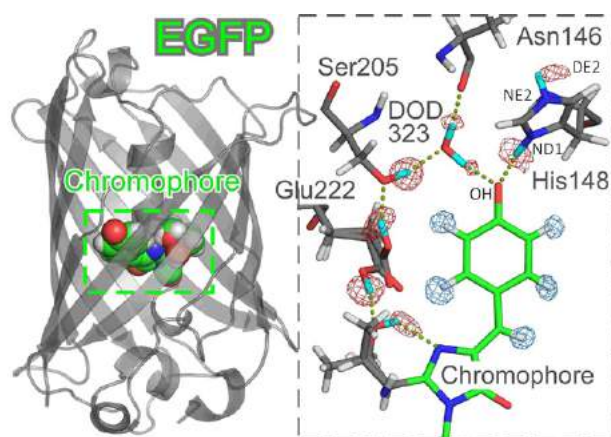


Fig. 1: The molecular structure of EGFP solved by neutron crystallography at the instrument BioDiff. The chromophore and interacting amino acids are represented in the dashed box on the right. Light blue and red omit maps show hydrogen and deuterium atoms observed by using neutrons.

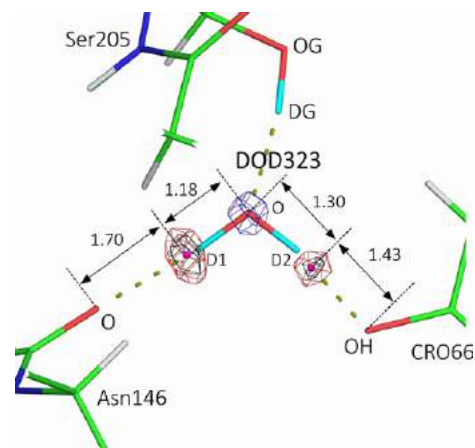


Fig. 2: The bond model of DOD323 with omit maps. $F_o - F_c$ neutron omit maps for D1 and D2 atoms for the DOD323 molecule are shown in red and black at 4.0 and 5.0 σ , respectively. $2F_o - F_c$ X-ray map for the oxygen atom is shown in blue at 5.0 σ . The magenta spheres represent the position of deuterium atoms at the centre of omit maps, respectively. The distances are indicated in a unit of Å.

DOD323 and the hydroxyl group of Ser205 are positioned between the oxygen atom OH of the chromophore (Fig. 1) and the side chain of Glu222 in the hydrogen bonding network responsible for an excited proton transfer in GFP. In this analysis, we observed two hydrogen bonds based on omit maps for the D1 atom of DOD323 and the DG atom of Ser205 (Fig. 2). The first bond forms between the O atom of DOD323 and the OG atom of Ser205, the second one between the O atom of DOD323 and the carbonyl O atom of Asn146. Notably, the positions of the two deuterium atoms of DOD323 appears to be displaced slightly to the acceptor oxygen atoms according to their omit maps (Fig. 2). The distances between the O atom of DOD323 and the centre of the omit map densities are significantly longer than the standard bond length of 0.95 Å within a water molecule (0.23 and 0.35 Å respectively). An unrestrained refinement, which introduced a slack value for the bond length to generate a square well potential, showed the movement of D1 and D2 towards the acceptor O atoms of Asn146 and the OH atom of the chromophore with a value of 0.14 and 0.18 Å, respectively. The positions of the deuterium atoms observed here might imply the formation of an intriguing electrostatic potential realised inside the protein. Our findings will provide new insights for future protein design strategies along with developments in quantum chemical calculations.

[1] C. Shibazaki et al., *Direct Observation of the Protonation States in the Mutant Green Fluorescent Protein*, *J. Phys. Chem. Lett.* 11(2), 492 (2020)

R. Schlenker^{1,2}, A.-L. Hansen¹, A. Senyshyn³, T. Zinkevich¹, M. Knapp¹, T. Hupfer², H. Ehrenberg¹, S. Indris¹¹Institute for Applied Materials (IAM), Karlsruhe Institute of Technology (KIT), Eggenstein-Leopoldshafen, Germany; ²Robert Bosch GmbH, Corporate Sector Research and Advance Engineering, Renningen, Germany; ³Heinz Maier-Leibniz Zentrum (MLZ), Technical University of Munich, Garching, Germany

Energy storage is one of the major global challenges and is becoming increasingly important as the demand for energy consuming devices grows. Batteries are most commonly used in a variety of portable applications, e.g. smart phones, laptops, and electric vehicles. Nowadays, typical batteries commonly use liquid electrolytes, but these types of electrolytes have safety concerns such as leakages and flammability. To minimise this danger, an alternative are solid-state electrolytes which have begun to be intensively investigated in the last couple of years. In addition, higher volumetric and specific energy densities can be achieved by replacing liquid electrolytes with solid-state electrolytes in combination with lithium metal anodes. The argyrodites class of materials exhibits very high ionic conductivities in the range of those observed for liquid electrolytes.

The current work [1] focuses on lithium argyrodite $\text{Li}_6\text{PS}_5\text{Cl}$ and investigates its structure and lithium pathways as structure properties highly correlate with ion migration. Using high-resolution neutron powder diffraction performed at the instrument SPODI at ambient and 500°C temperature, an additional lithium site (Li2) was experimentally found using Fourier map analysis. The lithium hopping pathways were determined using a combination of Four-

ier maps with the maximum entropy method and differential bond valence analysis. The lithium diffusion occurs in three different possible pathways: exchange within the cage segment, intra-cage and inter-cage transitions. Within the cage segment lithium moves in the hexagonal lithium units composed of closely connected Li1 and Li2 sites. Four of those hexagonal units form a tetragonal lithium cage in which the lithium moves via Li1-Li1 bridges. The inter-cage Li hopping from one cage to another proceeds through a Li1/Li2 – 48h (0.155, 0.527, 0.345) – Li1/Li2 chain. To ensure a valid system for classical approximation, the 500°C dataset was used. The activation energies for diffusion within the trigonal units (Li1-Li2), intra-cage (Li1-Li1) and inter-cage (Li1-48h-Li1) diffusion were obtained as 0.21 eV, 0.42 eV and 0.40 eV, respectively. In addition, pair distribution function analysis revealed a tilt of the $[\text{PS}_4]^{3-}$ tetrahedra that yields a local monoclinic structure. This structure modulates throughout higher R values, which leads to an average cubic structure.

[1] R. Schlenker et al., *Structure and Diffusion Pathways in $\text{Li}_6\text{PS}_5\text{Cl}$ Argyrodite from Neutron Diffraction, Pair-Distribution Function Analysis, and NMR*, *Chem. Mater.* 32(19), 8420 (2020)

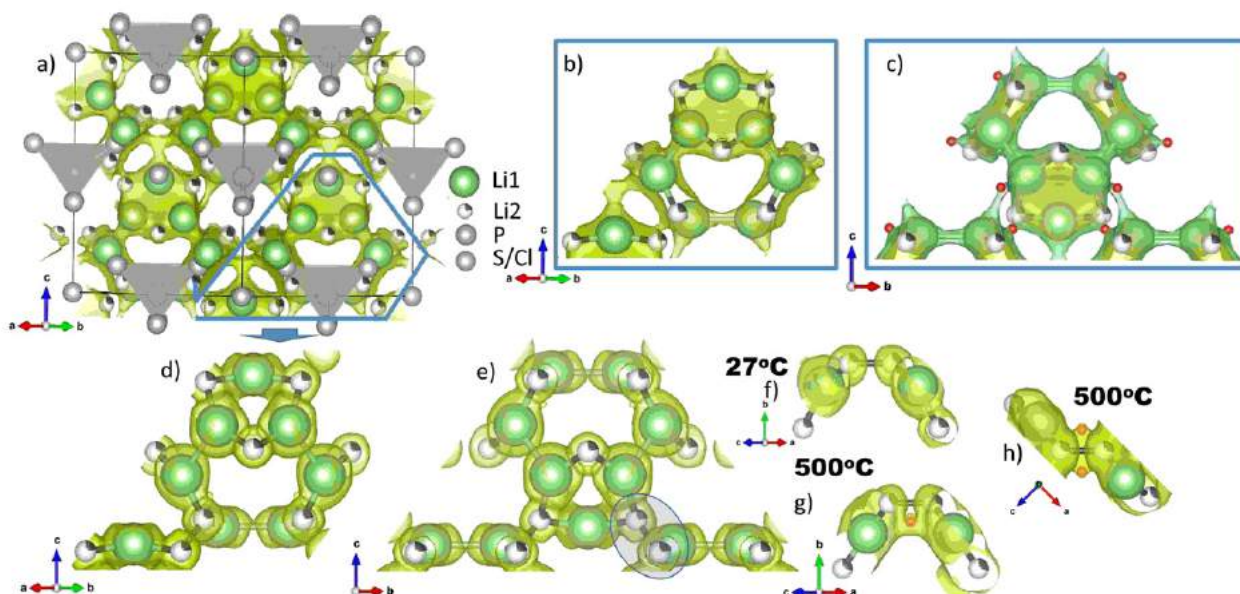


Fig. 1: Bond valence isosurfaces and atom locations in $\text{Li}_6\text{PS}_5\text{Cl}$ (a-c). Yellow/green isosurfaces correspond to $\Delta V=0.12$ and $\Delta V=0.1$ valence units, accordingly. Red spheres illustrate necks/intermediate sites which potentially support lithium diffusion. Selected regions of negative nuclear scattering density maps observed for $\text{Li}_6\text{PS}_5\text{Cl}$ at ambient temperature (d-f) and 500°C (g-h) by maximum entropy analysis. Isosurfaces in (d-h) were plotted using the equidensity level 0.013 $\text{fm}/\text{\AA}^3$.

D. Petz^{1,2}, M. J. Mühlbauer^{1,3}, V. Baran¹, O. Dolotko^{1,4}, M. Hofmann¹, R. Kostecki⁵, A. Senyshyn¹

¹Heinz Maier-Leibnitz Zentrum (MLZ), Technical University of Munich, Garching, Germany; ²Institute for Applied Materials (IAM), Karlsruhe Institute of Technology (KIT), Eggenstein-Leopoldshafen, Germany; ³Physics Department, Chair of Functional Materials, Technical University of Munich, Garching, Germany; ⁴U.S. DOE Ames Laboratory, Iowa State University, Ames, Iowa, USA; ⁵Energy Storage and Distributed Resources Division, Lawrence Berkeley National Laboratory, Berkeley, California, USA

Li-ion batteries became very popular energy storage systems in diverse daily life applications. This is mainly due to the high energy and power density along with their relatively fast charging rates. The loss of capacity with increasing cycle- and calendar- lifetime is a well-known drawback and is a subject to active research.

Cell disassembling for further *ex situ* or *post mortem* studies may cause irreversible changes in the cell state and its materials due to electrolyte evaporation, electrode oxidation etc. There is great interest in the non-destructive techniques capable to investigate these kind of isolated systems. Due to the high penetration depth, the high sensitivity to light elements and distinguishing between neighbouring elements, neutron diffraction has proven to be well suited for such kind of investigations.

Neutron diffraction can independently probe the lithiation state of the both positive and negative electrodes in a Li-ion cell. For example, in the anode the local lithium concentration x in Li_xC_6 can be unambiguously determined from the phase fractions of LiC_6 and LiC_{12} . Several years ago it has been found that at temperatures below 250 K the liquid electrolyte freezes and forms a long range order in frozen state, which can be detected and quantified with neutron diffraction. It offers the opportunity of quantifying and correla-

ting the lithium concentration in the graphite and the amount of electrolyte simultaneously.

The cell layout was studied non-destructively using X-ray CT (Fig. 1a), since cell opening is known to affect the lithium distribution in the graphite anode. Neutron diffraction studies were performed on instruments STRESS-SPEC and SPODI. At the position near the current lids and the center pin systematically lower lithium concentrations are observed. This, along with the aging-driven reduction in lithium inventory can be clearly observed by comparing the lithium concentration in fresh and aged cells (Fig. 1b) along with the heterogeneity of the cell degradation, where a clear gradient develops towards the cell bottom and cell top.

The experimentally observed electrolyte distribution (Fig. 1c) displays a well-resolved radial gradient towards the cell housing (outer region), which is present over the whole cell height. Extensive cell cycling results in a clear reduction of the electrolyte containment. The inhomogeneous degradation is here reflected in the development of a height gradient with systematically higher electrolyte concentration at the cell bottom associated with gravity.

[1] M. J. Mühlbauer et al., *Inhomogeneous distribution of lithium and electrolyte in aged Li-ion cylindrical cells*, *J. Power Sources* 475, 228690 (2020)

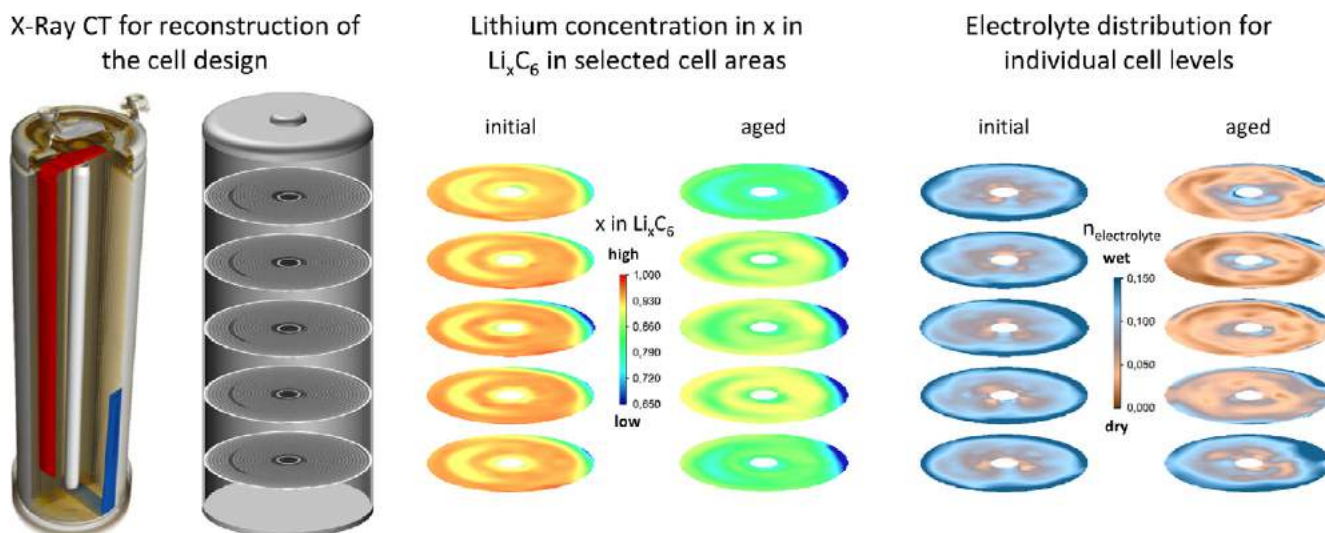


Fig. 1: Layout of stated cell (reconstructed from X-Ray CT) (a); Lithium concentration x in Li_xC_6 (b) and obtained electrolyte $n_{\text{electrolyte}}$ distribution (c) in a fresh and aged cylinder-type Li-ion batteries.

J. Zhu¹, M. Knapp^{1,2}, D. R. Sørensen³, M. Heere^{1,3}, M. S. D. Darma^{1,2}, A. Senyshyn³, H. Ehrenberg^{1,2}

¹Institute for Applied Materials (IAM), Karlsruhe Institute of Technology (KIT), Eggenstein-Leopoldshafen, Germany; ²Helmholtz Institute Ulm (HIU) Electrochemical Energy Storage, Ulm, Germany; ³Heinz Maier-Leibnitz Zentrum (MLZ), Technical University of Munich, Garching, Germany

18650-type cells with 2.5 Ah capacity were cycled at both 25°C and 0°C separately. At 25°C two charging protocols (constant current (CC) and constant current-constant voltage charge (CC-CV)) were used. The capacity results are shown in Fig. 1.

Collection of the neutron powder diffraction (NPD) data was carried out at the diffractometer SPODI for the beginning of life (BoL) cell, CY25-CC-400 (400 cycles), and CY25-CC-700 (700 cycles), respectively. The crystal structure parameters determined by *in situ* NPD are shown in Fig. 2. No new phases appear and no phases change for the cathode after the cell cycling. The (003) peaks of Li(NiCoAl)O₂ (NCA) and Li(NiCoMn)O₂ (NCM) are enlarged, as shown in Fig. 2b, indicating that the relative intensity of NCM reduces after the cell degradation, and slight structural changes can be observed from the peak shift. An increasing trend of the unit cell volume (Fig. 2d) can be observed in the course of cycling guided by the dashed lines, meaning that some increasing amount of lithium is still intercalated in the NCM/NCA structure. Comparing the (001) peak intensity of LiC₆ and (002) peak of LiC₁₂ for BoL and fatigue cells in Fig. 2c, it can be found that the weight fraction of the LiC₆ phase decreases whilst the amount of LiC₁₂ phase increases. From Fig. 2e, the quantitative evaluation of the BoL cell charged at 4.2 V reveals a weight ratio of LiC₆ to LiC₁₂ as approximately 11.0:1. Upon cycling, this ratio changes to 2.7:1 and to 1.1:1 for the CY25-CC-400 and CY25-CC-700

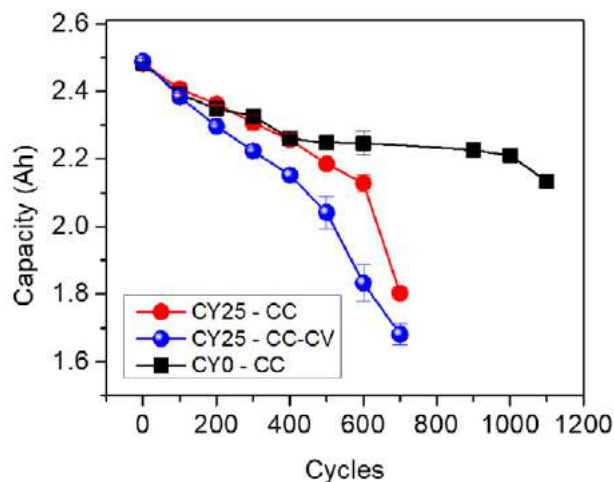


Fig. 1: Residual capacity of cells as a function of cycle number. Cycling with CC protocol at 25°C (CY25-CC); Cycling with CC-CV protocol at 25°C (CY25-CC-CV); Cycling with CC protocol at 0°C (CY0-CC)

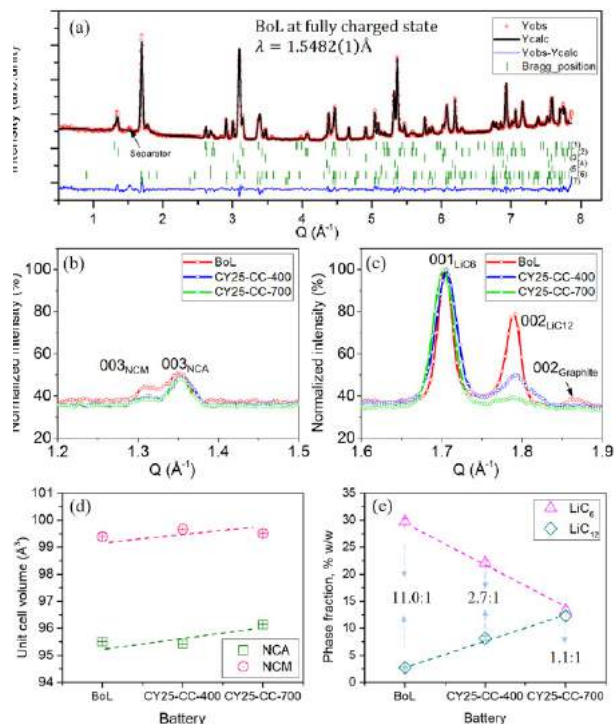


Fig. 2: *In situ* neutron powder diffraction results of the BoL cell and selected fatigued cells at fully charged state. (a) Neutron powder diffraction pattern for the BoL cell including the Rietveld refinement. (b) Selected range of neutron powder diffraction data focusing on the Bragg peak NCM (003) and NCA (003) phases. (c) Selected range for LiC₆ and LiC₁₂. (d) Calculated unit cell volumes. (e) Calculated phase weight ratios of LiC₆ and LiC₁₂.

cells, respectively. These changes in the phase fractions of intercalated phases correspond to a reduction of the active lithium into the graphite.

$$x \text{ in } \text{Li}_x\text{C}_6 = \frac{\text{Wt.\%LiC}_6 + \text{Wt.\%LiC}_{12}}{\frac{M_{\text{LiC}_6}}{\text{Wt.\%LiC}_6} + 2 \frac{M_{\text{LiC}_{12}}}{\text{Wt.\%LiC}_{12}}}$$

Summary: The lithium content x in Li_xC_6 is calculated by Equation (1). Wt.%LiC₆ is the LiC₆ weight fraction, Wt.%LiC₁₂ is the LiC₁₂ weight fraction, $M_{\text{LiC}_6} = 79.0052 \text{ g/mol}$, $M_{\text{LiC}_{12}} = 151.0694 \text{ g/mol}$. The quantitative recalculation of the lithium amount x inside the anode presents a reduction of 10% and 22% for CY25-CC-400 and CY25-CC-700 cells respectively, which shows good agreement with the results from other electrochemical techniques in [1].

[1] J. Zhu et al., *Investigation of lithium-ion battery degradation mechanisms by combining differential voltage analysis and alternating current impedance*, *J. Power Sources* 448, 227575 (2020)

G. J. Redhammer¹, M. Meven^{2,3}, S. Ganschow⁴, G. Tippelt¹, D. Rettenwander⁵

¹Department of Chemistry and Physics of Materials, Division of Materials Science and Mineralogy, University of Salzburg, Salzburg, Austria; ²Institute of Crystallography, RWTH Aachen University, Aachen, Germany; ³Jülich Centre for Neutron Science (JCNS) at MLZ, Forschungszentrum Jülich GmbH, Garching, Germany; ⁴Leibniz-Institut für Kristallzüchtung (IKZ), Berlin, Germany; ⁵Institute for Chemistry and Technology of Materials, Graz University of Technology, Graz, Austria

Modern and high-performance energy storage devices based on Li-ion battery technology require the selection of a safe electrolyte material. Cubic modifications of $\text{Li}_7\text{La}_3\text{Zr}_2\text{O}_{12}$, stabilised by doping with aliovalent cations, have been identified as being among the few promising candidates for such demanding purposes. Here, we studied a large single crystal of $\text{Li}_6\text{La}_3\text{ZrTaO}_{12}$ (LLZTO) – grown using the Czochralski method – by using neutron diffraction between 2.5 and 873 K. The data were collected at the HEiDi diffractometer down to d -values of 0.62 Å. Our goal was to fully characterise the Li-atom distribution, and possible Li ion mobility in this class of potential candidates for solid state electrolyte battery material [1].

Very accurate structural data for $\text{Li}_6\text{La}_3\text{ZrTaO}_{12}$ garnet-type material are obtained from the neutron diffraction analyses and can be indexed on the basis of the space group symmetry $la\bar{3}d$, revealing the generally assumed model of the garnet structure with La^{3+} on the 8-fold oxygen coordinated 24c site and $\text{Zr}^{4+}/\text{Ta}^{5+}$ on the 6-fold oxygen coordinated 16a site at any temperature investigated. Two strong nuclear densities appear within the dodecahedral – octahedral framework, corresponding to the two Li-positions. Li1 occupies the regular tetrahedrally coordinated 24d site at (3/8, 0, 1/4) of the garnet structure (normally occupied by Si^{4+} in silicate garnets), and Li2 resides at an interstitial site at the typical 96h position with coordinates $\sim (0.15, 0.17, 0.44)$. Both Li-atomic positions already show distinct anisotropic atomic displacement parameters at 2.5 K.

Detailed inspection of nuclear density data reveals some displacement of the tetrahedrally coordinated Li1 site from the 24d position to the more typical 96h position as depicted in Fig. 1. This displacement is small, but highly interesting as it may explain fast ion transport due to possible shorter jump distances. No indications are found to support Li occupation of a site other than 24d and 96h. Finally, and most importantly, from the high-resolution single crystal data it is

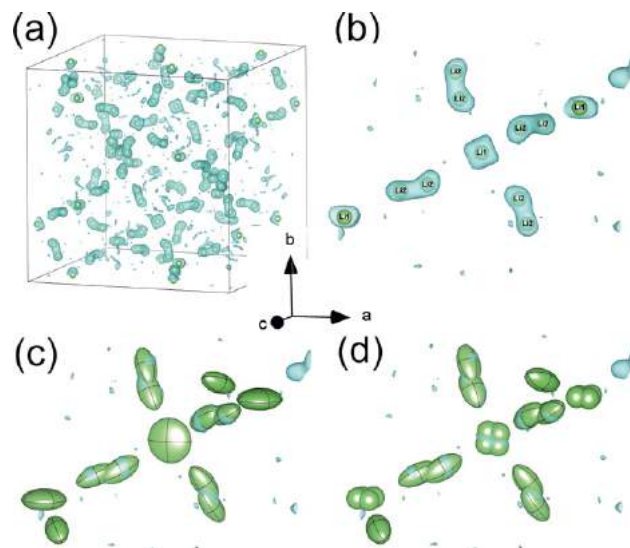


Fig. 1: Negative residual nuclear density (light blue) of LLZTO at 300 K, obtained from refining the framework La, Zr/Ta and O atom positions in the full unit cell (a) and a small section of the cell (b) with the refined Li-position of the “standard” model depicted as small green spheres. (c) the model with anisotropic refinement of Li1 at 24d with atomic displacement parameters, drawn at the 95% level, and (d) the model with Li1 shifted to a 96h position and isotropic refinement.

found that, although the anisotropic atomic displacement increases distinctly with temperature, the site occupation of Li1 and Li2 sites remains almost constant. Using powder diffraction data, this is not fully resolvable due to limited resolution and the high correlation of occupation numbers and atomic displacement parameters. In other words, there is no evident migration or change in average site occupation with temperature change. Since no change in the Li-ion distribution and no additional sites are occupied by increasing temperature, we conclude that the predominating diffusion pathways in LLZTO remain along the 24d – 96h sites in the $\text{Li}_6\text{La}_3\text{ZrTaO}_{12}$ garnet framework.

[1] G. J. Redhammer et al., *Single-crystal neutron and X-ray diffraction study of garnet-type solid-state electrolyte $\text{Li}_6\text{La}_3\text{ZrTaO}_{12}$: an in-situ temperature dependence investigation ($2.5 \text{ K} \leq T \leq 873 \text{ K}$)*, *Acta Cryst. B* 77, 123 (2021)

A. Kuhn¹, M. R. Plews², J. C. Perez-Flores³, F. Fauth⁴, M. Hoelzel⁵, J. Cabana², F. Garcia-Alvarado¹¹Departamento de Química y Bioquímica, Facultad de Farmacia, Universidad San Pablo-CEU, CEU Universities, Madrid, Spain; ²Department of Chemistry, University of Illinois at Chicago, Chicago USA; ³Renewable Energy Research Institute, University of Castilla-La Mancha, Albacete, Spain; ⁴Experiments Division CELLS - ALBA, Barcelona, Spain; ⁵Heinz Maier-Leibnitz Zentrum (MLZ), Technical University of Munich, Garching, Germany

Metal oxyfluorides are currently attracting a lot of attention for next-generation rechargeable batteries on account of their high theoretical capacity. In this work, VO₂F has been analysed in depth by means of neutron diffraction and *in operando* synchrotron X-ray diffraction to accurately describe the structural changes it undergoes upon lithium insertion. Redox changes were evaluated with X-ray absorption spectroscopy (XAS).

Commercial and technological demands are calling for energy storage devices to power lighter, smaller, cheaper, and safer applications. Lithium-ion batteries are employed to satisfy such requirements, but most of them use Ni- and Co-based oxide cathodes related to low specific energy, high toxicity and costs. Their progress towards highly demanding portable and stationary devices, plug-in hybrid and pure-electric vehicles will be dependent on the development of new electrode materials. Transition-metal oxyfluorides, with a strong ionicity of the M-F bond, could offer a higher average working potential in comparison to “pure” oxide compounds. An interesting oxyfluoride is VO₂F with a high specific theoretical capacity (263 mAh g⁻¹ for 1 Li⁺/f.u.) in the 3.9 - 2.2 V vs. Li⁺/Li voltage range.

In operando synchrotron XRD experiments reveal subtle and continuous changes of lattice parameters upon a full discharge-charge cycle (Fig. 1a), characteristic of a solid solution mechanism in the 0 ≤ x ≤ 1 compositional range. The small change in volume would explain the excellent cyclability in this single-phase domain.

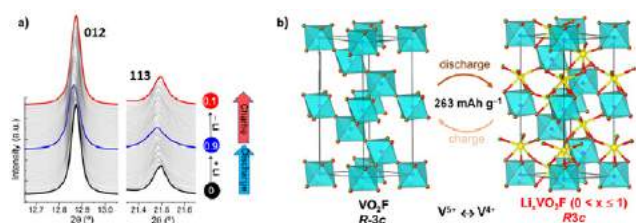


Fig. 1: a) Selected angular domain for a full discharge-charge cycle using *in operando* synchrotron X-ray diffraction. b) Crystal structures of VO₂F (left) and lithiated VO₂F (right). V-O/F octahedra (cyan); Li (yellow spheres); O/F (red spheres). Reprinted with permission from Inorg. Chem. 2020, 59, 10048–10058. Copyright (2020) American Chemical Society.

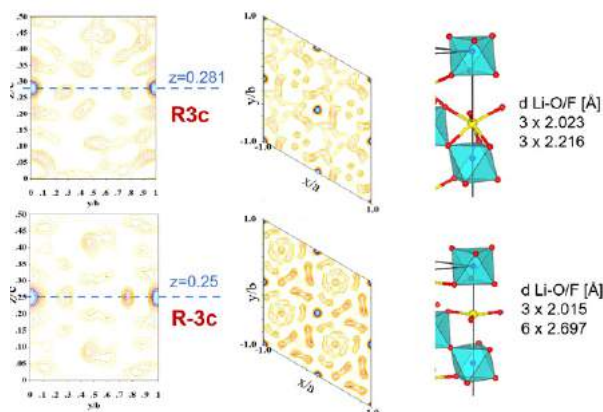


Fig. 2: Difference Fourier neutron-density maps for LiVO₂F in space group *R-3c* (bottom) and space group *R3c* (top) and corresponding coordinations for lithium with O/F anions. Reprinted with permission from Inorg. Chem. 2020, 59, 10048–10058. Copyright (2020) American Chemical Society.

The lithium site in lithiated VO₂F was determined from difference Fourier neutron density maps (Fig. 2) using the high-resolution powder ND data collected on SPODI. A closer examination reveals a continuous transition of the initially cubic-like close packing of anions in VO₂F, space group *R-3c*, toward hexagonal close packing in LiVO₂F, but with space group *R3c*. The lower symmetry space group *R-3c* allows for a 6-fold octahedral coordination for lithium (Fig. 1b) with reasonable Li-O/F bond lengths in the range 2.023 – 2.216 Å (Fig. 2) and, therefore, better accommodates the preferred crystal chemistry of the alkali metal in the structure.

Lithium insertion in VO₂F not only produces a reduction of V⁵⁺ to V⁴⁺, but is also accompanied by a change in covalent interactions with both O²⁻ and F⁻ anions as deduced from X-ray absorption spectroscopy (XAS). The clear evidence of the participation of F challenges existing assumptions that its high electronegativity renders this anion largely a spectator in the redox reaction.

[1] A. Kuhn et al., Redox Chemistry and Reversible Structural Changes in Rhombohedral VO₂F Cathode during Li Intercalation, Inorg. Chem. 59(14), 10048 (2020)

D. R. Sørensen^{1,2}, M. Heere^{2,3}, J. Zhu^{3,4}, M. S. D. Darma^{3,5}, S. M. Zimnik^{2,3}, M. J. Mühlbauer^{2,3}, L. Mereacre³, V. Baran², A. Senyshyn², M. Knapp³, H. Ehrenberg³

¹Department of Physics, Chemistry and Pharmacy, University of Southern Denmark, Odense, Denmark; ²Heinz Maier-Leibnitz Zentrum (MLZ), Technical University of Munich, Garching, Germany; ³Institute for Applied Materials (IAM), Karlsruhe Institute of Technology (KIT), Eggenstein-Leopoldshafen, Germany; ⁴Clean Energy Automotive Engineering Center, School of Automotive Engineering, Tongji University, Shanghai, China; ⁵Helmholtz Institute Ulm (HIU) Electrochemical Energy Storage, Ulm, Germany

Li-ion batteries are expected to play a major role in the transition to an electrified transport sector. In addition to energy density and cost, the lifetime of the battery cells is of vital importance if they are to compete with fossil fuel-based technologies. The capacity fatigue mechanisms in modern Li-ion battery cells are complex and depend heavily on the conditions of use, which necessitates a wide variety of investigative methods to gain a complete picture. Here, we use in-situ neutron diffraction on commercial Li-ion batteries cycled up to 3000 times at different temperatures to detect any long-term changes in the electrodes.

Two commercial brands of 18650 cylindrical battery cells were cycled up to 3000 times at different temperatures ($\frac{1}{2}C$ charge, $1C$ discharge at 25, 35 or 45°C) and the discharge capacity monitored at each cycle (Fig. 1a). Higher temperatures were seen to have a beneficial impact on the capacity retention for both brands. At specific cycle numbers, the batteries were disconnected, and neutron diffractograms recorded at SPODI, MLZ (Fig. 1b).

For each solid component in the cell, its diffraction signal could be identified and tracked as a function of

cycle number. Using multiphase Rietveld refinement, any changes in the components can be investigated. For the cathodes ($\text{Li}(\text{Ni}_{0.83}\text{Mn}_{0.07}\text{Co}_{0.11})\text{O}_2$ (NMC) for MJ1 and $\text{LiNi}_{0.86}\text{Co}_{0.11}\text{Al}_{0.03}\text{O}_2$ (NCA) for 35E), the lithium occupancy in the fully discharged state was seen to decrease steadily with cycle number (Fig. 1c). Importantly, no degradation of the cathodes to other phases was detected. Likewise, the Rietveld refinement of the graphite anode in the fully charged state showed decreasing lithiation, which could be linked to the decreasing capacity (Fig. 1d). This was done by comparing the two lithiated graphite phases LiC_{12} and LiC_6 , see Fig. 1b. As with the cathode, no decomposition phases, and no dislodged particles with different lithiation levels were detected. These results lead us to conclude that the main fatigue mechanisms for these cells is the slow degradation of the liquid electrolyte (not detectable using diffraction) over many cycles, which leads to lower and lower lithiation of the electrodes.

[1] D. R. Sørensen et al., *Fatigue in High-Energy Commercial Li Batteries while Cycling at Standard Conditions: An In Situ Neutron Powder Diffraction Study*, *ACS Appl. Energy Mater.* 3, 6611 (2020)

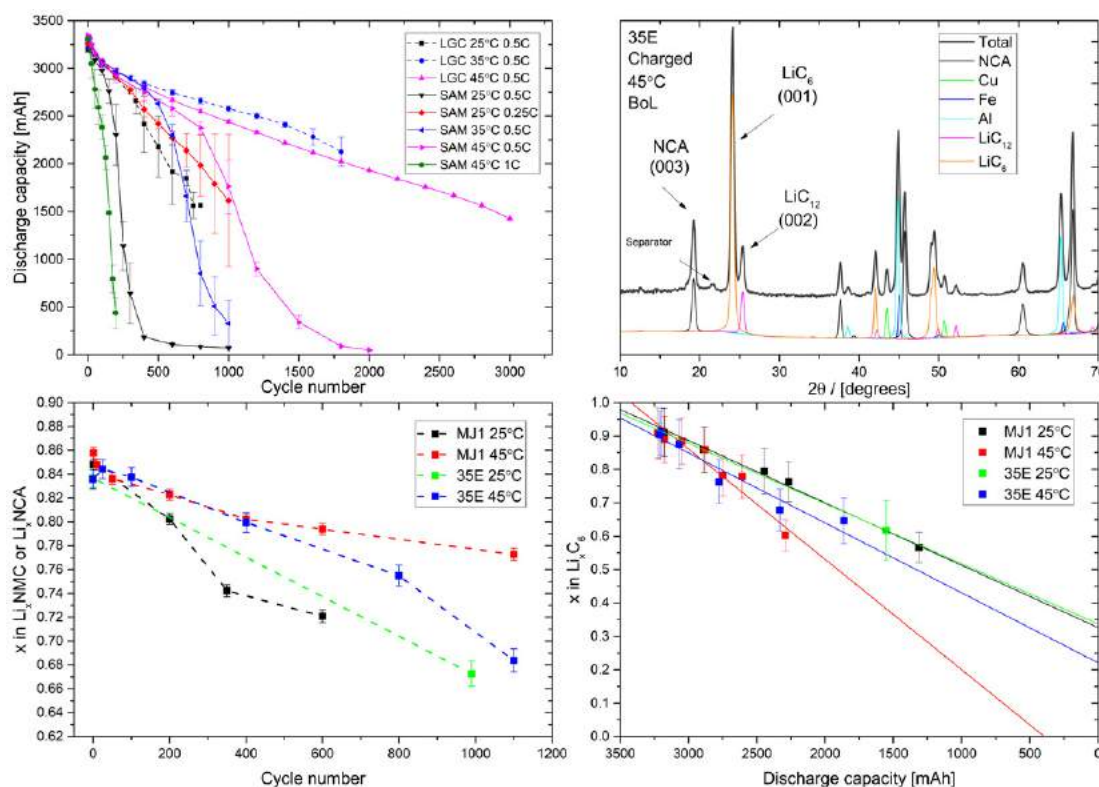


Fig. 1: a) Discharge capacity as a function of cycle number and temperature. b) An example of an in-situ powder neutron diffractogram; a fresh cell in the fully charged state. c) Lithium content in the cathode as a function of cycle number and temperature. d) Lithium content in the anode as a function of discharge capacity.

V. Hutanu¹, H. Deng¹, S. Ran^{2,3}, W. Fuhrman³, H. Thoma⁴, N. Butch^{2,3}

¹Institute of Crystallography, RWTH Aachen University and Jülich Centre for Neutron Science (JCNS) at MLZ, Forschungszentrum Jülich GmbH, Garching, Germany; ²NIST Center for Neutron Research, National Institute of Standards and Technology, Gaithersburg, USA; ³Center for Nanophysics and Advanced Materials, Department of Physics, University of Maryland, College Park, USA; ⁴Jülich Centre for Neutron Science (JCNS) at MLZ, Forschungszentrum Jülich GmbH, Garching, Germany

Recently, unconventional spin-triplet superconductivity has been reported in UTe_2 below 1.6 K. It was proposed that this belongs to the family of uranium based unconventional ferromagnetic (FM) superconductors as a paramagnetic end-member of this series, where spin fluctuations without an ordered magnetic moment play a major role in Cooper pairing. Moreover, observed superconductivity seems to survive the application of very strong magnetic fields, contrary to any intuitive expectation, and even exhibits a separate re-entrant superconducting phase between 45 T and 60 T. The structural parameters of UTe_2 at low temperature (LT) are an important prerequisite for any further studies as well as an understanding of the intriguing phenomenon of FM superconductivity.

Single-crystal neutron diffraction was performed on the diffractometer POLI at the MLZ. A short wavelength of 0.9 Å was employed in order to reduce the potential parasitic effects of absorption and extinction. A total number of 298 properly centered Bragg reflections satisfying the criterion $I > 10\sigma(I)$ were used for the refinement. By using SG *Immm* and averaging the symmetry equivalent peaks, the precise structural parameters of UTe_2 at 2.7 K were refined. A perspective view of the UTe_2 crystal structure is shown in Fig. 1. Our single crystal diffraction results show no evidence for any symmetry lowering at LT compared to the room temperature structure.

The atomic coordinates $z(U)$, $z(Te(1))$ and $y(Te(2))$ at LT were compared with those obtained from single crystal X-ray diffraction in the temperature range 573-118 K. The linear extrapolation of the large thermal evolution region down to zero temperature reproduces reasonably well (within one - two sigma error bars) our results for 2.7 K (Fig. 2).

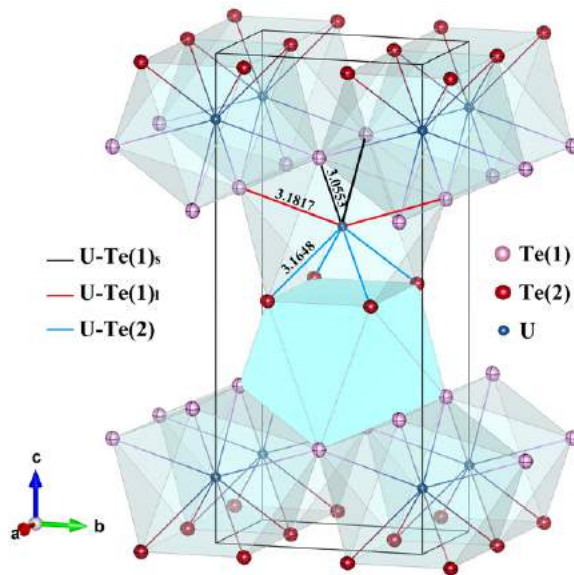


Fig. 1: The first coordination-sphere polyhedron of U (cation) by neighbouring Te (anions) in UTe_2 with bond lengths at 2.7 K.

This confirms the trends observed at higher temperatures, of strong decreasing $z(U)$ and weak decreasing $y(Te(2))$ with decreasing temperature, in contrast to the increasing $z(Te(1))$ also found for temperatures below 100 K.

Our data illustrate that there is no static magnetic order in UTe_2 in the normal state, which makes this superconductor qualitatively different from FM URhGe, UCoGe, and UGe₂ despite the similar anisotropy in superconducting upper critical fields and certain crystal structure similarities. We also support the picture of UTe_2 as a quantum critical FM.

[1] V. Hutanu et al., Low-temperature crystal structure of the unconventional spin-triplet superconductor UTe_2 from single-crystal neutron diffraction, *Acta Cryst. B* 76, 137 (2020)

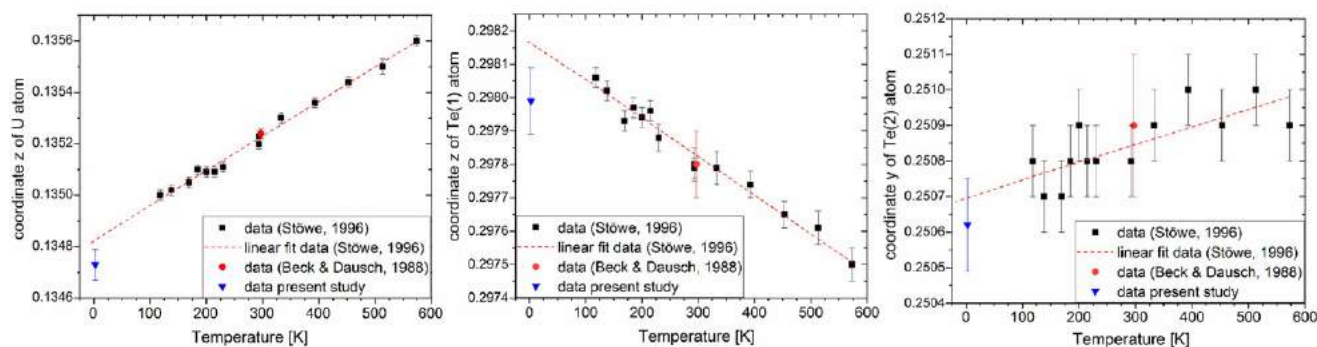


Fig. 2: Comparison of general atomic coordinates in UTe_2 refined in SG *Immm* at 2.7 K to data from literature at higher temperatures (K. Stöwe, *J. Solid State Chem.* 127, 202 (1996)).

F. Zhu^{1,2}, X. Wang¹, M. Meven^{1,3}, J. Song^{1,4}, T. Müller¹, C. Yi⁵, W. Ji^{1,6}, Y. Shi⁵, J. Ma², K. Schmalzl⁷, W. F. Schmidt⁷, Y. Su¹, T. Brückel^{1,6}

¹Jülich Centre for Neutron Science (JCNS) at MLZ, Forschungszentrum Jülich GmbH, Garching, Germany; ²Department of Physics and Astronomy, Shanghai Jiao Tong University, Shanghai, China; ³Institute of Crystallography, RWTH Aachen University, Aachen, Germany; ⁴Hefei National Laboratory for Physical Sciences at Microscale, University of Science and Technology of China, Hefei, Anhui, China; ⁵Institute of Physics and Beijing National Laboratory for Condensed Matter Physics, Chinese Academy of Sciences, Beijing, China; ⁶Peter Grünberg Institute PGI, JARA-FIT, Forschungszentrum Jülich, Jülich, Germany; ⁷Jülich Centre for Neutron Science (JCNS) at ILL, Grenoble, France

In recently emerging correlated topological materials, such as magnetic Dirac/Weyl semimetals, additional tunabilities of their transport and magnetic properties may be achieved by utilising a possible interaction between the exotic relativistic fermions and magnetic degree of freedom. The two-dimensional antiferromagnetic (AFM) Dirac semimetal EuMnBi_2 was proposed as an ideal candidate to test the potential coupling between multiple magnetic sublattices and Dirac fermions. We reported a comprehensive study of the AFM structures of the Eu and Mn magnetic sublattices as well as the interplay between Eu and Mn magnetism in this compound by using both polarised and nonpolarised single-crystal neutron diffraction.

From the magnetic susceptibility, specific heat capacity measurements, and the temperature dependence of magnetic diffractions, the AFM ordering temperature of the Eu and Mn sublattices are determined as 22 and 337 K, respectively. At DNS, we performed polarised neutron dif-

fraction experiments on single crystal EuMnBi_2 which were grown by the flux method, and we found that the magnetic moments of both Eu and Mn ions are oriented along the crystallographic c axis. Interestingly, the magnetic propagation vectors of Eu and Mn magnetic sublattices are distinct (e.g., $(0,0,1)$ for Eu; $(0,0,0)$ for Mn). To figure out the detailed magnetic structures for Eu and Mn ions, we collected more than 1500 nuclear and magnetic reflections at both 3 K and 300 K at HEIDI. With proper neutron absorption correction and symmetry analysis, the magnetic structures for Eu and Mn sublattices can be nicely refined by using the magnetic space groups $P4/nnc$ and $I4'/m'm'm$ separately. Most of all the integrated intensities I_{obs} have a good linear behaviour with the calculated intensities I_{calc} . The final refined magnetic structures and magnetic moment size are shown in Fig. 1 (a) and (b).

In addition, we further investigated the reorientation of the Eu moments in an applied magnetic field along the c axis at D23, and a spin-flop (SF) phase transition was confirmed to take place at a critical field of $H_c \sim 5.3$ T. By utilising the critical values fitted from the field dependence of the integrated intensities, as shown in Fig. 1 (c), one can probe the SF transition quantitatively by defining the spin Hamiltonian (XXZ model) and subsequently extracting the AFM exchange and magnetic anisotropy parameters ($J = 0.81$ meV, $K_u = 0.18$ meV, $K_e = -0.11$ meV). Furthermore, the temperature dependence of the selected magnetic reflection $(1,0,1)$ was also monitored during the cooling process, as shown in Fig. 1 (d), and a sudden enhancement of intensity can be observed near 22 K for both cases with and without applied field, i.e., exactly at the magnetic phase transition of Eu. It suggests a strong interplay between the two magnetic sublattices, and the coupling of Eu and Mn magnetism could be affected by the applied field in this system.

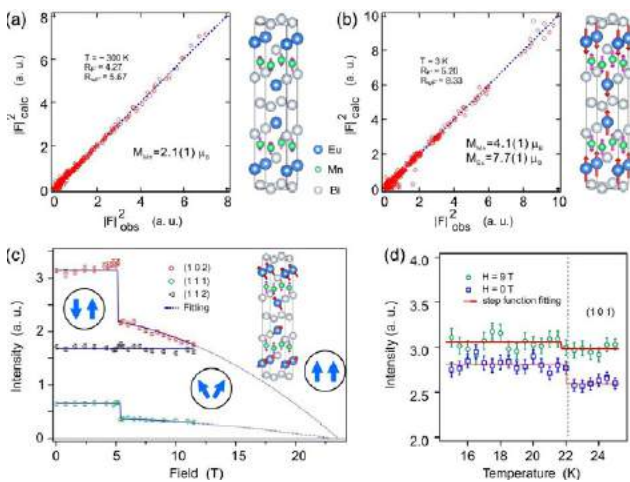


Fig. 1: Integrated intensities of the Bragg reflections collected at 300 K (a) and 3 K (b) plotted against the calculated values. (c) Field dependence of the integrated intensities of the selected nuclear and magnetic (contributed by Eu) reflections taken at 1.5 K. (d) Temperature dependence of the magnetic reflection $(1,0,1)$ with $H = 0$ and 9 T.

[1] F. Zhu et al, *Magnetic structures, spin-flop transition, and coupling of Eu and Mn magnetism in the Dirac semimetal EuMnBi_2* , *Phys. Rev. Research* 2, 043100 (2020)

N. van Well¹, M. Skoulatos^{2,3}, R. Georgii^{2,3}¹Department of Earth and Environmental Sciences, Crystallography Section, Ludwig Maximilian University of Munich, Munich, Germany; ²Heinz Maier-Leibnitz Zentrum, Technical University of Munich, Garching, Germany; ³Physics Department E21, Technical University of Munich, Garching, Germany

The triangular antiferromagnetic $\text{Cs}_2\text{CuCl}_{4-x}\text{Br}_x$ mixed system shows a rich magnetic phase diagram [1]. Depending on the Br concentration of the orthorhombic mixed system $\text{Cs}_2\text{CuCl}_{4-x}\text{Br}_x$, its diagram can be split into four regimes, which are characterised by different exchange coupling mechanisms. Regime I with $0 < x \leq 1.5$ Br and regime IV with $3.2 < x \leq 4$ Br, show a magnetic order. But regime II ($1.5 < x \leq 2$) and regime III ($2 < x \leq 3.2$) show no magnetic order. The investigated composition ($x = 2.2$), allocated in regime III, presents no magnetic order in the directions $(0\ 1\ 0)$, $(0\ 1\ 2)$ and $(0\ 1\ -2)$. The behaviour of the exchange parameter, obtained from a DFT calculation, was used to choose the Heisenberg model (HM) on an anisotropic triangular lattice (ATL) and square lattice (SL). HM yields ATL in the case of $J > J'$, and SL in the case of $J < J'$. This differentiation is necessary to describe the exchange interaction and for the distinction between different regimes. Fig. 1a shows the crystal structure for $x = 2$. The Cu^{2+} ions form chains (J), coupled in a zig-zag manner (J') in the bc -plane. The neighbouring layers are coupled by an exchange (J'') in the a -direction.

Inelastic neutron scattering experiments were performed at the instrument MIRA at the MLZ in the cold-three-axes spectrometer configuration for the compound from regime III ($2 < x \leq 3.2$) with $x = 2.2$. The energy scans were executed along $(0\ k\ 0)$ at the base temperature of 50 mK and show dynamical correlations. Fig. 1b represents raw energy scans (without subtraction of the background) along $(0\ k\ 0)$. The inset in Fig. 1b displays the upper boundary of the continuum scattering at 1.5 meV. This suggests that the Br concentration in $\text{Cs}_2\text{CuCl}_{1.8}\text{Br}_{2.2}$ shifts the upper boundary of the continuum scattering as compared to Cs_2CuCl_4 , where the upper boundary measured above and below T_N was found at 1 meV.

The results from the scans along $(0\ 1/2\ -l)$ in Fig. 1c display similar characteristics to those from Cs_2CuCl_4 . In general, the spin liquid behaviour is attributed to a quasi-1D and rather seldom to a 2D behaviour with a two-spinon continua. At the present time, our experimental data cannot be fully described by the quasi-1D description. Further investigations of this spin liquid phase are needed for a full description of the dynamical correlations found, dominated by highly dispersive scattering continua.

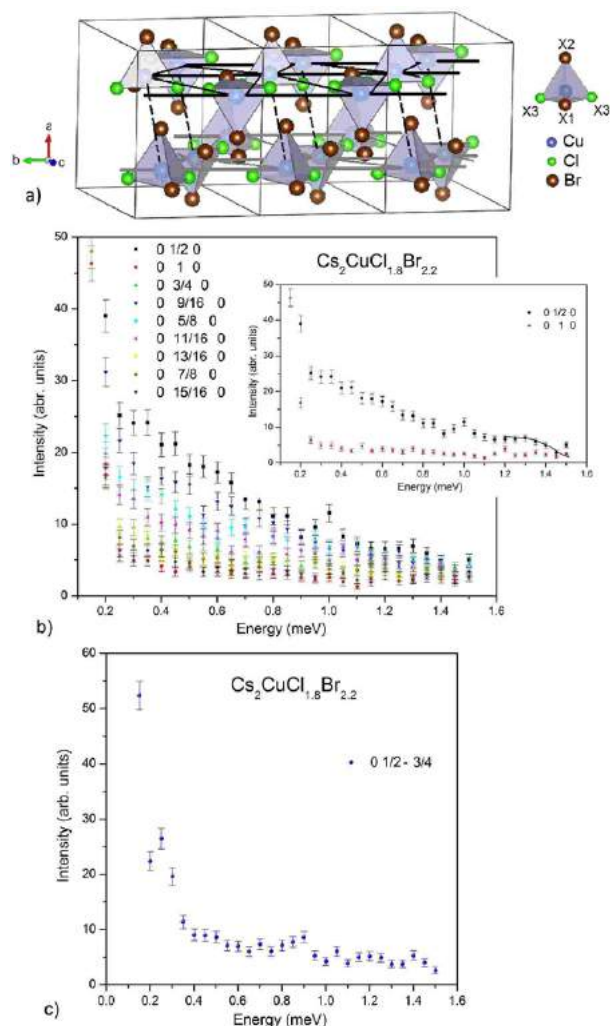


Fig. 1: a) Left: crystal structure for $x = 2$ with the $[\text{CuCl}_2\text{Br}_2]$ tetrahedra for three neighbouring unit cells in the ab -plane. Right: $[\text{Cl}_2\text{Br}_2]$ tetrahedra with Cl and Br having different preferred occupations of the different X_i crystallographic sites. For $x = 2$, the crystallographic position X_2 and X_1 is fully occupied by Br. Cs atoms are not shown for clarity. Energy scans: b) along the $(0\ k\ 0)$ direction for $\text{Cs}_2\text{CuCl}_{1.8}\text{Br}_{2.2}$; inset shows only two energy scans with a typical upper boundary of the continuum scattering (solid line as a guide to the eye), c) along the $(0\ 1/2\ -3/4)$ direction

[1] N. van Well et al., *Magnetic-Field-Controlled Quantum Critical Points in the Triangular Antiferromagnetic $\text{Cs}_2\text{CuCl}_{4-x}\text{Br}_x$ Mixed System*, *Ann. Phys.* 532, 2000147 (2020)

A. Grzechnik¹, M. Meven^{1,2}, K. Friese³¹Institute of Crystallography, RWTH Aachen University, Aachen, Germany; ²Jülich Centre for Neutron Science (JCNS) at MLZ, Forschungszentrum Jülich GmbH, Garching, Germany; ³JCNS-2, Peter Grünberg Institute (PGI), ⁴Scattering Methods, Forschungszentrum Jülich GmbH, Jülich, Germany

Single-crystal X-ray diffraction in a diamond anvil cell (DAC) is routinely performed on very small samples ($< 10^{-7} \text{ mm}^3$) to megabar pressures. However, there are hardly any single-crystal neutron diffraction studies in DACs that would present complete structural refinements. The reason is that, even at the most advanced neutron facilities, it is difficult to study crystals with volumes below 1 mm^3 since the highest neutron fluxes are several orders of magnitude smaller than the photon fluxes at synchrotron sources. The requirement for large samples hinders a joint use of X-ray and neutron single-crystal diffraction on compression. The combination of both techniques is highly advantageous as X-ray diffraction fails to provide precise information on, for instance, magnetic order or hydrogen bonding.

Recently, a new DAC was developed [1] suitable for both neutron and X-ray single-crystal diffraction (Fig. 1). It can be operated remotely using a membrane filled with the He gas and is useful for monitoring selected reflections with changing pressure. The outer dimensions of the DAC and of the membrane cup allow for the same crystal to be studied under the same conditions on laboratory X-ray and synchrotron diffractometers, as well as on neutron beamlines.

Single-crystal diffraction studies were carried out on the same crystal of MnFe_4Si_3 ($0.4 \times 0.45 \times 0.6 \text{ mm}^3$) under identical conditions of about 1 GPa at room temperature on

HEiDi at the MLZ and on the synchrotron beamline P24 at PETRAIII in Hamburg. The neutron and synchrotron diffraction data obtained were of very high quality and could be jointly refined. It was not possible to refine the Mn and Fe occupancies reliably using only the synchrotron data, due to the limited contrast of these neighbouring elements in X-ray diffraction. To distinguish these two elements, the information from the neutron data was clearly needed. An additional test with only the 10 strongest neutron reflections in the joint refinement showed that the occupancy factors are still correct. This implies that to resolve issues regarding, for instance, magnetic ordering or the positions of hydrogen bonds, a comparatively small number of reflections measured using neutrons would also be sufficient if they were combined with X-ray data. To sum up, the data collection and processing procedures as well as a joint structural refinement of the high-pressure synchrotron and neutron single-crystal data were performed for the very first time.

This work was supported by the projects 05K16PA3 and 05K19PA2 from the Federal Ministry of Education and Research (BMBF).

[1] A. Grzechnik et al., *Combined X-ray and neutron single-crystal diffraction in diamond anvil cells*, *J. Appl. Cryst.* **53**, 9 (2020)

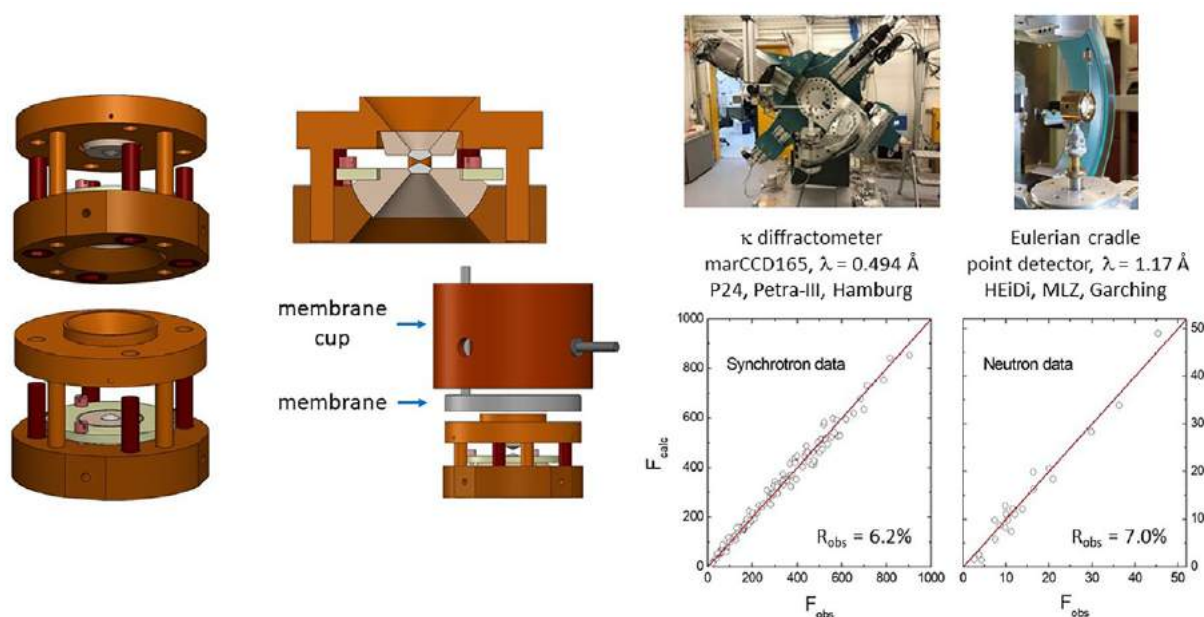


Fig. 1: Schematic drawing of the cell used at PETRAIII and the MLZ. The diagrams show the $F_{\text{obs}} - F_{\text{calc}}$ plots for the synchrotron and neutron data from the joint refinement.

Fast neutron imaging is a subfield of radiography with the potential to image large-scale objects such as plane turbines or fossils embedded in rocks due to the penetrative power of these high-energy neutrons (> 1 MeV). Fast neutrons are detected indirectly by the generation and detection of recoil protons in the detector screen, with traditional detectors utilising microscale scintillating phosphors embedded in plastics. However, widespread application of fast neutron imaging is inhibited by low detector efficiencies, compounded by drawbacks from the ZnS:Cu-based commercial screens including minutes-long afterglows and light scattering at the plastic-phosphor interface. Separately, the development of colloidal semiconductor nanocrystals (NCs) with emission quantum yields near unity has led to their successful incorporation in commercial displays and other lighting technologies. This work, conducted at the NECTAR beamline for fast neutron imaging, capitalises on these advances by utilising colloidal NCs as next-generation transparent scintillators for use in fast neutron imaging (Fig. 1).

Colloidal NCs exhibit high luminescent efficiencies and are transparently dissolved in solvents, providing the two-component system of standard detectors while eliminating key drawbacks of these screens. Here, the proton-rich solvent provides the scattering of neutrons to generate recoil protons, which then ionise charge carriers and excite scintillation in the efficiently emissive NCs (Fig. 2). This approach eliminates the plastic-phosphor interface, while the nano-scale confinement leads to enhanced recombination rates for short decay times.

Fast neutron imaging with colloidal NCs

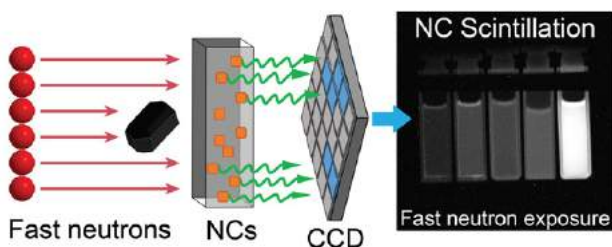


Fig. 1: Schematic of fast neutron detection utilising semiconductor nanocrystal scintillators.

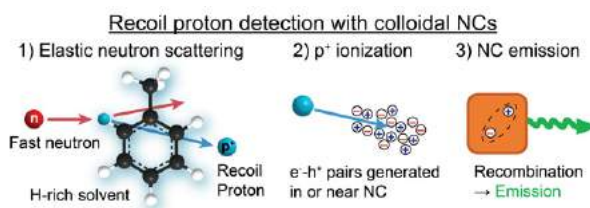


Fig. 2: Recoil proton detection in colloidal NCs for fast neutron detection.

We were able to realise this concept, demonstrating that a variety of halide and chalcogenide-based NCs all scintillate under fast neutron exposure, with perovskite FAPbBr₃ NCs showing a light output 19.3% of the commercial ZnS:Cu reference (Fig. 3a). Importantly, these NCs exhibited significantly lower gamma-ray sensitivity and no long-lived afterglows that impact their performance, confirming their expected advantages over the standard phosphor.

Spatial resolutions were estimated using metal blocks with sharp edges placed in the beam path, which were clearly resolved by the scintillating NCs (Fig. 3b). We also extracted several design principles through concentration and thickness-dependent measurements, indicating that higher concentrations and lower self-absorption are needed to advance beyond the current state-of-the-art detectors. These insights will guide future work towards NC-based fast neutron scintillators that offer high light yield alongside excellent spatial resolution, enabling the widespread use of fast neutron imaging.

[1] K. M. McCall *et al.*, *Fast Neutron Imaging with Semiconductor Nanocrystal Scintillators*, *ACS Nano* 14, 14686 (2020)

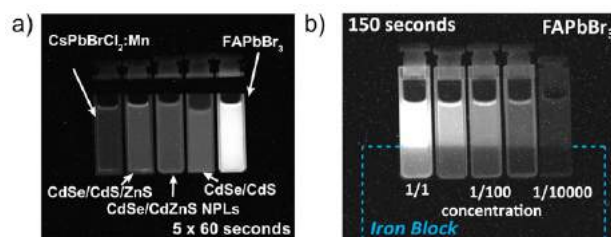


Fig. 3: Radiographs of NC scintillators under fast neutron irradiation: a) 5 different NCs with an unblocked beam (5 60 s exposures), and b) FAPbBr₃ NCs of varying concentration with an iron block in the beam to highlight the spatial resolution (150 s exposure).

W. Chuirazzi¹, A. Craft¹, B. Schillinger², S. Cool³, A. Tengattini^{4,5}

¹Advanced Post-Irradiation Examination Department, Idaho National Laboratory, Idaho Falls, USA; ²Heinz Maier-Leibnitz Zentrum (MLZ) and Physics Department, Technical University of Munich, Garching, Germany; ³DMI/Reading Imaging, Reading, USA; ⁴French National Centre for Scientific Research (CNRS), Université Grenoble Alpes, Grenoble, France; ⁵Institut Laue-Langevin (ILL), Grenoble, France

In digital neutron imaging, the neutron scintillator screen is a limiting factor of spatial resolution and neutron capture efficiency and must be improved to enhance the capabilities of digital neutron imaging systems. Commonly used neutron scintillators are based on ${}^6\text{LiF}$ and gadolinium oxy-sulfide neutron converters. This work explored boron-based neutron scintillators because ${}^{10}\text{B}$ has a neutron absorption cross-section four times greater than ${}^6\text{Li}$, less energetic daughter products than Gd and ${}^6\text{Li}$, and lower X-ray sensitivity than Gd. These factors all suggest that, although borated neutron scintillators may not produce as much light as ${}^6\text{Li}$ -based screens, they may offer improved neutron statistics and spatial resolution.

A parametric study was conducted at the ANTARES beamline to determine the effects of various boron neutron converters, scintillator and converter particle sizes, converter-to-scintillator mix ratio, substrate materials, and sensor construction on image quality. A novel approach for testing neutron scintillators that provides a simple and efficient way to measure relative light yield and detection efficiency over a range of scintillator thicknesses using a single scintillator screen and only a few radiographs was also developed. Two methods for correlating the screen thickness to the measured data were implemented and compared [1]. The best performing boron-based scintillator screens demonstrated an improvement in neutron detection efficiency when compared with a common ${}^6\text{LiF}/\text{ZnS}$ scintillator, with a 125% increase in thermal neutron detection efficiency and 67% increase in epithermal neutron detection efficiency [2]. The spatial resolution of high-resolution borated scintillators was measured, and the neutron tomography of a test object was successfully performed using some of the boron-based screens that exhibited the highest spatial resolution. An image of a mechanical watch acquired with a high-resolution boron-based neutron scintillator is displayed in Fig. 1.



Fig. 1: A reconstructed neutron tomography of a mechanical watch acquired with a prototype high resolution boron-based neutron scintillator screen.

The improved detection efficiency of boron-based scintillator screens compared to the common ${}^6\text{LiF}/\text{ZnS}$ scintillator allows for better image quality when taken with the same exposure time. Conversely, an image with the quality of that taken with the common ${}^6\text{LiF}/\text{ZnS}$ scintillator can be obtained by the boron-based scintillator in a quicker time, increasing the throughput of neutron imaging experiments. The screens developed here represent more efficient operations at ANTARES and neutron imaging facilities worldwide by improving the data quality through higher neutron detection efficiency and / or accelerating measurement times for users.

[1] W. Chuirazzi, A. E. Craft, *Measuring Thickness-Dependent Relative Light Yield and Detection Efficiency of Scintillator Screens*, *J. Imaging* 6(7), 56 (2020)

[2] W. Chuirazzi et al., *Boron-Based Neutron Scintillator Screens for Neutron Imaging*, *J. Imaging* 6(11), 124 (2020)

D. Awad¹, S. Younes¹, M. Glemser¹, F. M. Wagner², G. Schenk^{3,4}, N. Mehmer¹, T. Brueck¹

¹Werner Siemens-Chair of Synthetic Biotechnology, Department of Chemistry, Technical University of Munich (TUM), Garching, Germany; ²Heinz Maier-Leibnitz Zentrum (MLZ), Technical University of Munich, Garching, Germany; ³School of Chemistry and Molecular Biosciences, The University of Queensland, St. Lucia, Australia; ⁴Sustainable Minerals Institute, The University of Queensland, St. Lucia, Australia

We are in the middle of a climate emergency. To protect the planet for future generations, we must change the way we produce, store and consume energy. While some long-term mobility sector scenarios rely on electric or hydrogen-based car engines, complementary solutions to fossil fuels must be found and implemented now. Standard engines can already accommodate fossil fuels mixed with roughly 5 to 10% biofuel, but this is not as positive as it sounds: currently biofuel is mainly derived from plants, including edible crops, which are competing for farm land and water. The situation is even more drastic for biofuels derived from palm oils as practices around cultivating palm trees are leading to deforestation. In order to make biofuels truly green, one has to completely rethink the way they are produced.

In an ideal biofuel production scenario, a microorganism would transform biomass (e.g., industrial waste) into the necessary hydrocarbon building blocks. Microbial performance depends on (a) how much hydrocarbon is produced and (b) how quickly as well as (c) the quality of the oil. A handful of microbial contenders produce high quantities of oil. Of these, our work focused on the oleaginous yeast *Cutaneotrichosporon oleaginosus*.

In this first-of-its-kind study, we irradiated a culture of *C. oleaginosus* using extremely high-energy neutrons in the MEDAPP instrument. While human cells would be irreparably damaged by this process, in the yeast culture neutron irradiation stimulated the appearance of a large number of new characteristics. Using state-of-the-art screening methods we were able to sort and characterise the hydrocarbon production capabilities of the yeast.

One of the yeast variants that emerged after irradiation, “FN M2”, exhibits very interesting properties for biodiesel production: 23% enhanced oil productivity, which greatly contributes to the economics of yeast oil. Oil produced from FN M2 is compatible with all European and American biodiesel regulations and has an improved cetane number (CN, an indicator of combustion speed and ignition delay) of 61.62 (Table 1). Premium diesel fuels have a high CN (> 60). The variant “FN M8” is also particularly interesting as it is capable of producing many more hydrocarbons than FN M2, albeit very slowly.

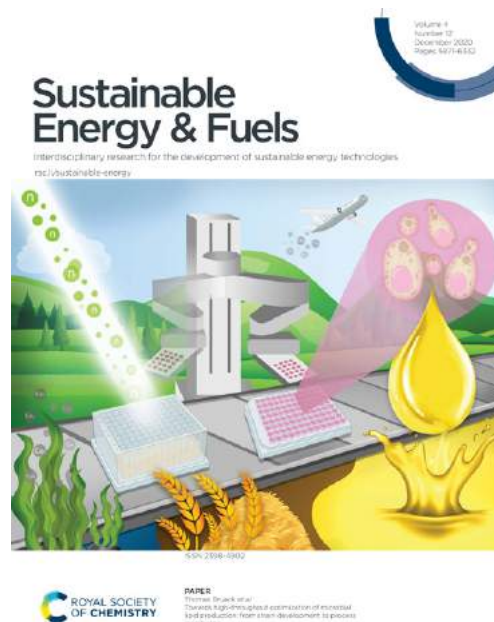


Fig. 1: This work has been published in [1]. This article is featured on the front cover of the 12th issue of Sustainable Energy and Fuels (December 2020).

Future work aims to elucidate the underlying biological differences in quantity and speed of hydrocarbon production between these two variants. It may then be possible to increase the hydrocarbon mass produced by FN M2 or the hydrocarbon production speed of FN M8.

Biodiesel Source	Cetane number (CN)
<i>L. starkeyi</i> [a]	59.80
<i>C. oleaginosus</i> wt	60.06
<i>Y. lipolytica</i> [a]	60.11
<i>C. oleaginosus</i> FN M2	61.62
<i>R. toruloides</i> [a]	62.19
Palm oil [a]	65.19
US biodiesel ASTM D6751	≤120
EU biodiesel standard EN 14214	≤120

Table 1: CN as an example property of biodiesel produced from prominent yeast strains and palm oil. [a]: Sergeeva et al. 2017

[1] D. Awad et al., *Towards high-throughput optimization of microbial lipid production: from strain development to process monitoring*, *Sustain. Energy Fuels* 4(12), 5958 (2020)

GINSES: dancing of polymer chains at solid interfaces

J. Witte¹, T. Kyrey², M. Ganeva², O. Holderer², S. Wellert¹¹Institute of Chemistry, Technical University of Berlin, Berlin, Germany; ²Jülich Centre for Neutron Science (JCNS) at MLZ, Forschungszentrum Jülich GmbH, Garching, Germany

Grazing incidence neutron spin echo spectroscopy (GINSES performed on J-NSE) combines the grazing incidence scattering (performed on MARIA) with neutron spin echo spectroscopy and enables the investigation of the dynamics of soft matter confined at planar solid substrates in the time range up to 100 ns. We discuss how virtual experiments within the distorted wave Born approximation (DWBA) with the BornAgain software can improve the GINSES data treatment and help to estimate the contributions of brush regions at different distances from the grafting surface to the observed dynamics. As an example, the dynamics of poly(*N*-isopropylacrylamide)-brushes under good solvent conditions with grafting densities in the high-density and semidilute regime at different neutron penetration depths are discussed.

Polymer brushes are polymer chains, end-tethered to a surface with a mean anchor point distance lower than the radius of gyration in a good solvent. The free-energy balance between the desire to achieve a random walk configuration and the avoidance of polymer-polymer interactions leads to the stretching of the polymer chains away from the surface. PNIPAM brushes were “grafted from” flat silicon surfaces via surface-initiated atom transfer radical polymerisation to obtain high grafting densities. Typically, a polydispersity above 1, and a certain height distribution of the end segments result from this approach.

GINSES studies of PNIPAM brushes in the semidilute and concentrated regime below the VPTT were performed (Fig. 1a) [1]. The polymer brush can be considered in a blob picture, where a blob describes a chain segment exhibiting the behaviour of a single unperturbed chain related to a local correlation length (blob size), as shown in Fig. 1b.

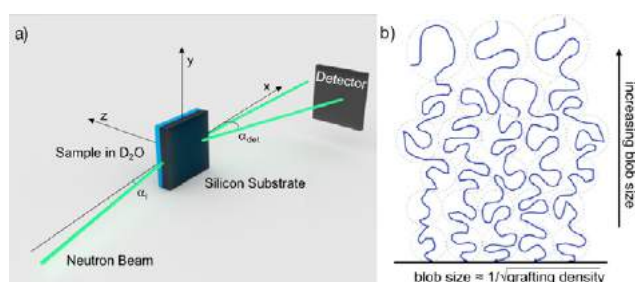


Fig. 1: a) Instead of the conventional transmission geometry in GINSES measurements a reflection mode scattering geometry is used. b) Scheme of a polydisperse polymer brush in the nonuniform blob-size picture.

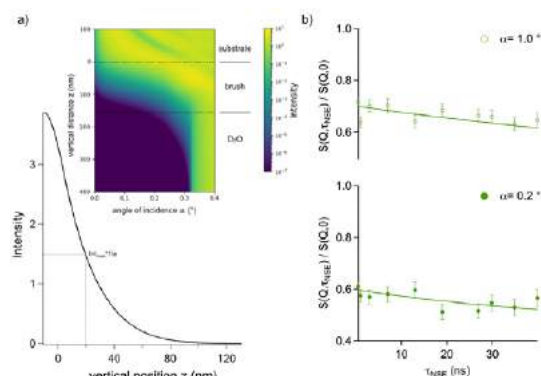


Fig. 2: a) Simulated evanescent intensity distribution for a PNIPAM brush. From a vertical line cut at an incidence angle of $\alpha_i = 0.2^\circ$. b) Intermediate scattering functions at two values of α_i above and below the critical angle of total external reflection.

The distribution of the evanescent intensity was calculated with BornAgain within the DWBA (Fig. 2a). The calculations included the instrumental resolution and layer properties. As in the real experiment, the neutron beam impinges on the interface through the silicon block. The contributions of brush regions at different distances from the grafting surface to the scattering signal, the penetration depth of the evanescent neutrons and the relative contributions of the solid-liquid interface with and without a sample layer to the observed elastic background were determined [2].

The relaxation rates of thermal fluctuations were determined by a single exponential fit to the intermediate scattering functions (Fig. 2b). The size of the correlation blobs of the polymer segments were 2.8 and 5.2 nm. Therefore, the blob size increases with increasing distance from the grafting surface.

The findings agree with simulations of the non-uniform blob model in which the final blob was found to be bigger than blobs closer to the grafting surface, reaching up to 20% of the entire brush height.

These promising GINSES experiments on PNIPAM brushes of varying grafting densities open up the potential for further work.

[1] J. Witte et al., *Grazing Incidence Neutron Spin Echo Study of Poly(*N*-isopropylacrylamide) Brushes*, *Macromolecules* 53(5), 1819 (2020)

[2] T. Kyrey et al., *Understanding near-surface polymer dynamics by a combination of grazing-incidence neutron scattering and virtual experiments*, *J. Appl. Cryst.* 54, 1 (2021)

G. V. Kulin¹, A. I. Frank¹, V. A. Bushuev², Yu. N. Khaydukov^{2,3,4}, D. V. Roshchupkin⁵, S. Vadilonga⁶, A. P. Sergeev⁷

¹Joint Institute for Nuclear Research, Dubna, Russia; ²Moscow State University, Moscow, Russia; ³Max Planck Institut for Solid State Research, Stuttgart, Germany; ⁴Max Planck Society Outstation at the MLZ, Garching, Germany; ⁵RAS Institute of Microelectronics Technology and High-Purity Materials, Chernogolovka, Russia; ⁶Institute for Nanometre Optics and Technology, Helmholtz-Zentrum GmbH, Berlin, Germany; ⁷Scientific Research Institute for System Analysis (NIISI), RAS, Moscow, Russia

Unlike usual diffraction by a stationary object, neutron diffraction on a running wave is an essentially non-stationary process resulting in the transfer of the energy $\Delta E = n\hbar\Omega$ to the neutron. Here, Ω is the wave frequency, \hbar is the Planck constant, and n is an integer. The first and, until recently, only experiment on the observation of neutron diffraction by a traveling surface acoustic wave (SAW) was carried out in the 1980's by W.A. Hamilton et al.

In our recent study [1], we reported on a new observation of this phenomenon and presented a fresh approach to its theoretical description. The appeal to this problem is due to several circumstances. First, in the years since the first experiment of Hamilton, significant progress has been achieved in neutron scattering technique, making it possible to study the phenomenon with greater accuracy. The second important circumstance is the desire to expand the range of phenomena studied, and in addition to diffraction by traveling SAWs, also observe diffraction on standing waves. In the latter case we deal with a non-stationary quantum phenomenon of reflection from an oscillating potential. It is important to note that SAWs arise due to periodical oscillation of the near-surface layer of matter that moves with alternating velocity and acceleration. For typical values of the frequency and amplitude of the ultrasonic wave, this acceleration reaches values of the order of 10^7 g.

The validity of the concept of the effective potential of matter in the case of such large accelerations is not obvious a priori.

In the experiment performed at the angle dispersive ($\lambda = 4.3$ Å) NREX reflectometer we used a YZ-cut of a LiNbO₃ crystal, a well-known SAW generator widely used in basic studies and industrial applications. On its surface two interdigital transducers (IDT) were disposed to excite travelling or standing waves with a frequency of 69 MHz. During the experiment a high-frequency electrical signal was applied to one of the two, or both, IDTs. In the first case, a SAW was generated propagating almost along a neutron beam incident on the sample at a grazing angle ($s = 1$). When voltage was applied to another IDT, a wave was generated in the opposite direction compared to the first case ($s = -1$). To excite a standing SAW, voltage was applied synchronously to both IDTs.

The experimental results are in the main consistent with theoretical predictions. The results obtained for diffraction by a standing wave are in complete agreement with the concept of it as a superposition of two traveling waves.

[1] G. Kulin et al., *Non-stationary neutron diffraction on surface acoustic waves*, *Phys. Rev. B* 101, 165419 (2020)

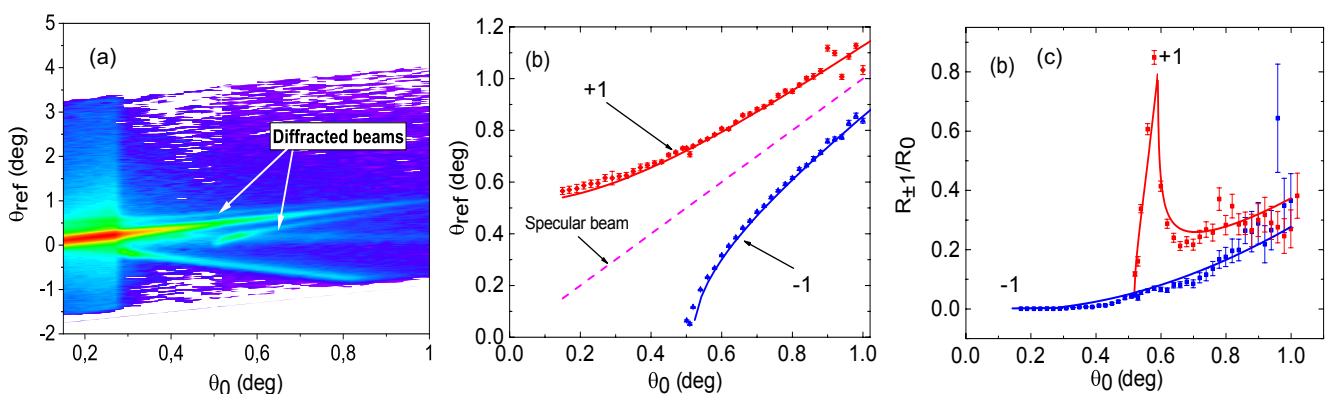


Fig. 1: Two-dimensional scattering map (a), angular distributions (b) and amplitudes of +1 and -1 diffracted beams (c) as a function of the angle of incidence for the traveling wave case $s = -1$.

T. Keller^{1,2}, P. Fabrykiewicz³, R. Przeniosło³, I. Sosnowska³, B. Keimer¹¹Max Planck Institute for Solid State Research, Stuttgart, Germany; ²Max Planck Society Outstation at MLZ, Garching, Germany; ³Faculty of Physics, University of Warsaw, Poland

A hitherto unrecognised resolution effect in neutron Larmor diffraction (LD), resulting from small-angle neutron scattering (SANS) in the sample, is reported in [1]. Small distortions of the neutron trajectories by SANS give rise to a blurring of the Bragg angles of the order of a few hundredths of a degree, leading to a degradation of the momentum resolution (Fig. 1). This effect is negligible for single crystals but may be significant for polycrystalline or powder samples. A procedure is presented to correct the LD data for the parasitic SANS. The latter is accurately determined by the SESANS technique (spin-echo small-angle neutron scattering), which is readily available on Larmor diffractometers. The analysis technique is demonstrated on LD and SESANS data from α -Fe₂O₃ powder samples.

Neutron Larmor diffraction (LD) is a high-resolution technique which permits the measurement of lattice spacings d_{hkl} and their range Δd_{hkl} . The latter arises, for example, from microstrains, magnetostriction, or structural and magnetic domains, or from a small splitting of Bragg peaks resulting from distortions of the crystal lattice.

The present work is related to a review of the symmetry properties and subsequent revision of the crystal structures of numerous compounds (I. Sosnowska et al., J. Phys. Soc. Jpn. 81, 0446041 (2012)). Synchrotron radiation (SR) pow-

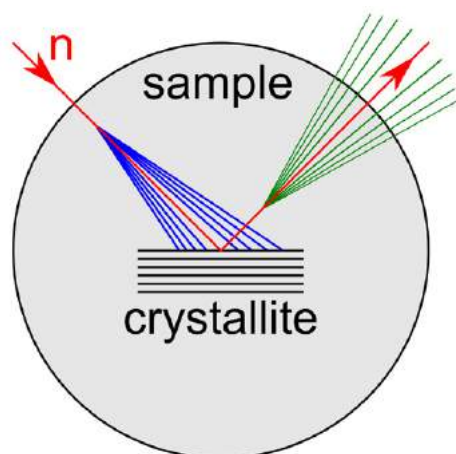


Fig. 1: SANS occurring during passage of a neutron through the powder sample (blue, green) leads to a blurring of Bragg angles and to a degradation of the resolution.



Fig. 2: Experimental team from left: I. Sosnowska, R. Przeniosło, P. Fabrykiewicz, T. Keller.

der diffraction studies of the multiferroic BiFeO₃, CaCO₃ (calcite), the transition metal oxides V₂O₃, Al₂O₃ and Cr₂O₃, and hematite (α -Fe₂O₃) have shown monoclinic symmetry instead of the previously established trigonal corundum-type structure (P. Fabrykiewicz et al., Acta Cryst. B74, 660 (2018)). The monoclinic distortion observed in α -Fe₂O₃ is of the order of $\Delta d/d \sim 2 \times 10^{-4}$, i.e. close to the detection limit of SR powder diffraction methods.

LD experiments on α -Fe₂O₃ were conducted at TRISP in order to confirm this small lattice distortion by means of a complementary technique. We show that small-angle scattering makes a significant contribution to the range of d_{hkl} measured by neutron Larmor diffraction. We describe a quantitative procedure to measure SANS by means of the SESANS scattering technique, and derive scaling expressions to include the SESANS data in the analysis of the LD data collected on flat or cylindrical samples. We show that using a flat sample in reflection geometry is preferable to using cylindrical samples, as for a given sample mass the effective neutron path length, and thus the effect of SANS, is minimised for the flat sample. Finally, we apply the new analysis method to LD data from hematite and calcite powders. These LD data confirm the hkl-dependent d-spacing range previously observed by high-resolution SR diffraction.

[1] T. Keller, P. Fabrykiewicz, R. Przeniosło, I. Sosnowska and B. Keimer, *Neutron Larmor diffraction on powder samples*, J. Appl. Cryst. 53, 88 (2020)

The MIEZE (or Modulation of Intensity with Zero Effort) technique is a variant of the Neutron Resonant Spin Echo (NRSE) technique, optimised for measurements under depolarising conditions such as applied magnetic fields or intrinsic sample magnetism. The essential feature of MIEZE is an intensity modulated neutron beam with a focal point (echo point) several meters downstream from the sample position, where neutrons of various velocities recombine constructively. The region over which this constructive recombination happens defines the ‘MIEZE group’.

Quasielastic scattering processes in the sample result in a transfer of energy from (or to) the neutrons, which smears out the intensity of this recombination depending on the energy scale of these processes. Therefore, this ‘detuning’ of the signal at the echo point allows for the determination of the quasielastic scattering processes in a sample (at the corresponding Fourier time) with very high resolution. Naturally, the 2D position-sensitive detector needs to be placed at the focal point. Since, at higher Fourier times, the width of the MIEZE group shrinks below the thickness of the combined detector foils, accurate control over the MIEZE group position is essential to ensure the highest neutron detection efficiency.

In contrast to classical neutron spin-echo, which uses only static magnetic fields, NRSE uses rotating fields at the neutron resonance frequency to manipulate the phases of the neutron spins.

When placing a solenoid (NSE coil, see the right panel of Fig. 1) between the resonant fields, it is possible to move the focal point by effectively subtracting field integral.

The NSE coil allows for a simpler and more accurate tuning of the instrument, increasing its performance and reliability. Furthermore, this enables access to shorter Fourier times, not previously achievable with neutron spin echo techniques, and thus significantly broadens the dynamical range of measurable Fourier times to over 7 orders of magnitude. These capabilities have been utilised, for example, to investigate low lying crystal field excitations in rare-earth compounds.

We calculated the MIEZE condition (position of the focal point) including the NSE coil and derived an expression for the contrast (which is proportional to neutron-energy transfer) as a function of the current in the NSE coil. Given this, it is possible to determine the width of the MIEZE group at the focal point as a function of the NSE current as well as its width in real space and compare it to measurements taken at RESEDA. The left panel of Fig. 1 shows the excellent agreement between the contrast values derived from calculations and the corresponding experimental data.

Although the size of the MIEZE group decreases in real space when going to higher Fourier times, it stays constant as a function of the current. The former needs to be taken into consideration when advancing detector development, while the latter permits the tuning of the setup with the same precision over the full range of accessible Fourier times, with no dependence on the setting accuracy of the power supply.

[1] J. K. Jochum et al., *Neutron MIEZE spectroscopy with focal length tuning*, *Meas. Sci. Technol.* 31, 035902 (2020)

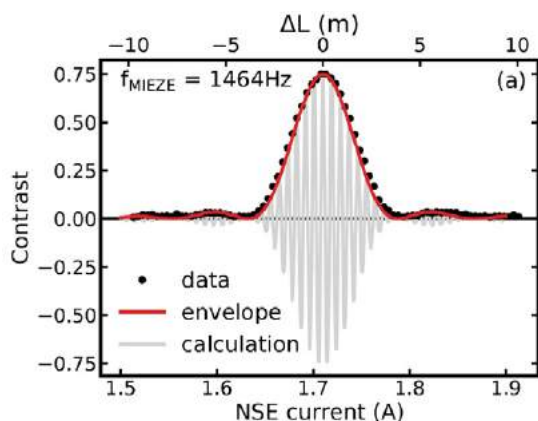


Fig. 1: Left: Contrast vs. length and current calculated and measured for a MIEZE frequency of 1464 Hz. The size of the MIEZE group at the focal point ($\Delta L = 0$) can be extracted in real space, as well as, as a function of current. Right: Photograph of the NSE coil at RESEDA.

A. Eich^{1,2}, M. Hölzle¹, Y. Su³, V. Hutanu^{2,3}, R. Georgii^{4,5}, L. Beddrich^{4,5}, A. Grzechnik²

¹Jülich Centre for Neutron Science JCNS-2 and Peter Grünberg Institute PGI-4, Forschungszentrum Jülich GmbH, Jülich, Germany; ²Institute of Crystallography, RWTH Aachen University, Aachen, Germany; ³Jülich Centre for Neutron Science (JCNS) at MLZ, Forschungszentrum Jülich GmbH, Garching, Germany; ⁴Heinz Maier-Leibnitz Zentrum (MLZ), Technical University of Munich, Garching, Germany; ⁵Physics Department E21, Technical University of Munich, Garching, Germany

Experiments under extreme conditions – high pressure, low temperature, high magnetic field – are of great interest for the study of a wide range of materials. For phenomena involving magnetic ordering at the microscopic level, neutron scattering is the standard method.

To experimentally combine pressure, temperature and magnetic field with neutron radiation, suitable pressure devices are required. For high-pressure neutron experiments, the most common type of device is the clamp cell: the pressure is applied *ex situ* before the cell is transferred to the experimental setup, which allows independent use of the same sample/cell in various setups. Despite their relatively simple design, careful optimisation is needed to reach the targeted pressure for specific applications.

We have developed a dedicated clamp cell for neutron scattering experiments in the existing cryostats and magnets on the beamlines DNS (diffuse scattering spectrometer), MIRA (cold three-axes spectrometer) and POLI (polarised hot neutron diffractometer) at the Heinz Maier-Leibnitz Zentrum (MLZ) [1]. The cell (Fig. 1) has been produced in two variants, CuBe and NiCrAl “Russian Alloy”, with predicted maximum pressures of 1.1 GPa and 1.5 GPa, respectively, at room temperature. Measurements of magnetic properties are possible due to the low paramagnetic moments of both materials.

First tests with the CuBe prototype cell at POLI to obtain the load/pressure calibration curve from a NaCl calibrant sample show that the cell can indeed be used up to 1.1 GPa. In addition, the data show that the setup could be reliably

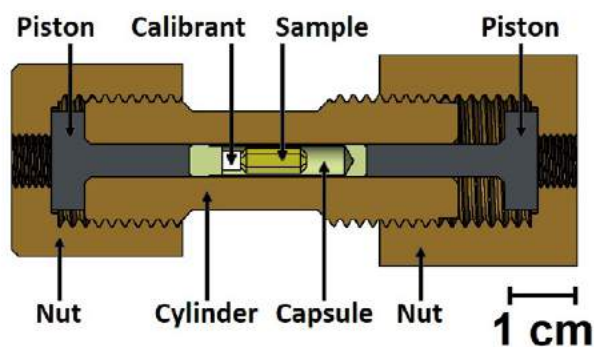


Fig. 1: Schematic drawing of the clamp cell.

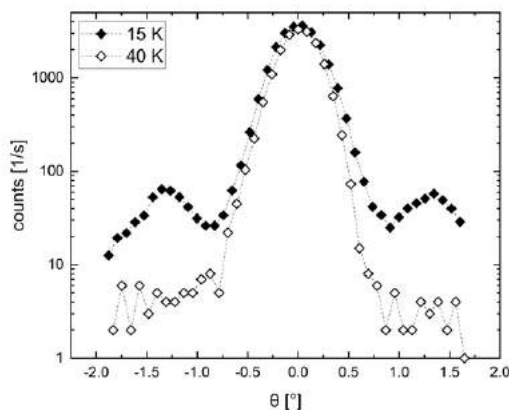


Fig. 2: Nuclear and magnetic peaks of MnSi within the CuBe clamp cell.

used to map phase diagrams by following selected reflections, and to obtain full structural data for absolute structure refinement with extended measurement time.

To determine the neutron transmission of the CuBe cell and to evaluate the feasibility of inelastic neutron scattering studies, measurements on a MnSi sample crystal were performed on MIRA within the cell at ambient pressure. The comparison of a nuclear Bragg peak within and without the clamp cell yields a transmission of $T_{\text{exp}} = 47\%$ for the cell at $\lambda = 4.05 \text{ \AA}$, in good agreement with the theoretical value (50%). Further measurements within the cell above and below the magnetic transition temperature of MnSi (29.5 K) show that beam attenuation and background are sufficiently low to detect even weak magnetic reflections (Fig. 2).

Ultimately, the newly constructed and tested clamp cells will be routinely available to the MLZ user community. Further tests of the existing cells and the development of further clamp cells for smaller cryostats and higher pressures are planned.

The work was supported by the BMBF project no. 05K19PA2 and the DFG project no. GE971/5-2. POLI at MLZ.

[1] A. Eich et al., *Clamp cells for high pressure neutron scattering at low temperatures and high magnetic fields at Heinz Maier-Leibnitz Zentrum (MLZ)*, *High Press. Res.* **41**, 88 (2021)

X. Li¹, R. van Sluijs², G. Kennedy³

¹Heinz Maier-Leibnitz Zentrum (MLZ), Technical University of Munich, Garching, Germany; ² k_0 -ware, AB Heerlen, The Netherlands; ³Department of Engineering Physics, Polytechnique Montréal, Montréal, Canada

Neutron activation analysis (NAA) is a high-sensitivity nuclear analytical technique. The widely-used k_0 method is based on experimentally determined composite nuclear constants and makes it possible to determine elemental concentrations with high precision. It was developed based on the so-called Høgdahl convention which assumes the (n,γ) reaction cross sections to follow the $1/v$ law (v is the neutron velocity) at thermal neutron energies. For the so-called non- $1/v$ nuclides, the Westcott $g(T_n)$ factors were introduced for the correction of the cross-section values at different temperatures. There have always been difficulties in the analyses of the non- $1/v$ nuclides due to large uncertainties in the neutron temperatures and the $g(T_n)$ factors.

The experiments were carried out in the highly thermalised irradiation channels of the FRM II reactor, which guaranteed negligible activation from the epithermal neutrons during the irradiation. First, the local neutron temperatures in the irradiation channels were determined in situ using irreversible thermometer labels indicating the temperatures by permanent color change (Fig. 1). They showed temperatures between 40°C and 54°C in the irradiation positions: the pneumatic transfer (rabbit) system and in the “fishing-line” position [1].

Then, the k_0 factors for six non- $1/v$ nuclides, the isotopes of Lu, Eu and Ir were redetermined by counting the activities



Fig. 1: Thermometer labels and standards after irradiation in the rabbit system.

of the samples and those of co-irradiated standards using three $g(T_n)$ factors (Gryntakis, Holden and van Sluijs). Fig. 2 shows the discrepancies (ζ -scores) between these new k_0 -values (using three g factors) and the old ones (assuming $g = 1$) for the different gamma rays. Some of them were out of the confidence interval ($|\zeta| = 1.95$), suggesting that the k_0 values needed to be revised. It has been concluded that the k_0 values of these non- $1/v$ nuclides are valid and should be used only in combination with the $g(T_n)$ factors used for their determination [2].

[1] X. Li, *In situ measurement of neutron temperature for the extended k_0 NAA at FRM II*, *J. Radioanal. Nucl. Chem.* 326, 1391 (2020)

[2] X. Li et al., *Measurement of k_0 values for europium, lutetium and iridium at FRM II with a very well thermalized neutron spectrum*, *J. Radioanal. Nucl. Chem.* 327, 533 (2021)

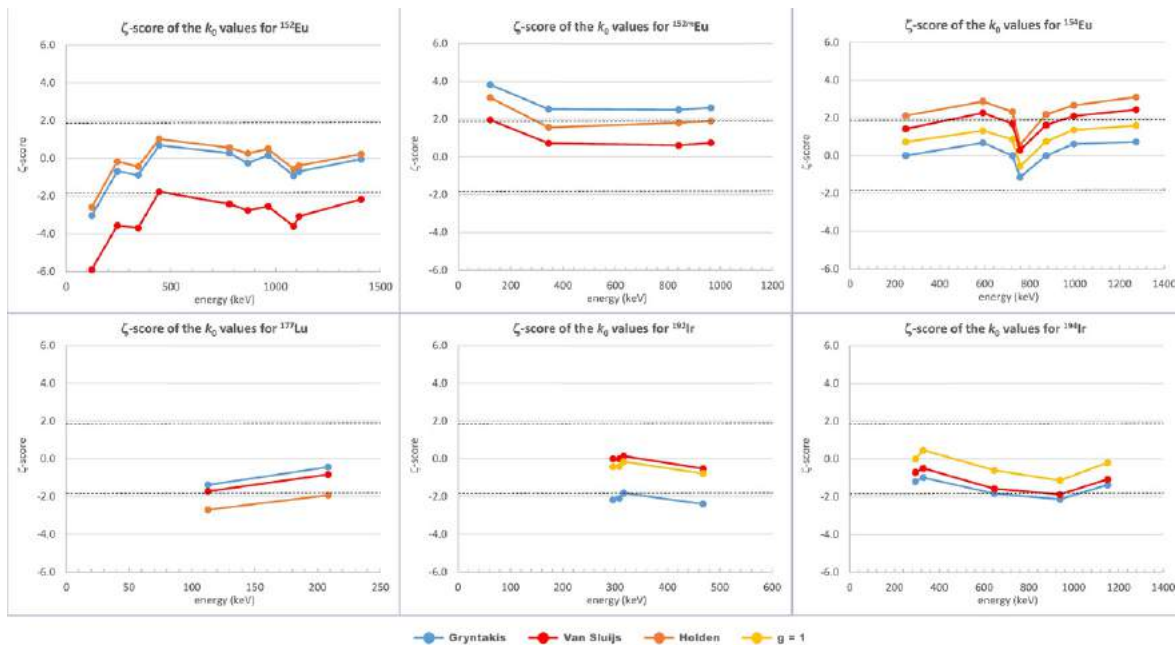
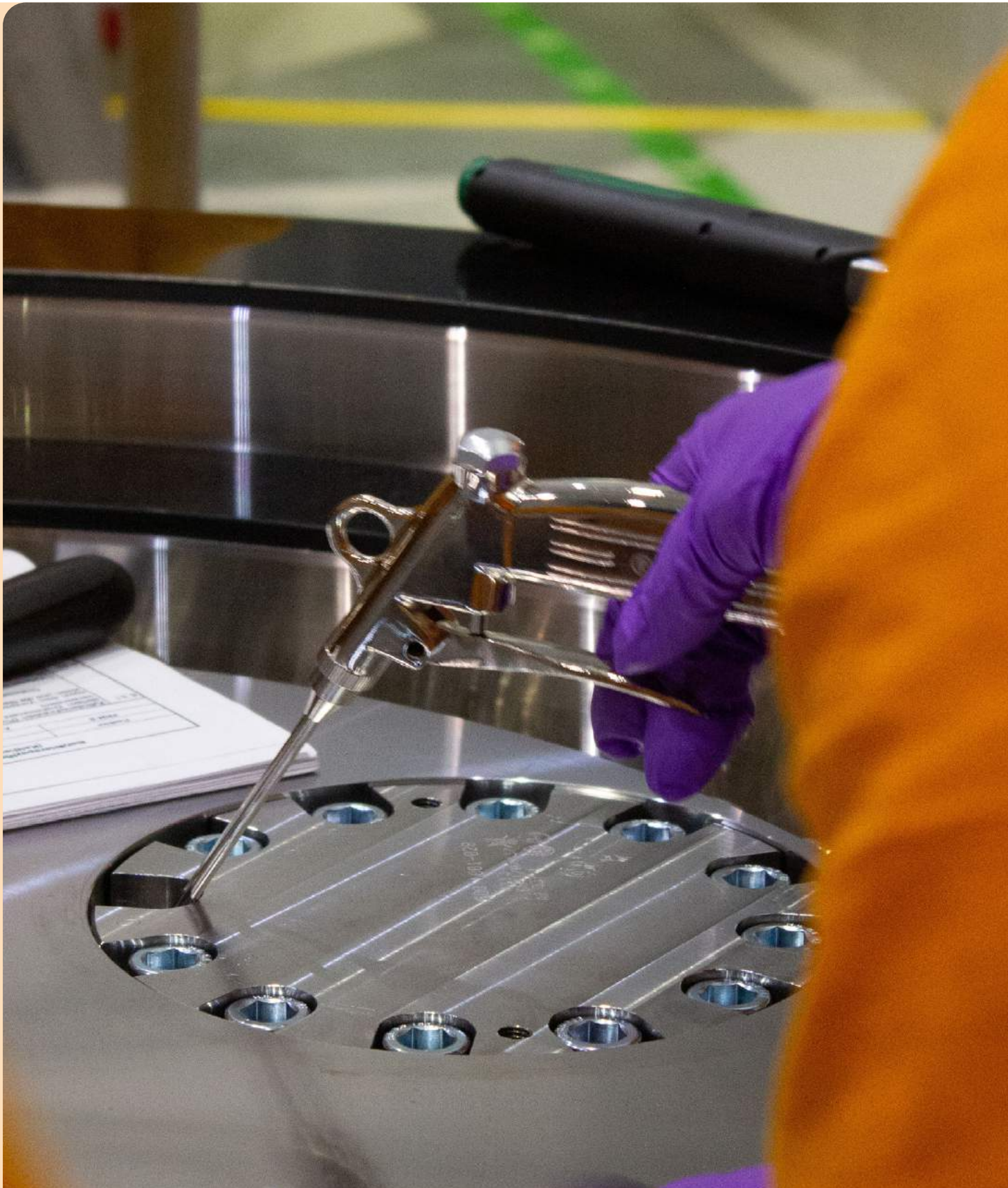


Fig. 2: Discrepancies (ζ -score) between the determined and the recommended k_0 values.

Practice test of the fuel element transport: Fixing and cleaning the screws of the transport and storage cask CASTOR MTR 3.



Reactor & Development

Finally: Fresh neutrons on the horizon

A. Pichlmaier

Forschungs-Neutronenquelle Heinz Maier-Leibnitz (FRM II), Technical University of Munich, Garching, Germany

Although it began full of promise, the Corona-pandemic and the reportable incident ME -01/2020 made 2020 a difficult year for the FRM II: we were only able to deliver one reactor cycle. Nevertheless, with the achievements made for fresh and spent fuel-transport, mastery of the reportable incident and the Corona-pandemic – hopefully by the time of publication of this report – on the retreat, there is good reason to be optimistic for 2021.

Were it not rather presumptuous, one could be tempted to quote Churchill: “blood, sweat, toil and tears” seemed to be on the FRM II agenda in 2020. Once more, in the wake of 2019. The year 2020 has indeed been remarkable in more than one respect.

From the personnel point of view: after two five- year terms in office, the technical director A. Kastenmüller left the FRM II on March 31st. As his successor, in post since July 1st, I would like to take the opportunity to express my sincere gratitude to him and thank him for all those years of dedication to the FRM II.

As for the number of neutrons delivered, the year 2020 dawned full of promise and ambition. The reactor cycle 47 was launched as planned on January 14th and ended on March 16th with only a short interruption (25th to 28th of January) due to a faulty ionisation chamber. This chamber, together with two others, is run in a 2 out of 3 logic and required for reactor power measurement. Two and a half further cycles were on the initial agenda, and this was to be one of the years when the greatest number of neutrons ever delivered was going to be achieved. Who would have imagined that 2020 would in fact become the second most challenging year in terms of reactor full power days, second only to 2019 and ex aequo to 2011, adversely affected by the Fukushima accident?

Consequences of the lockdowns

Two events changed everything and reduced all planning to not much more than a dream: the Corona-pandemic and the reportable incident of unauthorised release of the nuclide C-14. Both are in some sense intricately connected. The Corona-pandemic made – and still makes at the time of writing – all work harder and time-consuming. We are in the

midst of the dreaded second wave. Almost everything takes longer than initially planned for and is without doubt more complicated. The FRM II had almost come to a complete halt during the March/April. The partial lockdown in November again made all maintenance and operational work difficult – and regular reactor operation impossible. A major challenge was the task of keeping the FRM II as Corona-free as possible. We succeeded. Not completely, but pretty much so. A heart-felt “thank you” to everybody who, through his or her responsible behaviour, contributed to this achievement! The second lock-down and the policy of “minimum presence”, put in place by the TUM-management from December 16th, was a little more benign than the first lockdown since it was in a way predictable and occurred during the holiday season, at a time of the year when traditionally not much work is scheduled. When the TUM-management decided to suspend all but absolutely necessary work on site, we put the reactor into a safe mode with only a minimal crew present.

Reportable incident: unauthorised release of C-14

The reportable incident attracted wide publicity: locally and even internationally, the press discussed it in detail. Although there is no simple way of reporting on this incident, the radiological consequences of this release of C-14 can be summarized easily: under very conservative estimates, not even 1% of the permissible exposure limit for the general public set by law was reached. However, there is no denying that 115% of the C-14 emission limit set for the FRM II was released into the atmosphere. Aside from technical consequences concerning the strategy to contain C-14, this incident triggered even closer scrutiny of the FRM II's activities by the authorities. This is their right and duty and a fact I tend to embrace since it gave us the chance to prove how seriously we take our work and that we do respect the rules that apply. Safety was, is and always will be the top priority for everybody and every activity here at the FRM II.

Technical reasons for the C-14 emission

What had happened technically? The radioactive isotope C-14 is produced if one generates neutrons in either air or a water environment. It is formed from N-14 through a (n;p) reaction or from O-17 through a (n;α) reaction, the latter being the predominant production path at the FRM II. Other paths contribute only negligibly to the total C-14 production in the case of the FRM II. This C-14 is mainly present as H(C-14)O₃⁻ in the FRM II D₂O system. It is absorbed, togeth-



Fig. 1: It takes a lot of equipment to handle the CASTOR® MTR 3 cask. The cask in the picture is only a dummy used for training purposes.

er with many other ions, at the ion exchange resins that permanently purify the D_2O cooling loop. After some time, these resins are saturated and have to be replaced. The used resins are dried and prepared for treatment. Unavoidably, C-14 is released as $(C-14)O_2$ and emitted through the chimney into the environment – unless the air is carefully cleaned of all CO_2 . This sounds, and is in principle, easy. However, an error occurred and more than the permitted amount of this radioactive CO_2 was discharged. How much $(C-14)O_2$ was it in absolute numbers? About $2,3 \cdot 10^{10}$ Bq. This is approximately 1% of 1 Mol CO_2 or 200 ml of gas under normal conditions.

When operating a nuclear reactor, one simply has no right to exceed the permitted limits. We have been working hard to avoid any such situation in the future: we are building a new device to separate out the CO_2 before it reaches the chimney. We have identified improvements in the procedures and implemented them. We have raised the awareness of everybody working at the FRM II to these issues. We have not completed all the measures foreseen yet, but we will in time, and in line with the demands of the nuclear regulator and the expert organisations.

Preparations for fuel element transports underway

However, 2020 has not been without its brighter moments: the cold tests for the expedition of spent fuel went smoothly and will lead to a successful first campaign for spent-fuel

transports in 2021. Fig. 1 shows the operation with the CASTOR® MTR3 cask mounted on its specially designed flatbed truck. The mobile crane in the background is also required for the operation. Of all the vehicles in the picture, only the fire brigade, barely visible in the right foreground, had nothing to do with the cold tests and happened to be there for a routine operation.

No fresh fuel has arrived at the FRM II in 2020 but we have every reason to be optimistic for 2021.

More tasks and looking forward

We have completely renovated the crane in the experimental hall. It is running smoothly and inaudibly as never before. We have used the period of this shut-down to refurbish reactor systems, including all cooling loops as far as possible. New colleagues have come on board: together with those more experienced, they help us to run this magnificent machine called the FRM II. Together, we will restart the reactor and deliver neutrons not only to our scientific colleagues, but also to the local and international user community and to our industrial partners. We have every reason to look forward to 2021.

Conversion of the FRM II: Progress in fuel manufacturing and simulation

C. Reiter, B. Baumeister, K. Buducan, T. Schlitt, R. Schönecker, C. Schwarz, K. Shehu, J. Shi, W. Petry

Forschungs-Neutronenquelle Heinz Maier-Leibnitz (FRM II), Technical University of Munich, Garching, Germany

In line with international efforts to minimise the use of Highly Enriched Uranium fuel (HEU) in civilian nuclear facilities, the Forschungs-Neutronenquelle Heinz Maier-Leibnitz (FRM II) participates in the development of high density Uranium fuels which allow for lower enrichment. This is reflected not least in the role of the FRM II as a member of the HERACLES consortium. As one of the most powerful neutron sources in the world, it is crucial that the scientific performance of the FRM II is not reduced in the course of conversion to lower enrichment. Scientific performance hinges on marginal neutron flux losses, i.e. keeping a cycle length of at least 60 days and the avoidance of long shutdown periods during the course of conversion. Three different materials are considered to be suitable as high density fuel: U_3Si_2 with considerably higher uranium density than actually in use for the FRM II, disperse and monolithic U-Mo. It is foreseen that the final conversion candidate for the FRM II will be selected in 2022-23. The final selection will be based on several criteria, of which European manufacturing capabilities will be one. In this report we concentrate on recent progress in the development of a European manufacturing process for fuel plates based on bare uranium-molybdenum foils, an update of the major irradiation test as well as the installation of a new thermal-hydraulic test lab.

Development of a European manufacturing process for bare uranium-molybdenum foils

The TUM has joined forces with the FRM II's fuel manufacturer, Framatome-CERCA, to develop and put into operation a European U-Mo foil manufacturing capability. U-Mo foils produced by this new installation will be used first in the upcoming FUTURE-MONO-1 irradiation test.

Fig. 1 depicts the necessary steps in the European manufacturing process of U-Mo fuel plates as identified up to now. The production of monolithic U-Mo fuel plates begins with casting of the raw materials to obtain U-Mo coupons. Sub-

sequently, a coupon is enclosed in a stainless steel canister by laser welding. This assembly is then flat-rolled to get a bare U-Mo foil. The U-Mo master foil obtained is then cut using a laser to get the desired dimensions for the application of the zirconium interlayer, which acts as a diffusion barrier between fuel and cladding, using PVD. Finally, the aluminum cladding is applied via Framatome's proprietary C2TWP process.

In 2020, the laser welding and cutting process was further developed and optimised as well as the casting of U-Mo coupons. For 2021, the installation of the cold rolling equipment and further experiments on inert hot foil rolling is envisaged, the main objective being to obtain the first U-Mo bare foils produced in Europe beginning in 2022.

Irradiation Tests

The fuel development process of the HERACLES consortium has produced promising results with regard to irradiation tests of the individual fuel candidates.

EMPIRE: In the EMPIRE mini-plate irradiation campaign, several mini-plates with disperse and monolithic U-Mo were irradiated in the ATR reactor at the Idaho National Laboratory, USA. All mini-plates had been manufactured by Framatome-CERCA, the monolithic samples being the first of a European production. During the irradiation to partially high doses, all plates behaved very well; no leakage of fission elements and no undue swelling was observed. At the end of the irradiation in August 2018 and after a subsequent radioactive decay period, the irradiation capsules were first inspected optically. Meanwhile, the non-destructive post-irradiation swelling measurements had been completed. Swelling as a function of burn-up behaves almost linearly, in particular the monolithic test plates. In collaboration with TUM staff, the destructive Post-Irradiation Examinations (PIEs) were started in 2020 but had to be halted due to the global pandemic. The TUM and the INL are currently working on the restart of these PIEs and it is expected to have the results in 2021.

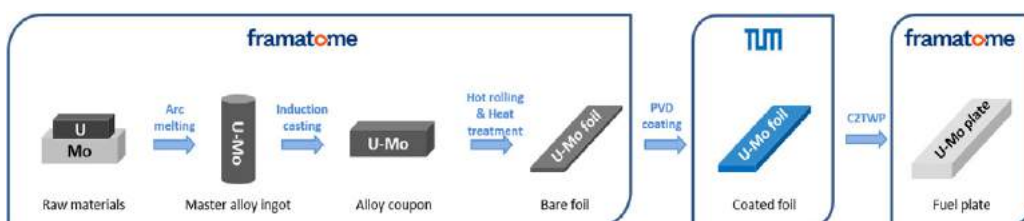


Fig. 1: Flowchart of the European manufacturing process for monolithic U-Mo fuel plates.



Fig. 2: Top: Different steps during the manufacturing process. Bottom: Assembly composition (a) and laser-welded assembly (b).

SEMPER-FIDELIS: SEMPER-FIDELIS is the central irradiation test for full-scale disperse U-Mo fuels of the EU funded HERACLES-CP project, for which the TUM was the project leader. The irradiation took place at BR 2, Mol. The basic PIEs were successfully performed at SCK CEN in 2020. Upon completion of the advanced PIEs in 2021, a report with the main results and recommendations as to how disperse U-Mo fuel can be further developed will be issued by the Fuel Development Expert Group.

HiPROSIT: The fuel plates of the HiPROSIT with an U_3Si_2 loading as high as 5.6 g/cm^3 were successfully manufactured at Framatome-CERCA in mid 2019 and subsequently successfully loaded for irradiation in the BR2 material test reactor in Mol, Belgium, at the end of 2019. All irradiation cycles were successfully completed and the visual inspections performed to date show that no damage to the plates could be detected. Currently, the fuel plates are in the cooling phase and the PIEs will start when that has finished. First results are to be expected in 2021.

New hydraulic test laboratory

State-of-the-art computation of the thermal-hydraulics and thermodynamics of the cooling will form part of the nuclear licensing of the newly fueled core. For that purpose Computational Fluid Dynamics (CFD) simulations have to be benchmarked, i.e. validated. To that end, the three high performance research reactors HFIR (Oakridge Nat Lab), HFR (Institute Laue Langevin) and the FRM II, all having a single compact fuel element with plates of involute shape, have joined forces and formed the Involute Working Group.

First high-fidelity CFD simulations were able to reproduce existing experimental data, covering in part the operating conditions for high-performance research reactors. While being useful, these experimental data are narrow in scope (e.g. geometry, operating conditions) and lack some critical input data (e.g. measurement uncertainty). Given the ongoing international conversion program, it is crucial to get more data, which should be acquired using state-of-the-art technology suited to CFD validation. Hence, the TUM is upgrading its existing test loop at the Chair of Nuclear Technology to simulate high-performance research reactor conditions and designs.

The test section can easily be changed in order to fit particular involute plate designs. In addition, the pressure and mass flow in the loop will be enhanced to achieve relevant heat fluxes. This upgraded loop will be an ideal instrument to validate heat transfer and boiling phenomena, such as the Onset of Nucleate Boiling (ONB), in CFD simulations.

Acknowledgement

This work was supported by a combined grant (FRM2023) from the Federal Ministry of Education and Research (BMBF) and the Bavarian State Ministry of Science and the Arts (StMWK). This work was supported by the European Commission within the framework of HORIZON 2020 through Grant Agreement 661935 in the HERACLES-CP project and Grant Agreement 754378 in the LEU-FOREVER project.

Many hearts for the MLZ! At the inauguration party, which had been planned as a live event but had to be held online, the MLZ distributed ginger bread hearts to the participants.



Facts & Figures

The year in pictures

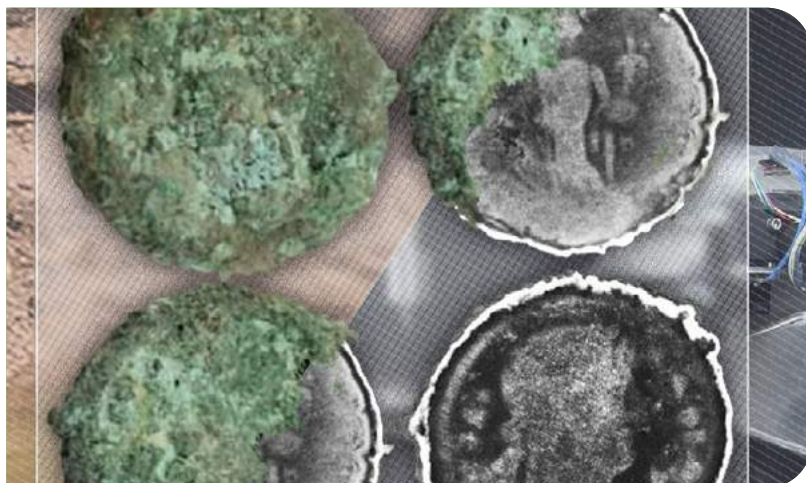


January 24th

For the second time, the management team of the FRM II, Dr. Anton Kastemüller (2nd from left), Technical Director until March 2020, and deputy director Dr. Heiko Gerstenberg (1st from left), met for an exchange of information with representatives of the interim storage facility for fuel elements and of the city of Ahaus.

March 24th

Delivery of ultrapure water from the FRM II to the Michaeli pharmacy in Moosburg for surface disinfectants (from left, front): Michael Wüst (Director THW Freising) and Manfred Danner (reactor operator at the FRM II).

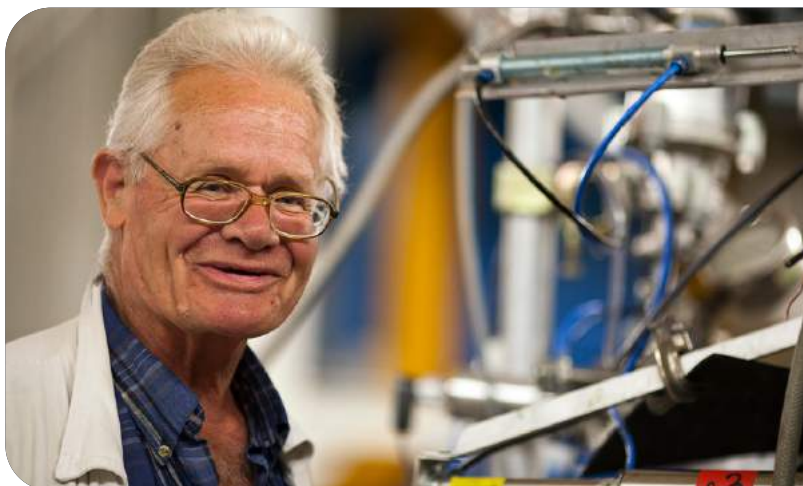


April 1st

Taking a look into ancient vases or exploring the forging technique of ancient Indian swords – archaeologists can now do this and much more at the Heinz Maier-Leibnitz Zentrum within the IPERION HS project. The EU has been supporting the 68 participating institutes since April with a total of 6.2 million euros over a period of three years.

May 2nd

In memory for Prof. Dr. Albert Steyerl, the inventor of the neutron turbine, who died on 2 May at the age of 81. Albert Steyerl at the age of 73 years.



September 7th

Live connection from the Euro-Science Open Forum in Trieste, Italy, to Laura Guasco at the neutron guide hall at the MLZ (left on the screen).

September 7th

District Administrator Helmut Petz (front, 2nd from left), visited the FRM II with his staff members. The three directors of the research neutron source showed the visitors around the facility (front, from left): Robert Rieck, Dr. Axel Pichlmaier and Prof. Dr. Peter Müller-Buschbaum.





September 23rd

Reactor operators and shift supervisors of the Isar nuclear power plant (KKI) visited the research neutron source Heinz Mair-Leibnitz (FRM II) to exchange information with their colleagues on site.

September 30th

Welcome to the FRM II: New TUM staff members are greeted by Scientific Director Prof. Dr. Peter Müller Buschbaum (right), Administrative Director Robert Rieck (2nd from right) and Technical Director Dr. Axel Pichlmaier (middle, white shirt).



October

Donation for a newly established fire department in Hungary: 16 firefighting outfits are handed over by Wolfgang Wagner (l.), the organizer and district fire chief, as well as FRM II reactor operator Manfred Danner (r.) to András Schumicky (m.), from Hungary.

October 22nd

Church blessing for the new MLZ buildings was recorded and sent via live stream to the 200 participants at the inauguration ceremony: Katarina Freisleder (r.) of the evangelist university municipality and Dr. Thomas Schindler of the catholic university municipality.

**October 29th**

Plenty of space: The new interim level in the neutron guide hall east contains 30 tons of steel, 140 tons of concrete, and its 350 m² provides space for 7 measuring cabins.

November 3rd

Staff members proudly present face masks made in the FRM II in-house sewing facility.



Awards



January 7th

PhD candidate Neslihan Aslan is carrying out research in the area of hydrogen storage at the Heinz Maier-Leibnitz Zentrum (MLZ). In January the scientist was awarded the Fuat Sezgin Prize, which is offered by the Presidency for Turks Abroad (YTB) of the Turkish Ministry of Culture and Tourism.

September 21st

Prof. Dr. Peter Müller-Buschbaum (left) hands over the Prize for Instrumentation and Scientific Use of the MLZ to retired Prof. Dr. Georg Roth, while observing safe distancing.



November 3rd

Another cause for celebration at the MLZ: With their work on a new material for power plant turbines, Dr. habil. Ralph Gilles (I.) and Dr. Markus Hölzel won the Werner Köster Award for the best publication in the "International Journal of Materials Research" of 2019.

Workshops, Conferences and Schools

①	13 January - 14 December	Seminar: Neutrons in Research and Industry, Garching	TUM / MLZ
②	27 - 31 January	F-Praktikum, Hands-on training for TUM physics students, Garching	TUM / MLZ
③	2 - 3 March	“New Imaging with Neutron and X-ray Methods for Archaeology and Cultural Heritage” (NINXMACH), Garching	TUM / MLZ
④	22 - 26 June	F-Praktikum, Hands-on training for TUM physics students, Garching: online	TUM / MLZ
⑤	31 August - 11 September	24 th Laboratory Course Neutron Scattering: Practical course for prospective neutron scatterers, Jülich and Garching: online	JCMS / RWTH Aachen / MLZ
⑥	18 - 22 October	Bavarian-Czech Mini-School, Garching and Prague: online	TUM / MLZ
⑦	27 - 30 October	10 th Serpent User Group Meeting, Garching: online	TUM / MLZ
⑧	8 - 9 December	MLZ User Meeting 2020, Garching: online	MLZ
⑨	9 - 10 December	German Neutron Scattering Conference, Garching: online	MLZ / KFN



Between dinosaur eggs and the discharge of C-14

A. Görg, A. Voit

Heinz Maier-Leibnitz Zentrum (MLZ), Technical University of Munich, Garching, Germany

Even though we thought we had already reached a plateau, this year's press coverage which saw 882 articles published about the FRM II and the MLZ even topped previous years. This is again double the last record year of 2019, which was almost double 2018. More than 40 press enquiries reached us in 2020 via 'phone or email.

Hot topics in the year of the pandemic

Hot topics for the media were the reportable event involving the increased discharge of C-14 at the research neutron source (445 articles), the interim storage in Ahaus (44 articles) and the legal question of the legality of the operation of the FRM II with highly enriched uranium (27 articles). The FRM II and TUM issued 16 press releases on these and scientific topics, while our partner institutions launched four more press releases that included MLZ topics. This is how science-driven topics also attracted a lot of attention with a total number of 131 articles, among them the 67 million-year-old dinosaur eggs from China which scientists examined at the MLZ (26 articles).

News, stories, posts and tweets

This year, we published 54 news items and four stories on the websites www.mlz-garching.de and www.frm2.tum.de. In addition, we published 110 German posts on Facebook www.facebook.com/frmII and 68 English tweets on

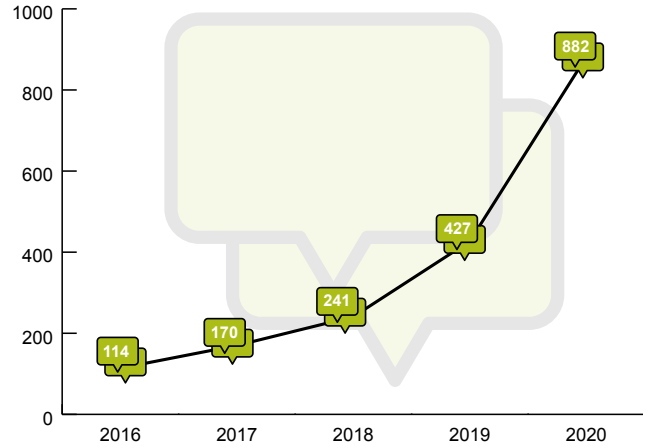


Fig. 2: Media coverage of FRM II/MLZ in numbers from 2016 to 2020.

www.twitter.com/mlz_garching to reach further target groups. Currently we have 236 international followers on twitter. At the beginning of our twitter activities, in 2019, there were just 90 followers.

More than 10 radio and TV contributions

In the era of Covid-19 in particular, the focus was on success stories on radio and TV (münchen tv, BR tv, BR radio, etc): such as the production of ultrapure water at the FRM II for disinfectants and the presentation of the new scientific director at the MLZ. The anniversary of the shutdown of the atomic egg and the opening of the new MLZ buildings, as well as the reportable event C-14, were also featured on TV and radio.

Science for everyone

As every year since 2016, the Heinz Maier-Leibnitz Zentrum was a guest at the Deutsches Museum. The lectures from the series "Wissenschaft für jedermann" offer interested non-professionals an accessible introduction and give ex-

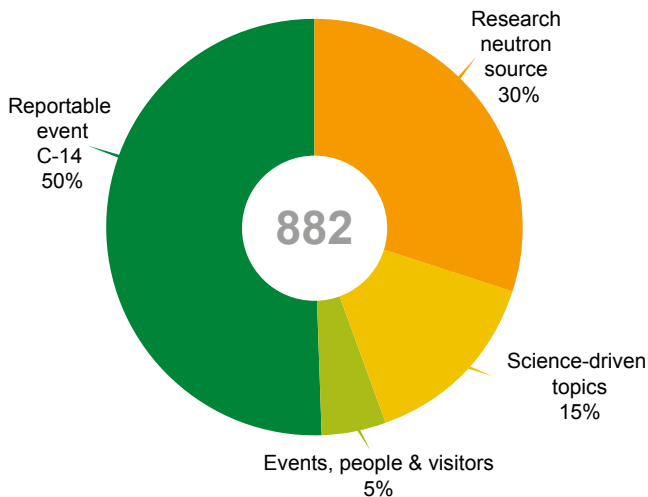


Fig. 1: Topics and percentages of the 882 media articles published on FRM II and MLZ in 2020.



Fig. 3: Shooting - Muenchen.tv with Christopher Griewel in Corona times visiting FRM II: Ultrapure water production at FRM II for the production of urgently needed disinfectants.

Join us at the
Science in the
City Festival
@ESOF_eu on
2-6 September at
@ERF_AISBL booth in
Trieste, or online.

Neutrons for Research
and Innovation

MLZ
Heinz Maier-Leibnitz Zentrum

Sun at will! Neutrons show us how
to capture solar energy with organic
thin films
Gaetano Mangiapia
9/2/20 10.30-10.45 h • 9/3/20 11.30-11.45 h

New hydrogen storage
materials and how to find them
Laura Guasco
9/2/20 11.30-11.45 h • 9/4/20 11.00-11.15 h
9/3/20 12.30-12.45 h • 9/4/20 13.00-13.15 h

About the risk and the side effects
of Ibuprofen, a study with neutrons
Stefano Pasini
9/2/20 12.30-12.45 h • 9/3/20 10.30-10.45 h

ERF-AISBL
Association of European-level
Research Infrastructure Facilities

ESOF2020
EUROSCIENCE OPEN FORUM
TRIESTE

Fig. 4: Live talks from the Neutron Guide Hall (MLZ) to Trieste (ESOF).

perts entertaining and well-founded insights into science. Shortly before the pandemic, MLZ scientist Prof. Dr. Christoph Hugenschmidt gave a lecture on research with antimatter (positrons) to an audience of more than 200.

Virtual events

The 9th EuroScience Open Forum (ESOF), which took place in Trieste (Italy) as a hybrid event, was particularly successful. MLZ scientists presented exciting scientific findings live from the Garching neutron guide hall as part of the "Science in the City Festival" and answered questions from the audience, whether they were live in Trieste or virtually connected.

Interspersed with the live broadcasts, English films about research at the individual science institutes were shown. The MLZ participated with a film about research on antibiotic resistance and imaging with neutrons. The opening ceremony of the new MLZ buildings with over 200 invited guests was



Fig. 5: Virtual tour through the MLZ buildings, which opened in October 2020 and provide a total of 4,550 square meters of floor space for laboratories, offices and workshops.

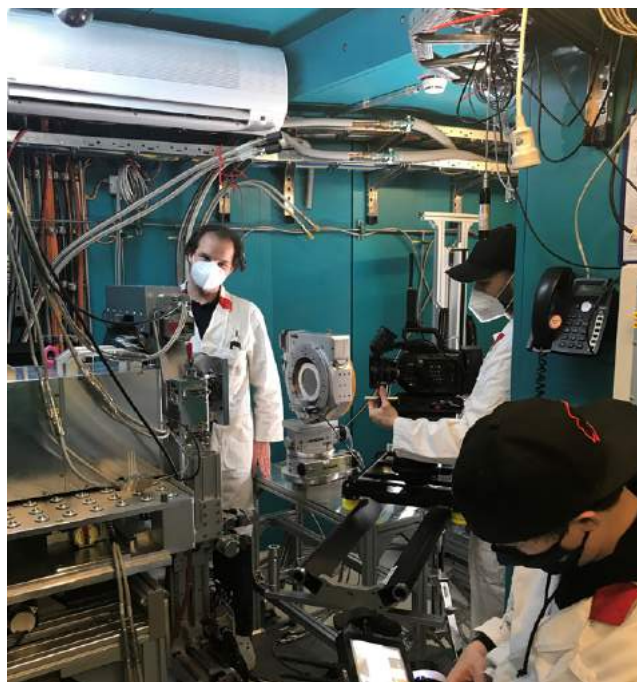


Fig. 6: Filmmaking at the ANTARES radiography facility at the MLZ. Project film "Embossing instead of cutting": How electric motors can run even more efficiently.

also switched to a purely virtual format at short notice. The ceremony took place virtually and featured speeches, and the participants also experienced the planned guided tours through the new MLZ buildings by means of a short film, produced by the FRM II / TUM.

Visitors live at the research neutron source

In 2020, the FRM II welcomed 602 visitors: Most of them came before the outbreak of the pandemic, the remainder despite Covid-19 in small groups and under strict hygiene rules, i.e. wearing masks and maintaining a safe distance.

At the User Office in the era of the pandemic

R. Bucher¹, F. Erdem², I. Lommatzsch^{1,2}

¹Jülich Centre for Neutron Science (JCNS) at MLZ, Forschungszentrum Jülich GmbH, Garching, Germany; ²Heinz Maier-Leibnitz Zentrum (MLZ), Technical University of Munich, Garching, Germany


Yes, there had been periods with no users in previous years, due to maintenance breaks or the lack of fuel elements, for example. But in 2020, everything was quite different. The one cycle we delivered ended almost simultaneously with the start of the lockdown in Germany. The User Office became a Home Office...

Spooky proposals

Before any one of us had even learned to spell the word “Corona”, we called for proposals. It was to be a thrilling round this time, because it was the first using our new online system GhOST. After the User Meeting in December 2019, when we were open for registration, proposal submission under full load was the next milestone. We received 285 proposals and a lot of feedback from the users – and at our home offices, we solved many problems with this completely new system during the crucial phase: the last three days before the deadline!

The review meeting took place in May. The usual meeting in person at Munich Airport followed by a nice dinner in the evening became a two day focussed online meeting. Everything went well and the next milestone of GhOST – the external reviewing process and its finalisation – was achieved.

Going East!




Despite the restriction due to the Covid-19 pandemic, there has been done a lot at the Neutron Guide Hall East during the last months. The most visible: The new interim level for the measuring cabins is ready – but there is so much more!

Read more →

Let's talk about...

.... (Involuntarily) virtual events


To organize events is quite challenging due to the current and often adjusted restrictions. How to deal now with a weekly seminar? And what about a neutron school? Learn more in an interview with two colleagues who mastered this task!



Read more →

People

Newly arrived



Meet some new colleagues at the instruments! This time: RESEDA, KWS-1, SPHERES, J-NSE – and the User Office!

Fig. 1: Three topics in the first digital MLZ Newsletter.

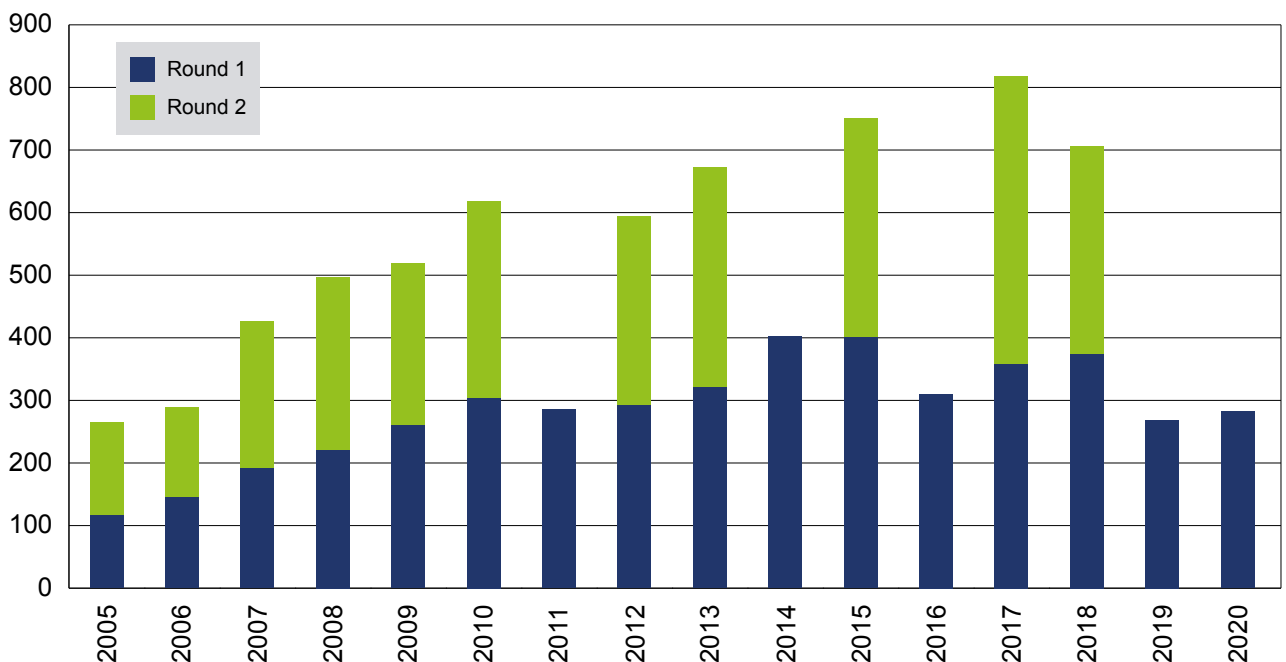


Fig. 2: Proposals submitted since the start of user operation at FRM II.

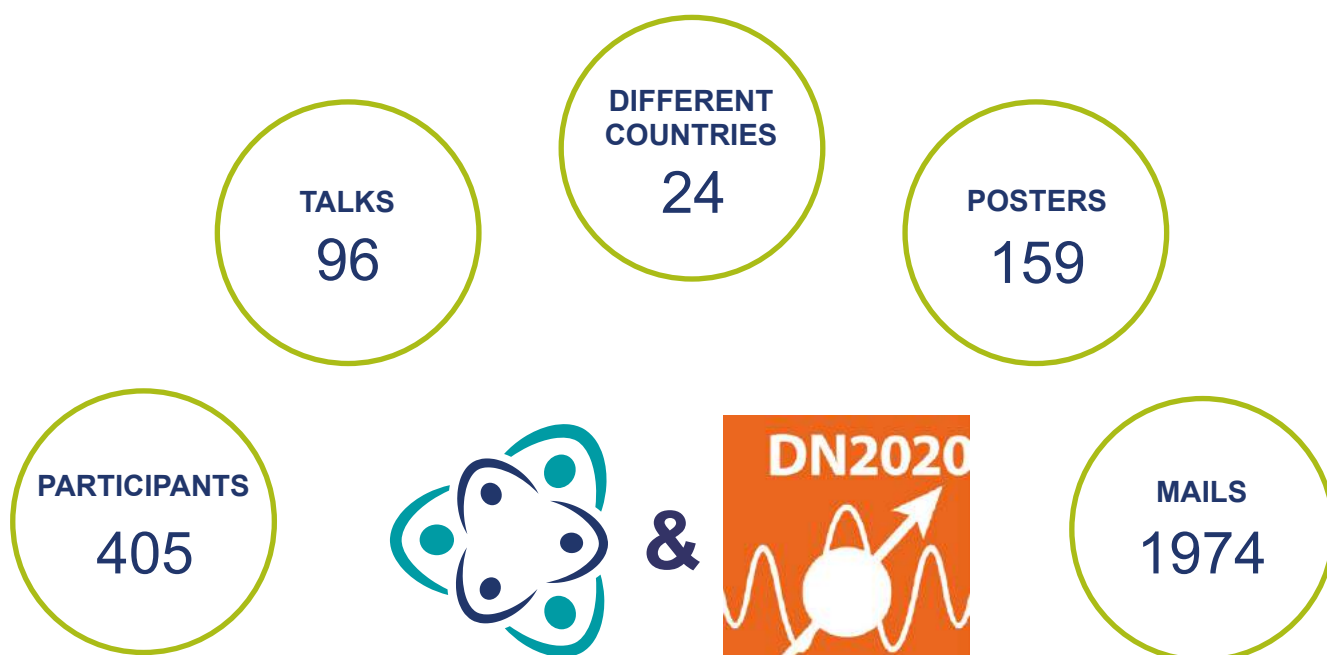


Fig. 3: Normally, a conference office is hustling and bustling with people. This time all problems were solved online.

We were able to accept 149 of the 285 proposals submitted, and of the 1683 days of beam time requested, 743 were granted.

New ways for the newsletter

The MLZ newsletter was established in 2008 and has undergone several make-overs. After 24 printed issues – of which about 1000 had been sent to readers twice a year by post – we decided to invent it anew. We therefore switched to a digital newsletter at the end of the year. Having been in preparation from the summer onwards, it was ready just after the User Meeting. It will be available four times a year, and will provide information on everything that is of interest to users of the MLZ.

Meetings without meeting

When the decision was taken at the end of 2019 to combine the MLZ User Meeting 2020 with the German Neutron Scattering Conference (DN2020), we looked forward to a lively

meeting in Munich in December 2020: We expected to host about 400 participants for three days and both conferences were to be linked by a joint poster session with beer and pretzels.

Yes, 405 participants registered for the event – and we went completely virtual like so many others this year. It turned out to be a very pleasant event with challenging sessions of 159 posters and 96 talks, but we all missed the social exchange we are used to at these meetings.

Old and new faces

In April, Ina Lommatzsch took over as the new head of the User Office. Part of the team since 2008, she is well known in the user community and looks forward to all her new tasks! In addition and to complete the team of three, Furkan Erdem joined in December and earned his first spurs during the MLZ User Meeting and DN2020.

Organisation

FRM II and MLZ

The Forschungs-Neutronenquelle Heinz Maier-Leibnitz (FRM II) provides neutrons for research, industry and medicine and is operated as a Corporate Research Center by the Technical University of Munich (TUM). The scientific use of the FRM II, with around 1000 user visits per year, is organised within the Heinz Maier-Leibnitz Zentrum (MLZ).

The chart below shows the overall network comprising the Neutron Source FRM II and the MLZ, as well as the funding bodies and the scientific users performing experiments at the MLZ addressing the grand challenges of our todays society.

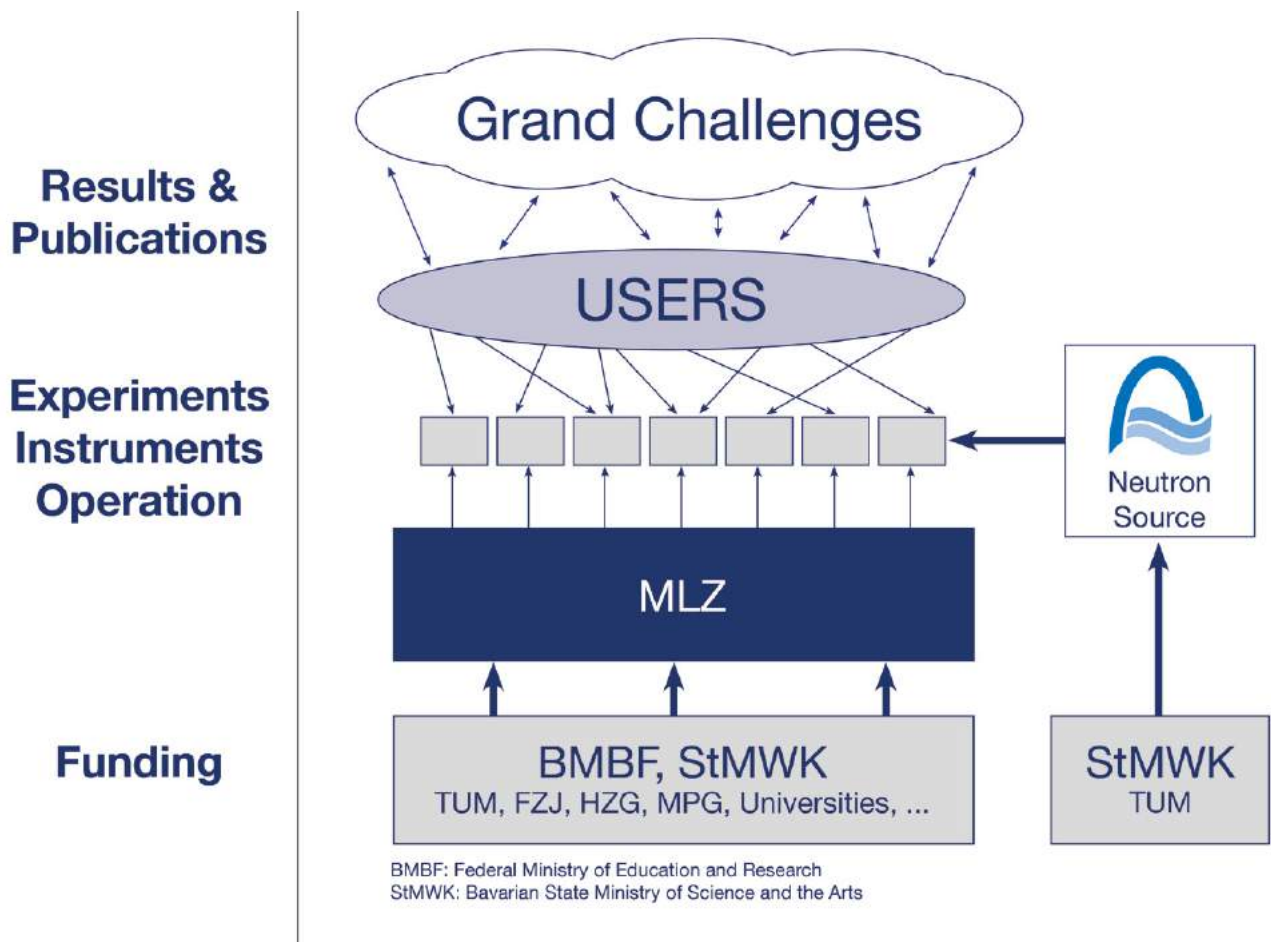


Fig. 1: The neutron source FRM II and the user facility MLZ.

Scientific Director MLZ, FRM II
Prof. Dr. Peter Müller-Buschbaum

Technical Director FRM II
Dr. Axel Pichlmaier

Scientific Director MLZ, HGF
Prof. Dr. Stephan Förster

Administrative Director FRM II
Robert Rieck

Scientific Cooperation at the Heinz Maier-Leibnitz Zentrum (MLZ)

The Heinz Maier-Leibnitz Zentrum with its cooperation partners Technical University of Munich (TUM), Forschungszentrum Jülich GmbH (FZJ) and Helmholtz-Zentrum hereon GmbH¹ is embedded in a network of strong partners including the Max Planck Society (MPG) and numerous university groups exploiting the scientific use of the Forschungs-Neutronenquelle Heinz Maier-Leibnitz. The organisational chart of the MLZ is shown below.

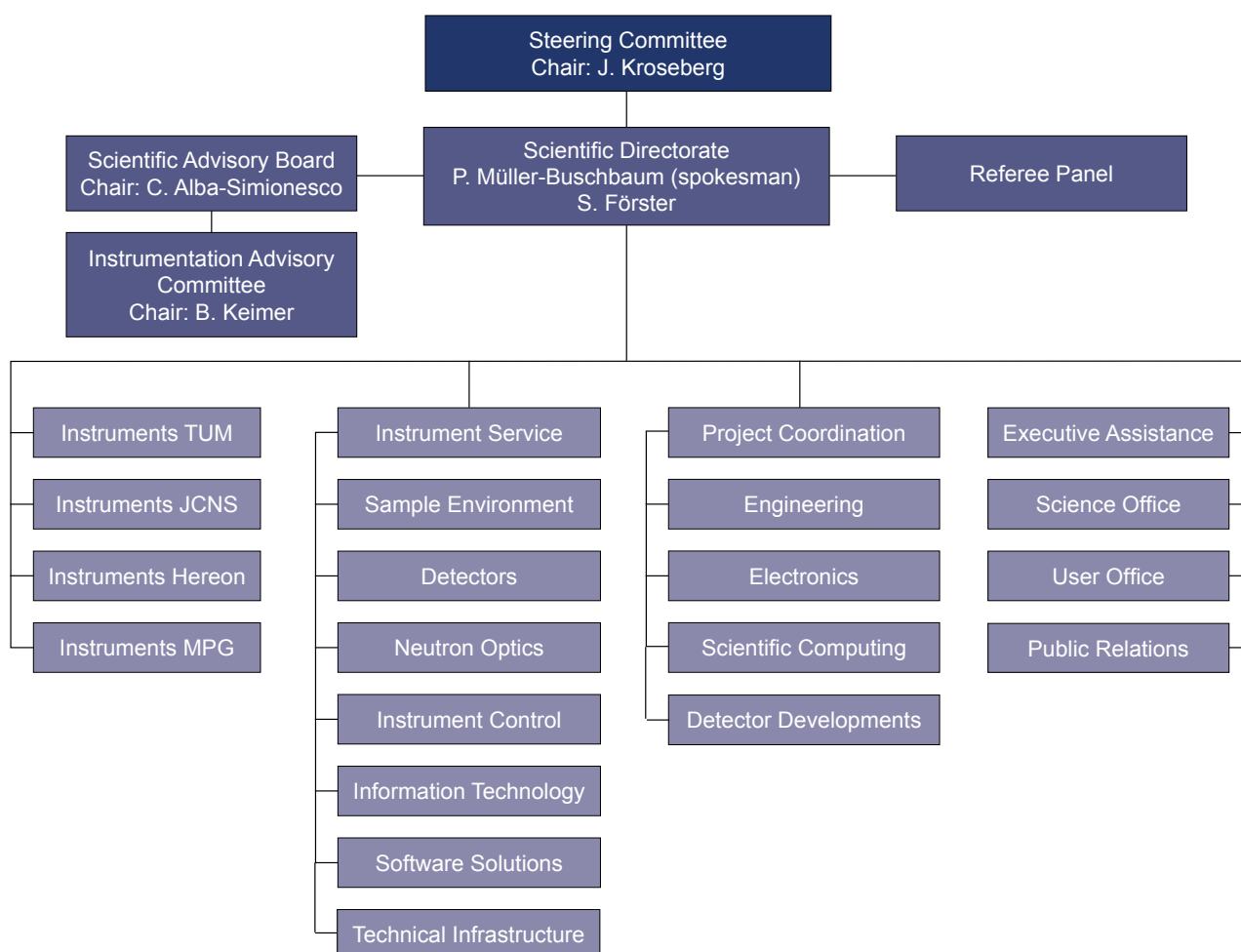
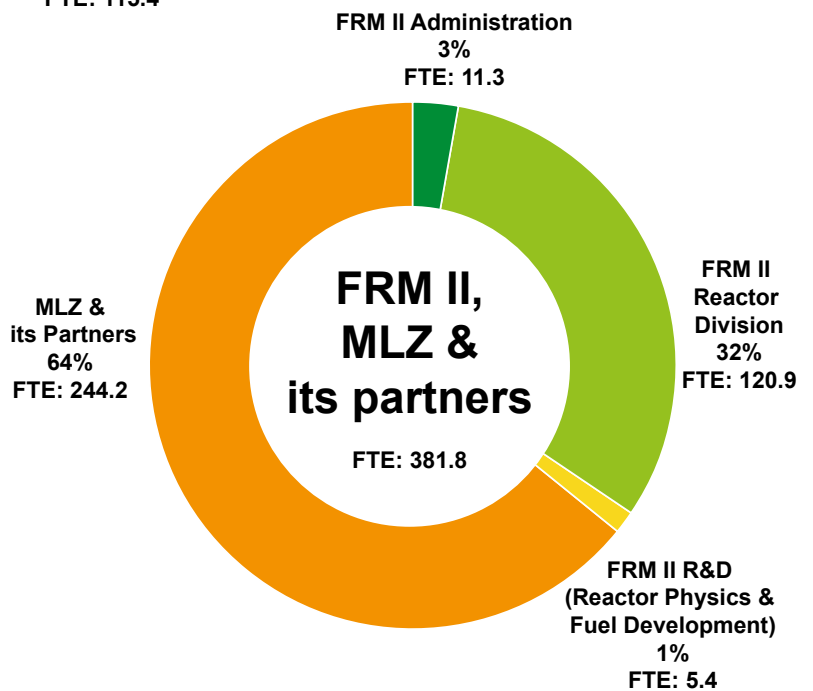
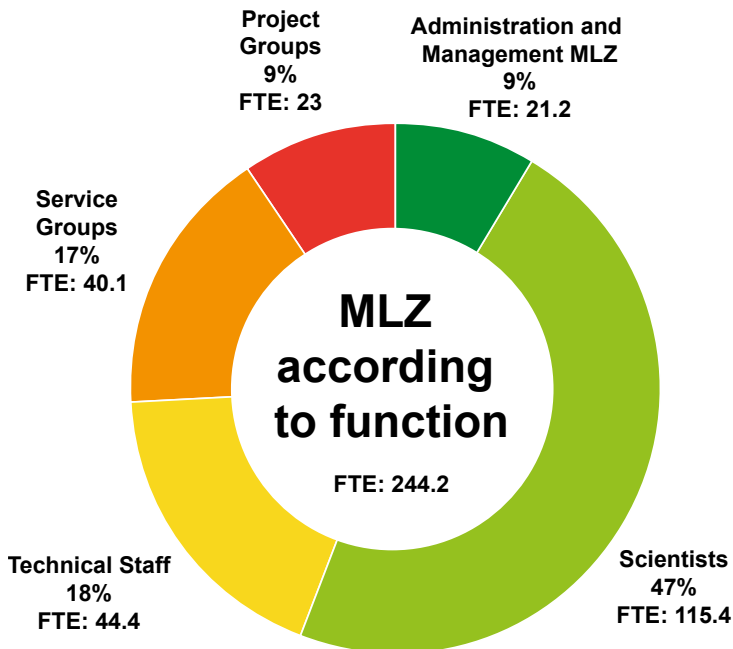
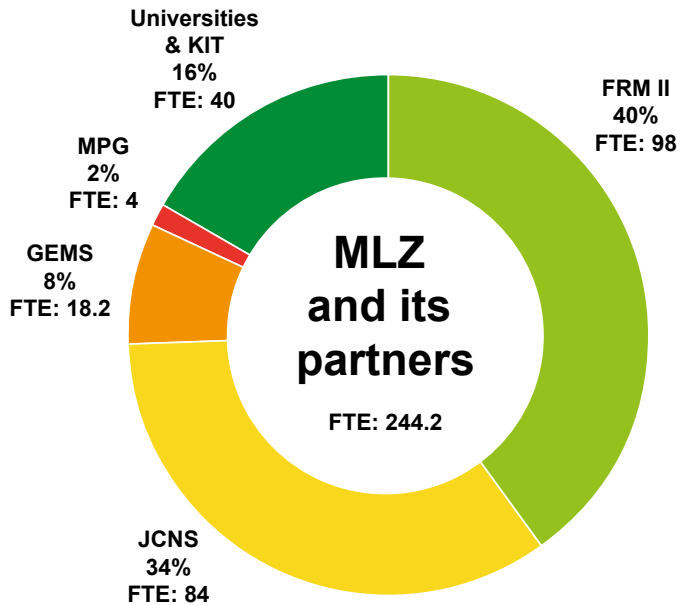


Fig. 2: Organisational chart MLZ.

¹Since the 31st of March 2021 the Helmholtz-Zentrum Geesthacht – Center for Materials and Coastal Research GmbH has a new name: Helmholtz-Zentrum hereon GmbH. More information: www.hereon.de/name

Staff

The charts below show the staff of MLZ and FRM II. The staff of MLZ according to its share among the partners with a detailed view according to the function within the MLZ is depicted as well.



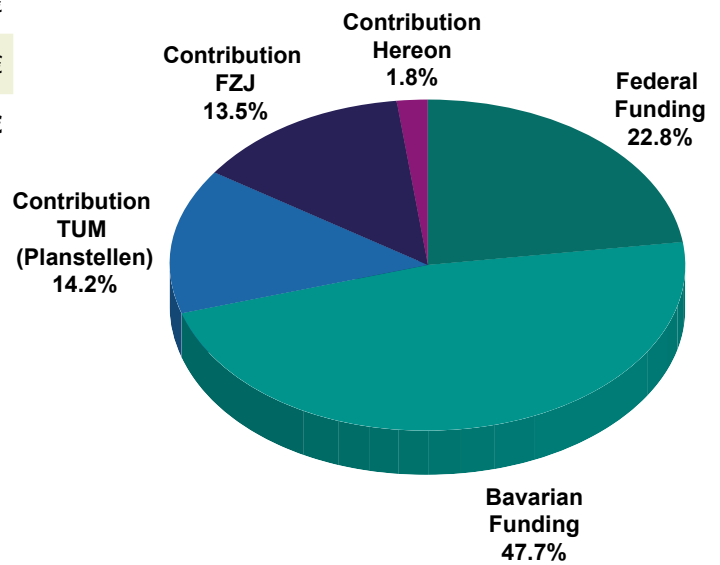
FTE = Full Time Equivalent

Budget

The tables and charts below show the revenue and expenses in 2020.

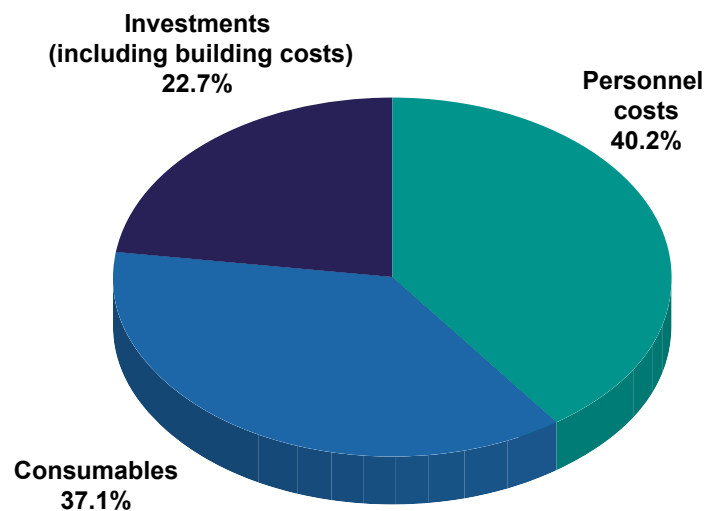
Revenue 2020

Federal Funding	16.700.000 €
Bavarian Funding	34.854.400 €
Contribution TUM (Planstellen)	10.363.467 €
Contribution FZJ	9.850.000 €
Contribution Hereon	1.320.000 €
Total	73.087.867 €



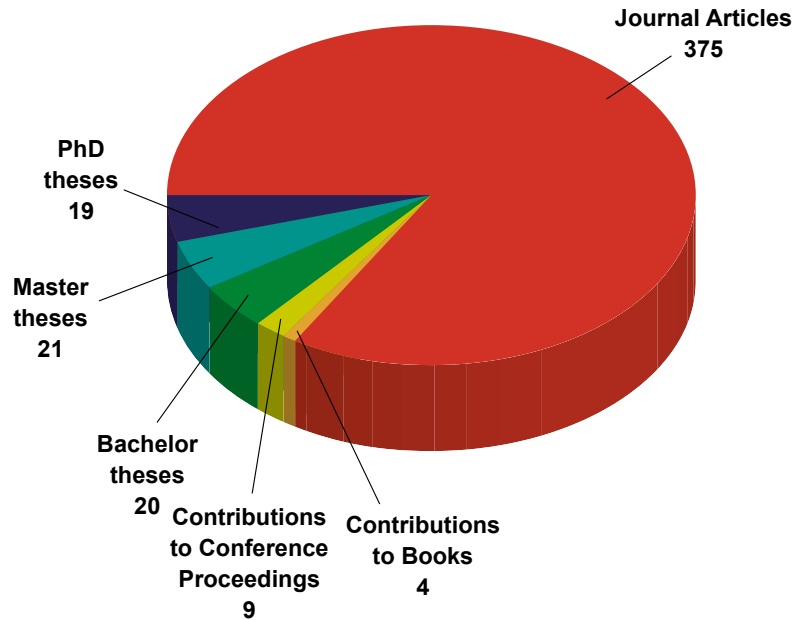
Expenses 2020

	TUM (€)	FZJ (€)	Hereon (€)	Total (€)
Personnel costs	18.107.502 €	8.050.000 €	1.917.000 €	28.074.502 €
Consumables	22.743.550 €	2.684.000 €	432.000 €	25.859.550 €
Investment (including building costs)	8.934.514 €	6.850.000 €	47.000 €	15.831.514 €
Total	49.785.566 €	17.584.000 €	2.396.000 €	69.765.566 €



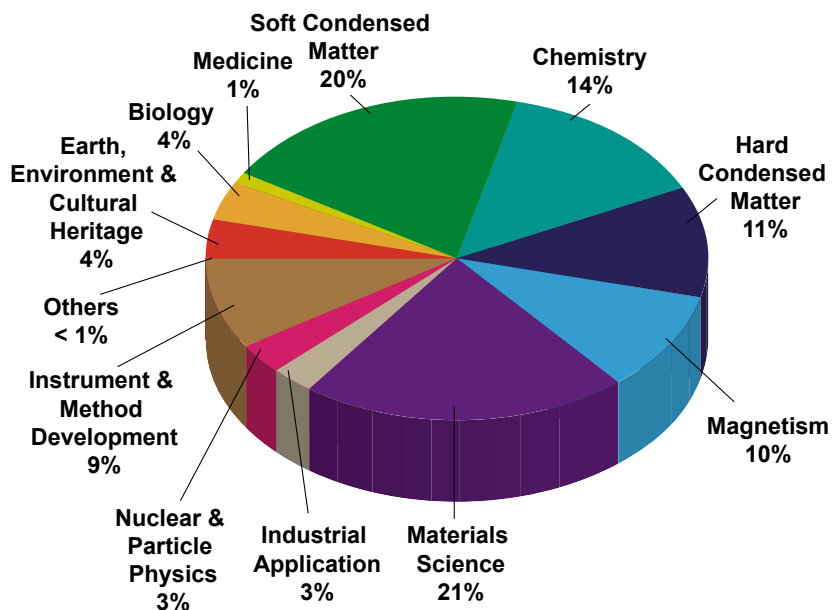
Publications & Theses

In 2020, we received notice of a total of 388 scientific publications, including journal articles, contributions to books and conference proceedings (<https://impulse.mlz-garching.de/> and Fig. below). Furthermore, in total 60 theses supervised by staff of the MLZ and its partner institutions were completed in 2020.

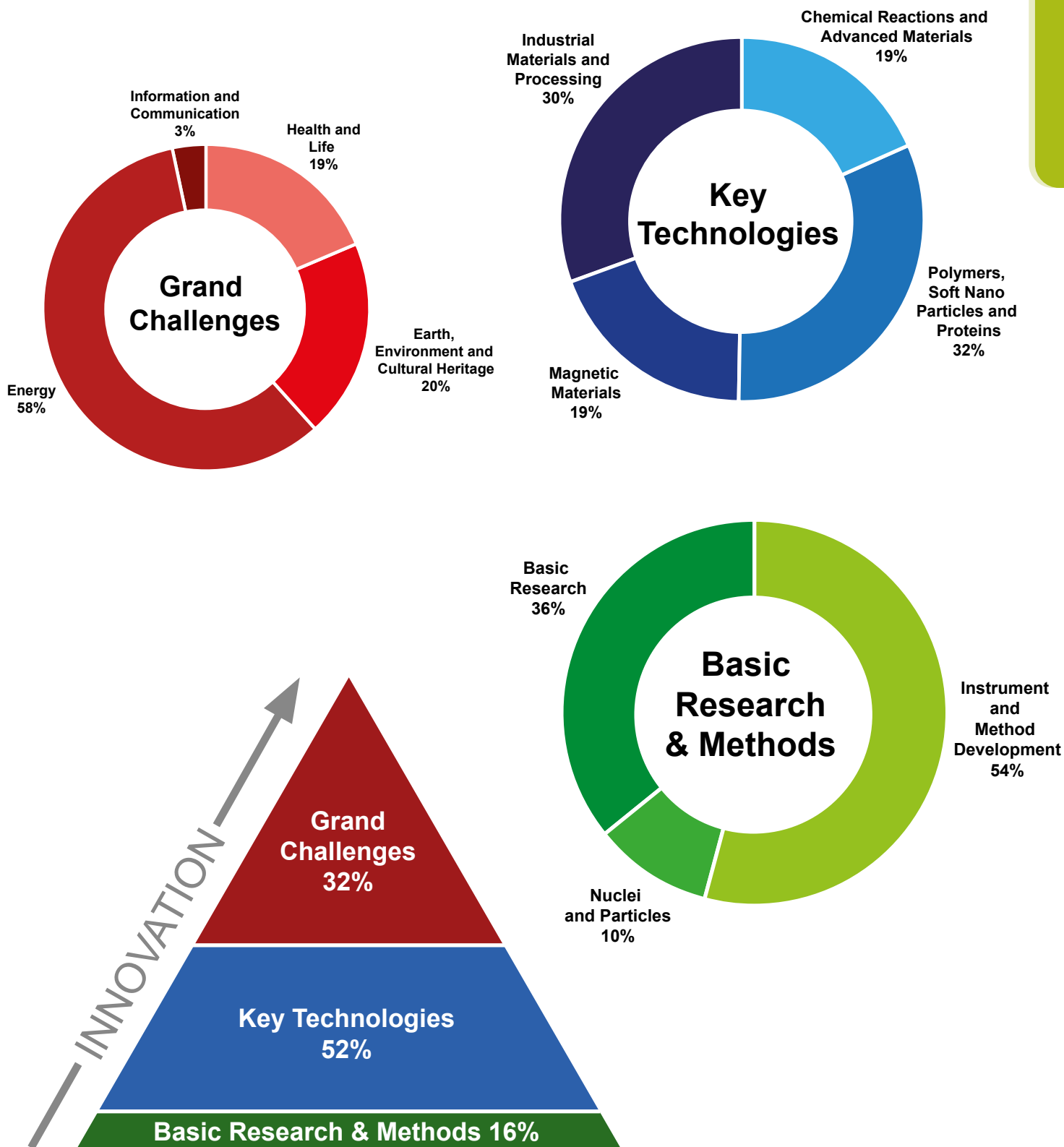


In 2020, about 210 PhD theses, based on experiments at the MLZ or method and instrument developments for the MLZ, were either ongoing or completed. Of these, about 145 are under the direct supervision of staff at the MLZ and its collaboration partners while the others involve external users. In total, 44 of the 210 PhD theses have been completed in 2020, including external users. Of all the doctoral students, around 89% come from German universities, 10% from other universities in Europe and 1% from the rest of the world.

The next Fig. shows the classification of the journal articles by Scientific Area (several tags per journal article are possible):



The journal articles at the MLZ can be pictured as a pyramid: Basic Research & Methods (16%) required to tackle the Key Technologies (52%) and articles that address directly the Grand Challenges of our society today (32%). The circular charts represent the individual subjects being dealt with within these three categories.



Committees

Steering Committee

Chair

Dr. Jürgen Kroseberg
Federal Ministry for Education and Research

Prof. Dr. Stephan Paul
Technical University of Munich

Members

Dr. Ulrike Kirste (Vice Chair)
Bavarian State Ministry of Science and the Arts

Prof. Dr. Matthias Rehahn
Helmholtz-Zentrum hereon GmbH

Albert Berger
Technical University of Munich

Guests
Prof. Dr. Peter Müller-Buschbaum
FRM II, Technical University of Munich

Prof. Dr.-Ing. Harald Bolt
Forschungszentrum Jülich GmbH

Prof. Dr. Stephan Förster
Forschungszentrum Jülich GmbH

Prof. Dr. Thomas Hofmann, represented by
Prof. Dr. sc. tech. Gerhard Kramer
Technical University of Munich

Dr. Axel Pichlmaier
FRM II, Technical University of Munich

Prof. Dr. Jan Lüning
Helmholtz-Zentrum Berlin GmbH

Robert Rieck
FRM II, Technical University of Munich

Dirk Schlotmann
Forschungszentrum Jülich GmbH



Fig. 1: Virtual Steering Committee meeting in December 2020 with A. Pichlmaier, R. Rieck, J. Kroseberg, D. Schlotmann, P. Müller-Buschbaum, S. Förster, M. Rehahn, G. Kramer, U. Kirste, S. Paul, A. Berger, and J. Lüning (from left to right and top to bottom).



Fig. 2: Virtual meeting of the Scientific Advisory Board in October 2020 with C. Alba-Simionesco, W. Daum, P. Müller-Buschbaum, S. Förster, M. Müller, T. Hellweg, B. Keimer, R. Niewa, H. Abele, R. v. Klitzing, M. Kenzelmann, and A. Arbe (from left to right and top to bottom).

Scientific Advisory Board

Chair

Prof. Dr. Christiane Alba-Simionesco
Laboratoire Léon Brillouin, Saclay

Prof. Dr. Bernhard Keimer
Max Planck Institute for
Solid State Research, Stuttgart

Members

Prof. Dr. Hartmut Abele
TU Wien

Prof. Dr. Michel Kenzelmann
Paul Scherrer Institute, Villigen

Prof. Dr. Arantxa Arbe
Material Physics Center, San Sebastián

Prof. Dr. Rainer Niewa
University of Stuttgart

Alejandro Javier Guirao Blank
Volkswagen AG, Wolfsburg

Prof. Dr. Joachim Rädler
Ludwig Maximilian University of Munich

Werner Daum
Bundesanstalt für Materialforschung
und -prüfung (BAM), Berlin

Prof. Dr. Helmut Schober
Institut Laue-Langevin, Grenoble

Prof. Dr. Thomas Hellweg
Bielefeld University

Prof. Dr. Regine v. Klitzing
Technical University of Darmstadt



Fig. 3: Meeting of the Instrumentation Advisory Committee in March 2020 with S. Busch, S. Mattauch, E. Lehmann, W. Lohstroh, S. Förster, B. Keimer, M. Russina, P. Müller-Buschbaum, C. Pappas, F. Ott, U. Köster, and J. Neuhaus (from left to right). The members M. T. Fernández-Díaz and H. Rønnow joined from remote.

Instrumentation Advisory Committee

Chair

Prof. Dr. Bernhard Keimer
Max Planck Institute for Solid State Research, Stuttgart

Dr. Frédéric Ott
Laboratoire Léon Brillouin, Saclay

Members

Dr. Maria Teresa Fernández-Díaz
Institut Laue-Langevin, Grenoble

Prof. Dr. Catherine Pappas
Delft University of Technology

Dr. Ulli Köster
Institut Laue-Langevin, Grenoble

Prof. Dr. Henrik Rønnow
Ecole Polytechnique Fédérale de Lausanne

Dr. Eberhard Lehmann
Paul Scherrer Institute, Villigen

Dr. Margarita Russina
Helmholtz-Zentrum Berlin für
Materialien und Energie

Evaluation of Beam Time Proposals: Members of the Review Panels

Prof. Dr. Lise Arleth
Niels Bohr Institute
University of Copenhagen

Dr. Mikhail Avdeev
Frank Laboratory of Neutron Physics
Joint Institute for Nuclear Research, Dubna

Prof. Dr. Piero Baglioni
University of Florence

Prof. Dr. Peter Battle
University of Oxford

Dr. Matthew Blakeley
Institut Laue-Langevin, Grenoble

Dr. Johann Bouchet
Commissariat à l'énergie atomique et
aux énergies alternatives, Arpajon

Dr. Philippe Bourges
Laboratoire Léon Brillouin, Saclay

Prof. Dr. William Brant
Uppsala University

Prof. Dr. Richard Campell
University of Manchester

Dr. Daniel Clemens
Helmholtz-Zentrum Berlin für
Materialien und Energie

Dr. Robert Cubitt
Institut Laue-Langevin, Grenoble

Dr. Sabrina Disch
University of Cologne

Dr. Stephan Eijt
Delft University of Technology

Prof. Dr. Ulli Englert
RWTH Aachen University

Prof. Dr. Björn Fåk
Institut Laue-Langevin, Grenoble

Dr. Bela Farago
Institut Laue-Langevin, Grenoble

Prof. Dr. Rupert Gebhard
Archäologische Staatssammlung, München

Dr. Anne-Caroline Genix
Laboratoire Charles Coulomb
Université Montpellier

Dr. Francesco Grazzi
National Research Council of Italy,
Florence Research Area

Dr. Christian Grünzweig
Paul Scherrer Institute, Villigen

Dr. Klaus Habicht
Helmholtz-Zentrum Berlin für
Materialien und Energie

Prof. Dr. Thomas Hellweg
Bielefeld University

Prof. Dr. Paul Henry
ISIS Neutron and Muon Source, Didcot

Prof. Dr. Björgvin Hjörvarsson
Uppsala University

Dr. Ingo Hoffmann
Institut Laue-Langevin, Grenoble

Dr. Klaudia Hradil
TU Wien

Dr. Christy Kinane
ISIS Neutron and Muon Source, Didcot

Dr. Joachim Kohlbrecher
Paul Scherrer Institute, Villigen

Dr. Reinhard Kremer
Max Planck Institute for
Solid State Research, Stuttgart

Prof. Dr. Christian Krempaszky
Technical University of Munich, Garching

Prof. Dr. Jeremy Lakey
University of Newcastle

Dr. Reidar Lund
Oslo University



Fig. 4: MLZ Director Peter Müller-Buschbaum during the plenary session of the online review panels' meeting in May 2020.

Dr. Sandrine Lyonnard
Commissariat à l'énergie atomique et
aux énergies alternatives, Grenoble

Prof. Dr. Andreas Magerl
Universität Erlangen-Nürnberg

Dr. Nicolas Martin
Laboratoire Léon Brillouin, Saclay

Dr. Eric Mauerhofer
Forschungszentrum Jülich GmbH

Prof. Dr. Andreas Michels
University of Luxembourg

Dr. Gwilherm Nénert
PANalytical B.V., Almelo

Dr.-Ing. Thomas Nitschke-Pagel
TU Braunschweig

Prof. Dr. Tommy Nylander
Lund University

Dr. Esko Oksanen
European Spallation Source, Lund

Prof. Dr. Andrea Orecchini
Università degli Studi di Perugia

Dr. Alessandro Paciaroni
Università degli Studi di Perugia

Prof. Dr. Christine Papadakis
Technical University of Munich, Garching

Dr. Oleg Petrenko
University of Warwick

Dr. Thilo Pirling
Institut Laue-Langevin, Grenoble

Prof. Dr. Radosław Przeniosło
University of Warsaw

Prof. Dr. Diana Lucia Quintero Castro
University of Stavanger

Dr. Navid Qureshi
Institut Laue-Langevin, Grenoble

Dr. Florin Radu
Helmholtz-Zentrum Berlin für
Materialien und Energie

Prof. Dr. Günther Redhammer
University of Salzburg

Dr. Sarah Rogers
ISIS Neutron and Muon Source, Didcot

Dr. Emmanuel Schneck
Max Planck Institute of
Colloids and Interfaces, Potsdam

Dr. Romain Sibille
Paul Scherrer Institute, Villigen

Dr. Thorsten Soldner
Institut Laue-Langevin, Grenoble

Prof. Dr. Thomas Sottmann
University of Stuttgart

Prof. Dr. Wolfgang Sprengel
Graz University of Technology

Dr. Andreas Stark
Helmholtz-Zentrum hereon GmbH

Dr. Ross Stewart
ISIS Neutron and Muon Source, Didcot

Dr. Christopher Stock
University of Edinburgh

Dr. Pavel Strunz
Nuclear Physics Institute, Řez near Prague

Dr. Anne Stunault
Institut Laue-Langevin, Grenoble

Dr. László Szentmiklósi
Hungarian Academy of Sciences, Budapest

Dr. Kristiaan Temst
KU Leuven

Prof. Dr. Regine von Klitzing
Technical University of Darmstadt

Dr. Frank Weber
Karlsruhe Institute of Technology

Jun. Prof. Dr. Hongbin Zhang
Technical University of Darmstadt

MLZ User Committee

Chair

Prof. Dr. Adrian Rennie
Uppsala University

Members

Dr. Sophie Combet
Laboratoire Léon Brillouin, Saclay

Dr.-Ing. Jens Gibmeier
Karlsruhe Institute of Technology

Prof. Dr. David Keeble
University of Dundee

Prof. Dr. Luigi Paduano
University of Naples

Prof. Dr. Diana Quintero Castro
University of Stavanger

Prof. Dr. Rainer Niewa (Observer on behalf of the KFN)
University of Stuttgart

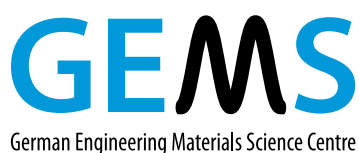
Partner institutions



Bavarian Research Institute of
Experimental Geochemistry and Geophysics
University of Bayreuth
www.bgi.uni-bayreuth.de



Georg-August-Universität Göttingen
• Geowissenschaftliches Zentrum
www.uni-goettingen.de/de/125309.html



German Engineering Materials Science Centre GEMS
Helmholtz-Zentrum hereon GmbH
www.hereon.de/central_units/gems



Jülich Centre for Neutron Science JCNS
Forschungszentrum Jülich GmbH
www.jcns.info



Karlsruhe Institute of Technology

- Institute for Applied Materials – Energy Storage Systems (IAM-ESS)
www.iam.kit.edu



Ludwig Maximilian University of Munich

- Section Crystallography
www.lmu.de/kristallographie
- Faculty of Physics
www.softmatter.physik.uni-muenchen.de



MAX-PLANCK-GESELLSCHAFT

Max Planck Institute for Solid State Research
Stuttgart

www.fkf.mpg.de



RWTH Aachen University

- Institute of Crystallography
www.xtal.rwth-aachen.de
- Institute of Inorganic Chemistry
www.iac.rwth-aachen.de



Clausthal University of Technology

- Institute of Materials Science and Engineering
www.iww.tu-clausthal.de



Technische Universität Dresden

- Institute of Solid State and Materials Physics
www.tu-dresden.de/mn/physik/ifp



Technical University of Munich

Department of Physics

- E13 - Institute for Functional Materials
www.functmat.ph.tum.de
- E18 - Institute for Hadronic Structure and Fundamental Symmetries
www.e18.ph.tum.de
- E21 - Research area Strongly Correlated Electron Systems
www.sces.ph.tum.de
- RCM - Radiochemie München
www.rcm.tum.de



Klinikum rechts der Isar

Technical University of Munich

- MRI - Klinikum Rechts der Isar
www.mri.tum.de



Technical University of Munich

- Exzellenzcluster „Origin and Structure of the Universe“
www.universe-cluster.de



TECHNISCHE
UNIVERSITÄT
WIEN
Vienna University of Technology

Vienna University of Technology

- Neutron- and Quantum Physics
Research area at the Atominstut Vienna
Abele Group
<https://ati.tuwien.ac.at/forschungsgruppen/nqp/home/>



Universität der Bundeswehr München

- Institute of Applied Physics and Measurement
Technology
www.unibw.de/lrt2

Universität zu Köln



University of Cologne

Faculty of Mathematics and
Natural Sciences

- Institute for Nuclear Physics
www.ikp.uni-koeln.de
- Institute of Physics II
www.ph2.uni-koeln.de

Imprint

Publisher

Technische Universität München
Forschungs-Neutronenquelle
Heinz Maier-Leibnitz (FRM II)
Lichtenbergstr. 1
85747 Garching
Germany

Phone: +49.89.289.14965
Fax: +49.89.289.14995
Internet: www.mlz-garching.de
www.frm2.tum.de
E-Mail: jahresbericht@frm2.tum.de

Editorial Office, Design and typesetting

Ramona Bucher
Katharina Dietmann
Diana Fleischer
Anke Görg
Connie Hesse
Andrea Voit

Editors

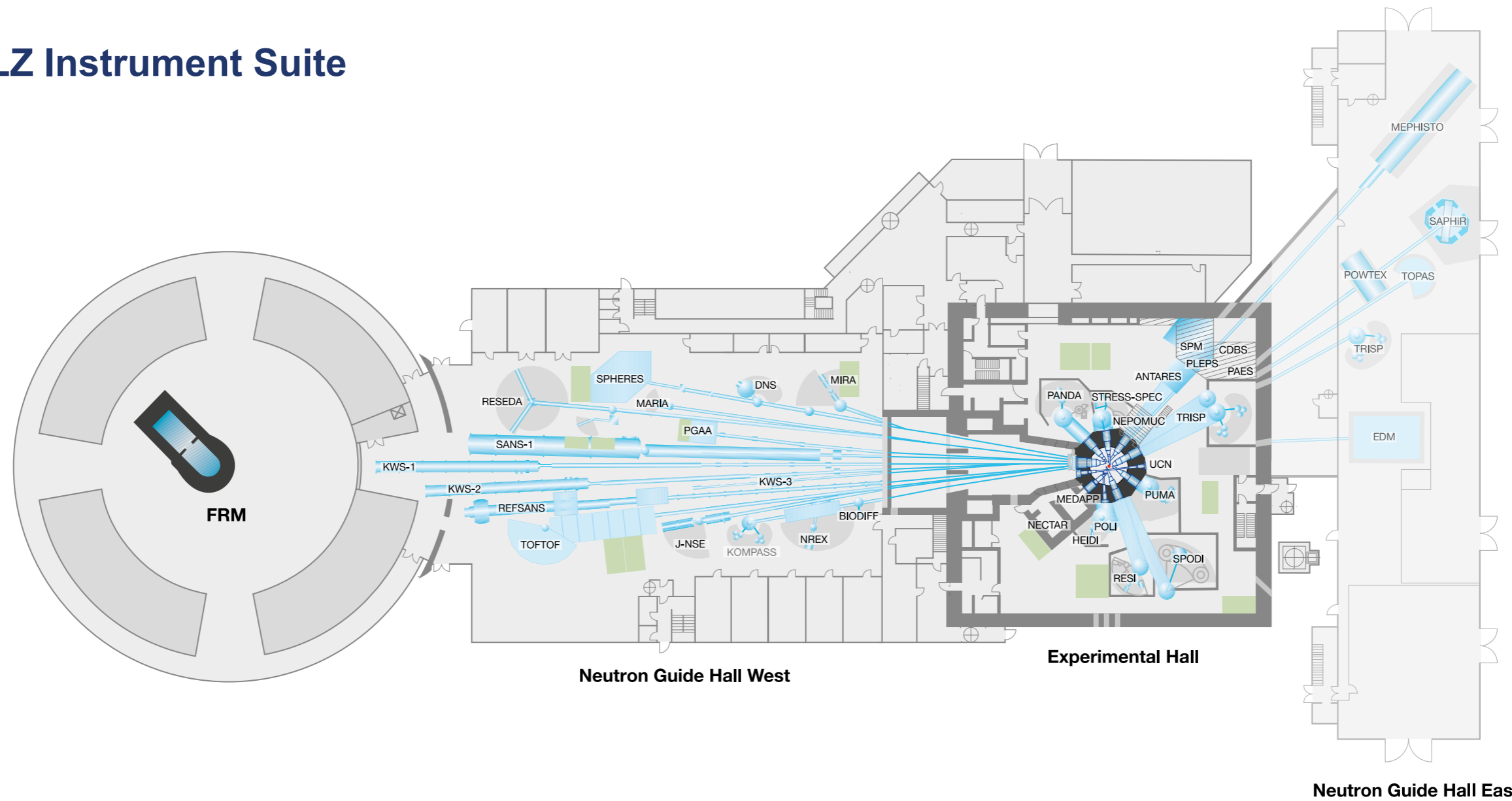
Sebastian Busch
Henrich Frielinghaus
Robert Georgii
Markus Hölzel
Michael Hofmann
Olaf Holderer
Johanna Jochum
Peter Link
Martin Meven
Andreas Ostermann
Björn Pedersen
Zsolt Revay
Anatoliy Senyshyn
Christian Stieghorst
Yixi Su
Marcell Wolf

Photographic credits

Front page	Dr. Eve V. Stenson (IPP) and Markus Singer (TUM)
p. 4	top: Astrid Eckert (TUM) bottom left: Andreas Heddergott (TUM) bottom 2 nd left: Ralf-Uwe Limbach bottom 2 nd right: Alessandra Schellnegger bottom right: Astrid Eckert (TUM)
p. 9	MCQST by Jan Greune
p. 10	Dr. Weimin Gan (Hereon)
p. 12	Andreas Heddergott (TUM)
p. 13	Pradeep Shanbogh (University of Cologne)
p. 14	Andreas Heddergott (TUM)
p. 15	Andreas Heddergott (TUM)
p. 16	Wolfgang Filser (TUM)
p. 17	Wenzel Schürmann (TUM)
p. 18	Wenzel Schürmann (TUM)
p. 19	Dr. Eve V. Stenson (IPP) and Markus Singer (TUM)
p. 30	André Moreira (visao) (1), Dr. Nuno Canha (2), Wenzel Schürmann (TUM) (3)
p. 75	Wenzel Schürmann (TUM)
p. 79	Wenzel Schürmann (TUM)
p. 81	top: Misha Lasakov middle: CERIC-ERIC bottom: Wenzel Schürmann (TUM)
p. 82	middle: Wenzel Schürmann (TUM) bottom: Roland Albrecht
p. 83	middle: Wenzel Schürmann (TUM)
p. 84	top: Andreas Heddergott (TUM) middle: Wenzel Schürmann (TUM) bottom: Wenzel Schürmann (TUM)
p. 85	top 3 rd : Wenzel Schürmann (TUM)
p. 98	Wenzel Schürmann (TUM)
Back page	Wenzel Schürmann (TUM)

Editors, authors or FRM II/ TUM:
other images

MLZ Instrument Suite



Instrument	Description	Neutrons	Operated by	Funding	Instrument group at MLZ
ANTARES	Radiography and tomography	cold	TUM	TUM	FRM II
BIODIFF	Diffractionmeter for large unit cells	cold	TUM, JCNS	TUM, FZJ	FRM II, JCNS
DNS	Diffuse scattering spectrometer	cold	JCNS	FZJ	JCNS
HEIDI	Single crystal diffractometer	hot	RWTH Aachen	FZJ	JCNS
J-NSE	Spin-echo spectrometer	cold	JCNS	FZJ	JCNS
KOMPASS*	Three axes spectrometer	cold	Uni Köln, TUM	VF	FRM II
KWS-1	Small angle scattering	cold	JCNS	FZJ	JCNS
KWS-2	Small angle scattering	cold	JCNS	FZJ	JCNS
KWS-3	Very small angle scattering	cold	JCNS	FZJ	JCNS
MARIA	Magnetic reflectometer	cold	JCNS	FZJ	JCNS
MEPHISTO**	Instrument for particle physics, PERC	cold	TUM	TUM, DFG	FRM II
MIRA	Multipurpose instrument	cold	TUM	TUM	FRM II
MEDAPP	Medical irradiation treatment	fast	TUM	TUM	FRM II
NECTAR	Radiography and tomography	fast	TUM	TUM	FRM II
NEPOMUC	Positron source, CDBS, PAES, PLEPS, SPM	-	TUM, UniBw München	TUM	FRM II
NREX	Reflectometer with X-ray option	cold	MPI Stuttgart	MPG	MPI Stuttgart
PANDA	Three axes spectrometer	cold	JCNS	FZJ	JCNS

Instrument	Description	Neutrons	Operated by	Funding	Instrument group at MLZ
PGAA	Prompt gamma activation analysis	cold	Uni Köln	TUM	FRM II
PUMA	Three axes spectrometer	thermal	TUM	TUM	FRM II
POLI	Single-crystal diffractometer polarized neutrons	hot	RWTH Aachen	FZJ	JCNS
POWTEX*	Time-of-flight diffractometer	thermal	RWTH Aachen, Uni Göttingen, JCNS	VF, FZJ	JCNS
REFSANS	Reflectometer	cold	GEMS	Hereon	GEMS
RESEDA	Resonance spin-echo spectrometer	cold	TUM	TUM	FRM II
RESI/ERWIN*	Neutron diffractometer	thermal	LMU, KIT	VF, TUM	FRM II
SANS-1	Small angle scattering	cold	TUM, GEMS	TUM, Hereon	FRM II, GEMS
SAPHIR*	Six anvil press for radiography and diffraction	thermal	Uni Bayreuth	VF, TUM	FRM II
SPHERES	Backscattering spectrometer	cold	JCNS	FZJ	JCNS
SPODI	Powder diffractometer	thermal	KIT	TUM	FRM II
STRESS-SPEC	Materials science diffractometer	thermal	TUM, TU Clausthal, GEMS	TUM, Hereon	FRM II, GEMS
TOFTOF	Time-of-flight spectrometer	cold	TUM	TUM	FRM II
TOPAS*	Time-of-flight spectrometer	thermal	JCNS	FZJ	JCNS
TRISP	Three axes spin-echo spectrometer	thermal	MPI Stuttgart	MPG	MPI Stuttgart
UCN*	Ultra cold neutron source, EDM	ultra-cold	TUM	TUM, DFG	FRM II

*construction
 **reconstruction
 VF: instrument construction funded by "BMBF-Verbundforschung" (Collaborative Projects)



Heinz Maier-Leibnitz Zentrum (MLZ)

www.mlz-garching.de

DOI: 10.14459/2021md1601341